The Astrophysical Journal, 966:157 (57pp), 2024 May 10 https://doi.org/10.3847/1538-4357/ad31a5

The Atacama Cosmology Telescope: Cosmology from Cross-correlations of unWISE Galaxies and ACT DR6 CMB Lensing

Gerrit S. Farren[1,2], Alex Krolewski[3,4], Niall MacCrann[1], Simone Ferraro[5,6], Irene Abril-Cabezas[1], Rui An[7], Zachary Atkins[8], Nicholas Battaglia[9], J. Richard Bond[10], Erminia Calabrese[11], Steve K. Choi[9,12], Omar Darwish[13], Mark J. Devlin[14], Adriaan J. Duivenvoorden[8,15], Jo Dunkley[8,16], J. Colin Hill[17], Matt Hilton[18,19], Kevin M. Huffenberger[20], Joshua Kim[21], Thibaut Louis[22], Mathew S. Madhavacheril[14], Gabriela A. Marques[23,24], Jeff McMahon[24,25,26,27], Kavilan Moodley[28], Lyman A. Page[8], Bruce Partridge[29], Frank J. Qu[1], Emmanuel Schaan[30,31], Neelima Sehgal[32], Blake D. Sherwin[1,2], Cristóbal Sifón[33], Suzanne T. Staggs[8], Alexander Van Engelen[34], Cristian Vargas[35], Lukas Wenzl[9], Martin White[36], and Edward J. Wollack[37]
[1] DAMTP, Centre for Mathematical Sciences, University of Cambridge, Wilberforce Road, Cambridge CB3 OWA, UK; gsf29@cam.ac.uk
[2] Kavli Institute for Cosmology Cambridge, Madingley Road, Cambridge CB3 0HA, UK
[3] Perimeter Institute for Theoretical Physics, 31 Caroline St. North, Waterloo, ON NL2 2Y5, Canada
[4] Waterloo Centre for Astrophysics, University of Waterloo, Waterloo, ON N2L 3G1, Canada
[5] Physics Division, Lawrence Berkeley National Laboratory, Berkeley, CA, USA
[6] Berkeley Center for Cosmological Physics, University of California, Berkeley, CA 94720, USA
[7] Department of Physics and Astronomy, University of Southern California, Los Angeles, CA 90089, USA
[8] Joseph Henry Laboratories of Physics, Jadwin Hall, Princeton University, Princeton, NJ 08544, USA
[9] Department of Astronomy, Cornell University, Ithaca, NY 14853, USA
[10] Canadian Institute for Theoretical Astrophysics, University of Toronto, Toronto, ON, M5S 3H8, Canada
[11] School of Physics and Astronomy, Cardiff University, The Parade, Cardiff, Wales CF24 3AA, UK
[12] Department of Physics, Cornell University, Ithaca, NY 14853, USA
[13] Université de Genève, Département de Physique Théorique et CAP, 24 quai Ernest-Ansermet, CH-1211 Genève 4, Switzerland
[14] Department of Physics and Astronomy, University of Pennsylvania, 209 South 33rd Street, Philadelphia, PA 19104, USA
[15] Center for Computational Astrophysics, Flatiron Institute, New York, NY 10010, USA
[16] Department of Astrophysical Sciences, Peyton Hall, Princeton University, Princeton, NJ 08544, USA
[17] Department of Physics, Columbia University, 538 West 120th Street, New York, NY 10027, USA
[18] Wits Centre for Astrophysics, School of Physics, University of the Witwatersrand, Private Bag 3, 2050, Johannesburg, South Africa
[19] Astrophysics Research Centre, School of Mathematics, Statistics, and Computer Science, University of KwaZulu-Natal, Westville Campus, Durban 4041, South Africa
[20] Department of Physics, Florida State University, Tallahassee, FL 32306, USA
[21] Department of Physics and Astronomy, University of Pennsylvania, Philadelphia, PA 19104, USA
[22] Université Paris-Saclay, CNRS/IN2P3, IJCLab, 91405 Orsay, France
[23] Fermi National Accelerator Laboratory, P.O. Box 500, Batavia, IL 60510, USA
[24] Kavli Institute for Cosmological Physics, University of Chicago, 5640 S. Ellis Avenue, Chicago, IL 60637, USA
[25] Department of Astronomy and Astrophysics, University of Chicago, 5640 S. Ellis Avenue, Chicago, IL 60637, USA
[26] Department of Physics, University of Chicago, Chicago, IL 60637, USA
[27] Enrico Fermi Institute, University of Chicago, Chicago, IL 60637, USA
[28] Astrophysics Research Centre, School of Mathematics, Statistics and Computer Science, University of KwaZulu-Natal, Durban 4001, South Africa
[29] Department of Physics and Astronomy, Haverford College, Haverford, PA 19041, USA
[30] SLAC National Accelerator Laboratory, Menlo Park, CA 94025, USA
[31] Kavli Institute for Particle Astrophysics and Cosmology and Department of Physics, Stanford University, Stanford, CA 94305, USA
[32] Physics and Astronomy Department, Stony Brook University, Stony Brook, NY 11794, USA
[33] Instituto de Física, Pontificia Universidad Católica de Valparaíso, Casilla 4059, Valparaíso, Chile
[34] School of Earth and Space Exploration, Arizona State University, Tempe, AZ 85287, USA
[35] Instituto de Astrofísica and Centro de Astro-Ingenieía, Facultad de Física, Pontificia Universidad Católica de Chile, Av. Vicuña Mackenna 4860, 7820436 Macul, Santiago, Chile
[36] Department of Physics, University of California, Berkeley, 366 LeConte Hall MC 7300, Berkeley, CA 94720-7300, USA
[37] NASA/Goddard Space Flight Center, Greenbelt, MD 20771, USA
Received 2023 September 15; revised 2024 March 5; accepted 2024 March 6; published 2024 May 2

Abstract

We present tomographic measurements of structure growth using cross-correlations of Atacama Cosmology Telescope (ACT) DR6 and Planck cosmic microwave background (CMB) lensing maps with the unWISE Blue and Green galaxy samples, which span the redshift ranges $0.2 \lesssim z \lesssim 1.1$ and $0.3 \lesssim z \lesssim 1.8$, respectively. We improve on prior unWISE cross-correlations not just by making use of the new, high-precision ACT DR6 lensing maps, but also by including additional spectroscopic data for redshift calibration and by analyzing our measurements with a more flexible theoretical model. We determine the amplitude of matter fluctuations at low redshifts ($z \simeq 0.2$–1.6), finding $S_8 \equiv \sigma_8(\Omega_m/0.3)^{0.5} = 0.813 \pm 0.021$ using the ACT cross-correlation alone and $S_8 = 0.810 \pm 0.015$ with a combination of Planck and ACT cross-correlations; these measurements are fully consistent with the predictions from primary CMB measurements assuming standard structure growth. The addition of baryon acoustic oscillation

data breaks the degeneracy between σ_8 and Ω_m, allowing us to measure $\sigma_8 = 0.813 \pm 0.020$ from the cross-correlation of unWISE with ACT and $\sigma_8 = 0.813 \pm 0.015$ from the combination of cross-correlations with ACT and Planck. These results also agree with the expectations from primary CMB extrapolations in ΛCDM cosmology; the consistency of σ_8 derived from our two redshift samples at $z \sim 0.6$ and 1.1 provides a further check of our cosmological model. Our results suggest that structure formation on linear scales is well described by ΛCDM even down to low redshifts $z \lesssim 1$.

Unified Astronomy Thesaurus concepts: Observational cosmology (1146); Sigma8 (1455); Cosmological parameters from large-scale structure (340); Cosmic microwave background radiation (322); Weak gravitational lensing (1797); Large-scale structure of the universe (902); Cosmology (343); Cosmological parameters (339)

1. Introduction

Measuring the amplitude of low-redshift matter fluctuations can probe the growth of cosmic structure over time, reveal the properties of dark matter and dark energy, constrain the masses of neutrinos, and provide important tests of general relativity. A number of lensing-related techniques have been developed for this purpose, including both galaxy lensing and cosmic microwave background (CMB) lensing.

Recent measurements of galaxy weak lensing from the Dark Energy Survey (DES; Flaugher et al. 2015; Abbott et al. 2022), the Kilo-Degree Survey (KiDS; Kuijken et al. 2015; Heymans et al. 2021), Hyper Suprime-Cam (HSC; Aihara et al. 2017; Miyatake et al. 2023; More et al. 2023; Sugiyama et al. 2023), among others, have found a 2σ–3σ lower amplitude of fluctuations, compared to the prediction from Planck primary CMB assuming standard structure growth. In particular, parameterizing the low-redshift amplitude by $S_8 \equiv \sigma_8(\Omega_m/0.3)^{0.5}$ (which is the quantity best measured by galaxy weak lensing surveys), DES, KiDS, and HSC obtain $S_8 = 0.782 \pm 0.019$,[38] $S_8 = 0.765^{+0.017}_{-0.016}$,[39] $S_8 = 0.775^{+0.043}_{-0.038}$,[40] respectively, from a combination of cosmic shear and galaxy clustering (Heymans et al. 2021; Abbott et al. 2022; Sugiyama et al. 2023). HSC also presents an alternative analysis using smaller scales and a halo-mode-based approach using a cosmological emulator (rather than the linear bias approximation used on large scales) finding $S_8 = 0.763^{+0.040}_{-0.036}$[41] (Miyatake et al. 2023). A recent joint reanalysis of the DES and KiDS cosmic shear data hints at a slightly higher value of $S_8 = 0.790^{+0.018}_{-0.014}$ (Abbott et al. 2023a). Comparing to the value $S_8 = 0.834 \pm 0.016$ from the Planck primary CMB (or $S_8 = 0.832 \pm 0.013$ when including CMB lensing; Planck Collaboration et al. 2020a), we see that most recent galaxy weak lensing surveys have a preference for slightly lower S_8, even though no single experiment is in significant tension with Planck. The recent DES + KiDS reanalysis of cosmic shear is consistent at the 1.7σ level.

CMB lensing probes the same physics as galaxy weak lensing, but has different potential systematics; a known redshift of the *source* (the primary CMB) and well-understood statistical properties make it a particularly reliable and independent cosmological probe. The CMB lensing autocorrelation is in excellent agreement with the primary CMB predictions: recent measurements from the Atacama Cosmology Telescope (ACT; Madhavacheril et al. 2024; Qu et al. 2024) combined with baryon acoustic oscillation (BAO) data yield $S_8 = 0.840 \pm 0.028$ from ACT alone and $S_8 = 0.831 \pm 0.023$ when combined with Planck lensing (Planck Collaboration et al. 2020b; Carron et al. 2022).

However, the cross-correlation between CMB lensing and galaxies has at times shown a preference for a lower S_8. For example, cross-correlations of DESI Luminous Red Galaxy (LRG) targets (Kitanidis & White 2020; Hang et al. 2021; White et al. 2022) or galaxies from the Baryon Oscillation Spectroscopic Survey (BOSS; Singh et al. 2020; Chen et al. 2022b) with Planck lensing show a preference for a lower S_8 at up to 3σ. An analysis of the cross-correlation between CMB lensing from the South Pole Telescope (SPT) and Planck and various data sets from DES finds varying levels of tension between 2.2σ and 3σ (see Section 10.2 for details; Abbott et al. 2023b; Chang et al. 2023). Cross-correlations with previous CMB lensing reconstructions from ACT have also found this preference at the $\sim 2\sigma$ level, albeit with substantial uncertainties. Using CMB lensing data from ACT DR4 and Planck together with galaxy shear from KiDS-1000, Robertson et al. (2021) found $S_8 = 0.64 \pm 0.08$; similarly, an analysis of the cross-correlation between ACT DR4 CMB lensing and galaxy clustering from DES-Y3 yields $S_8 = 0.75^{+0.04}_{-0.05}$ (Marques et al. 2024).

Moreover, Krolewski et al. (2021) used the unWISE full-sky galaxy catalog split into three tomographic bins spanning the redshift range of $0 \lesssim z \lesssim 2$ (with the power spectra and redshift distributions measured in Krolewski et al. 2020), together with the Planck 2018 CMB lensing maps (Planck Collaboration et al. 2020b), to set a constraint $S_8 = 0.784 \pm 0.015$, about 2.4σ lower than estimated from the primary CMB. Motivated by the availability of additional data for the unWISE redshift distribution calibration, improved understanding of the calibration of Planck CMB lensing maps, and the availability of lower-noise CMB lensing maps from Planck PR4 and ACT DR6, we perform a new and improved analysis of the cross-correlation between unWISE galaxies and CMB lensing. An expanded set of null tests, enhanced foreground control, and improved theoretical modeling add to the robustness of the measurement.

This paper is structured as follows: in Section 2, we briefly summarize the key results of this work before introducing the data sets used in this work in Section 3. In Section 4, we present the measurements of the galaxy autocorrelation power spectra and the galaxy-CMB lensing cross-power spectra. In Sections 5 and 6, we introduce the simulations we use in this work and describe how we estimate the data covariance.

[38] This value is obtained from the public DES parameter chain with fixed neutrino mass here (http://desdr-server.ncsa.illinois.edu/despublic/y3a2_files/chains/chain_3x2pt_fixednu_lcdm.txt). We adopt this result throughout for better comparability with our analysis, which fixes the neutrino mass to the minimum value allowed in the normal hierarchy.

[39] This differs from the results reported by KiDS, $S_8 = 0.766^{+0.020}_{-0.014}$. KiDS by default reports the MAP value along with the projected joint highest posterior density region (PJ-HPD). For better comparability, however, we adopt throughout the marginalized mean and credible interval instead.

[40] We note that the HSC results we compare to in Section 10.2 differ slightly from these values as they are derived from a reanalysis of the HSC data with prior choices consistent with those adopted in this work.

[41] See footnote 40.

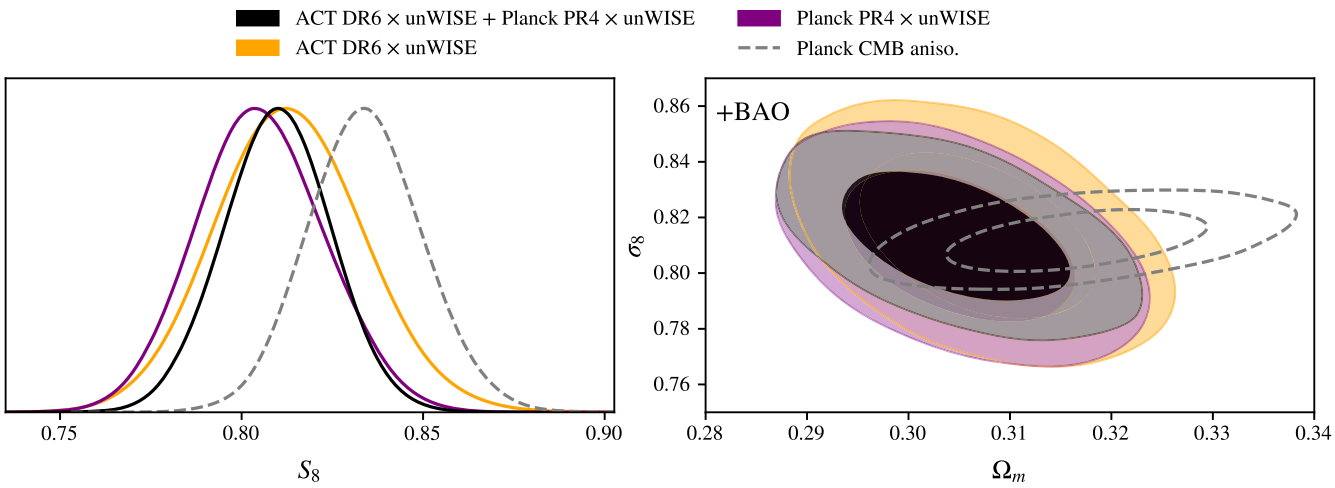

Figure 1. The main result from this work is a constraint on the amplitude of low-redshift structure captured by the parameter $S_8 \equiv \sigma_8(\Omega_m/0.3)^{0.5}$ (left). We obtain $S_8 = 0.810 \pm 0.015$ using the combination of cross-correlation measurements of the unWISE galaxies with ACT DR6 and Planck PR4 lensing reconstructions. Combined with BAO, which constrains Ω_m, we obtain constraints on σ_8 of $\sigma_8 = 0.813 \pm 0.015$ (right). Our results show no significant tension with values inferred from the primary CMB from Planck.

Section 7 focuses on various tests for systematic errors. In Section 8, we describe the theoretical model that we use for parameter inference. The parameter inference pipeline and the results of our analysis are presented in Section 9. Finally, we compare our results to other results from the literature in Section 10 and discuss the implications of our findings for the S_8 *tension*.

2. Summary of Key Results

The key results of this work are constraints on structure formation at $z \simeq 0.2$–1.6. Within a ΛCDM cosmology, the best-constrained parameter combination in the analysis presented here is approximately $\sigma_8\Omega_m^{0.45}$. This differs slightly from the best-constrained parameter combination in galaxy weak lensing analyses, $\sigma_8\Omega_m^{0.5}$. To facilitate comparisons with other probes, we mainly present constraints on the commonly used parameter $S_8 \equiv \sigma_8(\Omega_m/0.3)^{0.5}$ (Heymans et al. 2021; Abbott et al. 2022; Dalal et al. 2023; X. Li et al. 2023) in this paper; however, we also define a cross-correlation equivalent $S_8^{\times} \equiv \sigma_8(\Omega_m/0.3)^{0.45}$. CMB lensing autospectrum analyses, in contrast, primarily probe the combination $S_8^{\rm CMBL} \equiv \sigma_8(\Omega_m/0.3)^{0.25}$ (Planck Collaboration et al. 2020b; Carron et al. 2022; Madhavacheril et al. 2024; Qu et al. 2024). In this paper, we also combine BAO measurements that probe Ω_m independently of σ_8 to obtain constraints on σ_8 that are directly comparable to other probes.

When using only the cross-correlation between the ACT DR6 CMB lensing reconstruction and the two unWISE galaxy samples, Blue and Green (previously defined in Krolewski et al. 2020), as well as the autocorrelation of the galaxy samples measured on the overlapping area, we find $S_8 = 0.813 \pm 0.021$ ($S_8^{\times} = 0.817 \pm 0.019$). We combine this data with an equivalent cross-correlation analysis using the same unWISE galaxy samples and a lensing reconstruction from Planck PR4 (Carron et al. 2022) while taking into account the relevant covariance matrix and obtain improved constraints of $S_8 = 0.810 \pm 0.015$ ($S_8^{\times} = 0.814 \pm 0.014$). The posterior distributions for S_8 are shown in the left panel of Figure 1. With the addition of BAO, we find $\sigma_8 = 0.813 \pm 0.020$ from unWISE and ACT alone and $\sigma_8 = 0.813 \pm 0.015$ when combined with Planck lensing (see the right panel of Figure 1).

The model best fitting the measured C_ℓ^{gg} and $C_\ell^{\kappa g}$ is shown in Figure 2. We find a minimum $\chi^2 = 20.9$. Our model, described in detail in Section 8, includes 20 model parameters. Of those, 15 are largely prior dominated yielding an approximate number of degrees of freedom of 21 (there are a total of 26 band powers for the Blue and Green samples combined). Therefore, we estimate the probability to exceed (PTE) for the model at 0.5.

These conclusions differ from previous results from the cross-correlation of unWISE with CMB lensing reconstruction from Planck PR3 (Planck Collaboration et al. 2020b) presented in Krolewski et al. (2021). In Appendix I, we present a reanalysis of the Planck cross-correlation, finding results consistent with those presented here. We discuss the corrections and improvements that lead to the discrepancy. Other cross-correlation measurements still exhibit a preference for lower S_8 (Kitanidis & White 2020; Singh et al. 2020; Robertson et al. 2021; Chen et al. 2022b; White et al. 2022; Abbott et al. 2023b; Chang et al. 2023; Marques et al. 2024), and while some of the improvements made here (e.g., the inclusion of a Monte Carlo correction for the lensing normalization) are also relevant to those works, preliminary results show that they are likely insufficient to alleviate the discrepancy completely (J. Kim et al. 2024, in preparation; N. Sailer et al. 2024, in preparation).

Our results are in good agreement with the predictions for the amplitude of low-redshift structure obtained from the primary CMB observed by the Planck satellite (within 1.1σ for S_8 and 0.1σ for σ_8; Planck Collaboration et al. 2020a) as well as measurements from CMB lensing using either ACT (0.3σ for σ_8; Madhavacheril et al. 2024; Qu et al. 2024) or Planck (0.04σ for σ_8; Planck Collaboration et al. 2020b; Carron et al. 2022). On the other hand, our results are also not in significant tension with recent results from any one galaxy weak lensing survey such as DES, KiDS, HSC (1.1σ, 2.0σ, 0.8σ, respectively for S_8; Heymans et al. 2021; Abbott et al. 2022; Sugiyama et al. 2023), although our results favor a higher amplitude of low-redshift structure. Overall, our results do not strengthen the case for a real discrepancy in structure growth or for problems with the

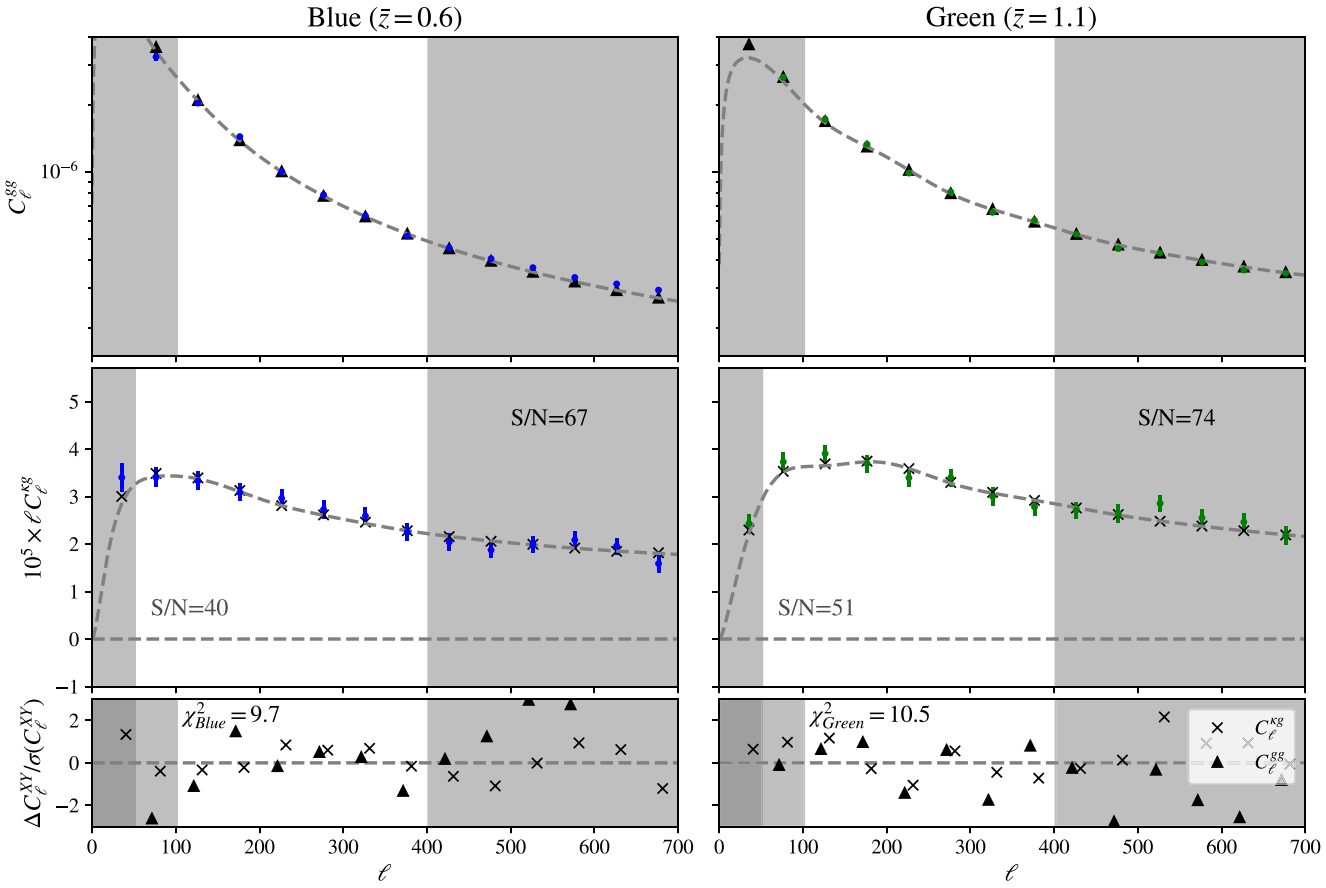

Figure 2. We measure C_ℓ^{gg} (top row) and $C_\ell^{\kappa g}$ (middle row) for the Blue and Green samples of unWISE galaxies. The total S/N in $C_\ell^{\kappa g}$ on all measured scales ($20 \leqslant \ell \leqslant 3000$) is approximately 67 and 74, respectively. Within the analysis range ($50 \leqslant \ell \leqslant 400$), we obtain an S/N of 40 and 51 for Blue and Green, respectively. The gray line shows the best fit from the joint fit to both samples, with the model residuals shown in the bottom row. The total model χ^2 for the joint fit is 21, slightly larger than the sum of the χ^2 for each of the two samples (9.7 and 10.5 for Blue and Green, respectively), due to the nonzero off-diagonal covariance between them. We estimate the model PTE at 0.5.

ΛCDM model, at least in the low-redshift, linear-scale regime to which we are sensitive.

3. The Data

We use the unWISE galaxy catalog (Krolewski et al. 2020; Schlafly et al. 2019) and lensing reconstructions from the anticipated Data Release 6 (DR6) of ACT (MacCrann et al. 2023; Madhavacheril et al. 2024; Qu et al. 2024). We also combine our cross-correlation analysis (results given in Section 9.5) with the cross-correlation obtained using the latest CMB lensing reconstruction based on data from the Planck satellite (Carron et al. 2022).

In Section 3.1, we briefly describe the unWISE samples, their selection, the measurement of their redshift distribution, and the mitigation of observational systematics. Subsequently, we describe the ACT DR6 lensing reconstruction in Section 3.2 and the Planck PR4 lensing reconstruction in Section 3.3.

3.1. unWISE Galaxies

The unWISE galaxy catalog is constructed from the Wide-Field Infrared Survey Explorer (WISE) survey (Wright et al. 2010), including 4 yr of the post-hibernation NEOWISE phase (Mainzer et al. 2011, 2014). The WISE satellite mapped the entire sky at 3.4 (W1), 4.6 (W2), 12 (W3), and 22 (W4) μm, although NEOWISE only measured in bands W1 and W2, due to a lack of cryogen necessary for the longer wavelength bands. As a result, unWISE (Lang 2014; Meisner et al. 2017) is constructed only from the much deeper W1 and W2 bands.

3.1.1. Galaxy Selection

We select three galaxy samples from unWISE using W1 − W2 color cuts, called the Blue, Green, and Red samples, at $z \sim 0.6$, 1.1, and 1.5, respectively. These samples are extensively described in Krolewski et al. (2020) and Schlafly et al. (2019). The Red sample of galaxies has a significantly lower number density than the other two samples and was shown to contribute negligible constraining power (Krolewski et al. 2021). Krolewski et al. (2021) also showed that it was difficult to reproduce the Red sample in N-body simulations and to recover unbiased cosmology from simulations tuned to reproduce the properties of the Red sample. Thus, we do not use the Red sample.

In addition to the unWISE color cuts, we additionally remove any unWISE source within 2.″75 of a Gaia (Gaia Collaboration et al. 2018) point source,[42] and remove potentially spurious sources in unWISE imaging, as described in Krolewski et al. (2020). Residual stellar contamination is

[42] 2.″75 is the size of a WISE pixel, and we use it as the match radius when crossmatching unWISE and Gaia. Relative to the 6″ WISE PSF, this is similar to the 0.″5 match radius often used between optical catalogs with 1″ seeing.

<2%. As pointed out in Krolewski et al. (2020), the power spectrum of stars drops very rapidly with ℓ, such that even at $\ell \sim 50$, the stellar power spectrum multiplied by the contamination fraction is <0.5% of the galaxy autopower spectrum, compared to the 2% statistical errors of the galaxy autospectrum at that band power. In the limit that the stellar power spectrum contributes negligible power, stellar contamination simply modifies the number density in a way that is completely degenerate with the linear galaxy bias.

The unWISE mask is based on the Planck 2018 CMB lensing mask (Planck Collaboration et al. 2020b) with a Gaussian apodization of 1°, and additional cuts around bright stars, nearby galaxies, planetary nebulae, and optical diffraction spikes. Because we remove any source within 2.″75 of a Gaia point source and mask out diffraction spikes and other narrow regions around stars, the effective area within each HEALPix pixel is less than the full area of the pixel. We correct the counts in each pixel for the effective area (and mask out any pixel with <80% coverage), before applying the unWISE mask. The large-scale component of the unWISE mask, derived from the Planck lensing mask, is apodized by smoothing with a 1° FWHM Gaussian; the other components of the mask are treated as binary. The effective sky fraction after masking is $f_{\rm sky} = 0.586$.

3.1.2. Galaxy Redshift Distributions

Since the unWISE galaxies are selected from two-band photometry, it is not possible to determine photometric redshifts for individual galaxies. Instead, we use cross-correlations with Sloan Digital Sky Survey (SDSS) spectroscopy to measure the redshift distributions of the samples (e.g., Newman 2008; McQuinn & White 2013; Ménard et al. 2013). The cross-correlation between a photometric sample with unknown redshift distribution and a spectroscopic sample is proportional to the biases of the two galaxy samples and the overlap in redshift distributions. Therefore, by repeating the cross-correlation measurement over a large number of narrowly spaced spectroscopic bins and measuring the spectroscopic sample's bias in each bin, we can measure the product of the photometric sample's bias evolution and its redshift distribution. The formalism is described in Appendix C.1 and Section 5.2 of Krolewski et al. (2020).

The unWISE cross-correlation redshifts were originally presented in Krolewski et al. (2020) using spectroscopic samples from LOWZ and CMASS galaxies (Reid et al. 2016), BOSS quasars (Ross et al. 2020), and extended BOSS (eBOSS) DR14 quasars (Ata et al. 2018). Krolewski et al. (2020) only considered objects in the Northern Galactic Cap (NGC), where most of the spectroscopy lies. These tracers span the full redshift range of the unWISE samples.

We update the unWISE cross-correlation redshifts first measured in Krolewski et al. (2020) to include additional data. We use the Southern Galactic Cap (SGC) footprints for all tracers, due to the better overlap with the mostly southern ACT footprint. We replace the eBOSS DR14 quasars with the final eBOSS DR16 quasars (Ross et al. 2020), leading to a significant increase in the area (1178–4752 $\deg^2$) and number of quasars used (54,708–343,708). Finally, we also use the eBOSS DR16 LRGs (Ross et al. 2020). We do not use the eBOSS DR16 emission line galaxies (ELGs), due to the significantly smaller area compared to the LRGs or quasars (1120 $\deg^2$ versus 4202 $\deg^2$ for LRG and 4808 $\deg^2$ for quasars) and potential systematics in the ELG autocorrelation needed to measure the ELGs' spectroscopic bias. These additions significantly improve the cross-correlation redshifts at $z \sim 0.7$–2, the redshift range where most of the unWISE galaxies lie. In Appendix K, we describe the spectroscopic samples used and their relevant properties (linear and magnification biases), then discuss the impact of the additional data used.

Conveniently, cross-correlation redshifts are sensitive to the product of the galaxy bias and the number density, $b(z)dN/dz$, that appears in the dominant terms in our model (Section 8.1). The conversion from the measured correlation function to $b(z)dN/dz$ leads to a dependence on a fiducial cosmology, although we note that there is no dependence on the amplitude of the power spectrum because we require that $b(z)dN/dz$ is normalized to integrate to unity. The residual cosmology dependence is quite minor, and the correction is described in detail in Appendix C.1 (updating the heuristic correction presented in Krolewski et al. 2021). Although the spectra we measure primarily depend on $b(z)dN/dz$, the lensing magnification, and some higher-order galaxy bias terms also depend on dN/dz, which we measure by crossmatching unWISE galaxies to deep photometric redshifts from the COSMOS2015 catalog (Laigle et al. 2016). This redshift distribution is consistent with the cross-correlation $b(z)dN/dz$ assuming a simple halo occupation distribution (HOD), consistent with the unWISE number density, to determine the bias evolution $b(z)$. From the COSMOS crossmatch, we find no evidence for unWISE galaxies to lie at $z > 1.7$ (2.5) for Blue (Green), and therefore, set the smoothed redshift distribution to zero above these high-redshift thresholds.

The cross-correlation estimates of $b(z)dN/dz$ are shown in the top panel of Figure 3. We normalize the cross-correlation redshift estimates (for more details, see Section 8.1). We also show the crossmatch dN/dz from COSMOS2015 in the lower panel.

The mean bias-weighted redshift is 0.697 ± 0.023 (Blue) and 1.355 ± 0.022 (Green), with uncertainties estimated from the samples drawn according to the cross-correlation redshift error estimates. The median and uncertainty in the crossmatch redshifts were estimated in Table 2 of Krolewski et al. (2020), 0.63 ± 0.022 (Blue) and 1.09 ± 0.019 (Green); the significant difference between the bias-weighted and unweighted redshift distributions for Green is due to the strong bias evolution consistent with the simple HOD described above. The uncertainties were estimated by crossmatching to wider-area HSC DR1 photometric redshifts (Aihara et al. 2018; Tanaka et al. 2018) at $z_{\rm phot} < 1$ and extrapolating the additional variance relative to Poisson to $z_{\rm phot} > 1$ (where the HSC redshifts become unreliable).

3.1.3. Removing unWISE Correlations with Stellar Density and WISE Depth

In addition to cosmological fluctuations, the observed galaxy number densities are determined by foregrounds such as Galactic dust and stars, as well as survey depth and other imaging properties. Both foregrounds and imaging properties affect the galaxy selection. The power spectra of these contaminants are generally red; if uncorrected, they therefore add significant power to the galaxy autocorrelation at low ℓ. The standard approach for galaxy surveys is to create a set of weights that are designed to remove any relationship between

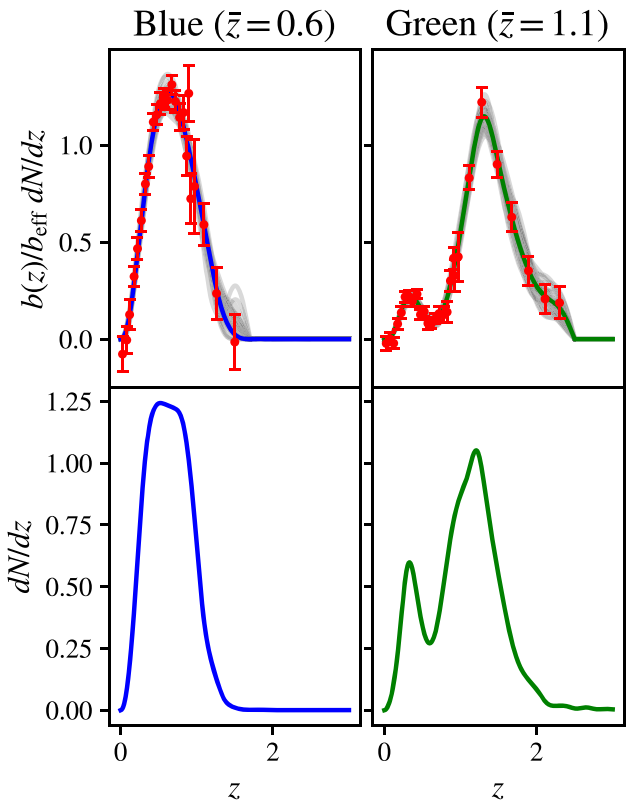

Figure 3. The Blue and Green samples of unWISE galaxies span the redshift ranges $z \simeq 0.2$–1.1 and $z \simeq 0.3$–1.8 with mean redshifts of approximately 0.6 and 1.1, respectively. In the top panel, we show the normalized estimate of $b(z)dN/dz$ obtained from cross-correlating with spectroscopic tracers from SDSS, BOSS, and eBOSS. The Blue and Green curves are the spline interpolations of the best-fitting estimates of $b(z)dN/dz$ for the two galaxy samples. We also show several noise realizations in gray and the clustering redshift measurements in red. The lower panel shows estimates of dN/dz obtained by crossmatching with photometric data from COSMOS2015.

the galaxy overdensity and various imaging property maps (Ross et al. 2012, 2017, 2020; Ata et al. 2018; Bautista et al. 2018; Elvin-Poole et al. 2018; Rodríguez-Monroy et al. 2022). Krolewski et al. (2021) did not follow this approach; instead, the authors applied a high-pass filter to the galaxy data, removing all modes of the galaxy survey at $\ell < 20$, and found that this led to better agreement between the $\ell < 100$ autocorrelation and a theory model. Additionally, Krolewski et al. (2021) did not use the galaxy autocorrelation at $\ell < 100$, where changing the Galactic mask significantly changed the shape of the unWISE autocorrelation.[43]

In this work, we update the method used in Krolewski et al. (2021) to apply weights that explicitly remove correlations between the galaxy density and maps of stellar density and WISE depth. This is similar to the approach taken by other galaxy surveys and ensures that our unWISE galaxy maps are uncorrelated with known foreground survey systematics that may affect the autocorrelation at $\ell > 100$. These weights were originally created by Krolewski & Ferraro (2022) to use the low-ℓ unWISE data in cross-correlation with CMB temperature to measure the integrated Sachs–Wolfe effect. We also no longer filter out the low-ℓ ($\ell < 20$) modes in the unWISE map. The large-scale filtering has a similar effect to weighting, also reducing large-scale power by removing correlations between systematics and the true galaxy density. However, removing large scales in harmonic space complicates the use of the MASTER algorithm Hivon et al. (2002) to obtain unbiased band powers through mode decoupling. Hence, we no longer adopt this method. This change has only a small impact on the power spectra (<0.5% on the auto- and cross-correlation corresponding to $<0.3\sigma$ in terms of the band power uncertainties; see Figure 47), but we consider the updated results more robust because the galaxy density has a significantly reduced dependence on both Galactic stellar density and WISE depth.

In the remainder of this section, we provide more detail on the construction of these weights. We measure the correlation between unWISE galaxy density and several templates: (1) Gaia stellar density; (2) and (3) W1 and W2 limiting magnitude; (4) dust extinction $E(B-V)$ from the Schlegel–Finkbeiner–Davis map corrected for cosmic infrared background (CIB) contamination (cSFD, Schlegel et al. 1998; Chiang 2023);[44] (5) neutral hydrogen column density NHI from the H14PI survey (HI4PI Collaboration et al. 2016) as an alternative dust map that is noisier than SFD but has much reduced extragalactic contamination (Chiang & Ménard 2019); (6) and (7) a 3.5 and 4.9 μm sky brightness from the DIRBE Zodi-Subtracted Mission Average;[45] (8) a DIRBE measurement of the total 4.9 μm background light at a solar elongation of 90°[46] (WISE always observed at a 90° solar elongation; Mainzer et al. 2011); and (9) a separate model of the zodiacal background light at 4.9 μm from the DIRBE Sky and Zodi Atlas[47] (Kelsall et al. 1998).

We find that the strongest correlations are with Gaia's stellar density and W2 limiting magnitude. To conservatively guard against the possibility of overfitting (Weaverdyck & Huterer 2021), we only regress against these two maps to define the systematics weights. Several other correlations are also quite significant (particularly with W1 limiting magnitude), but are significantly mitigated after weighting against stellar density and W2 depth, due to correlations between these contaminant templates. For example, both W1 and W2 depths are set by the WISE scan strategy, so the two maps exhibit the same structure.

For the Blue sample, we fit a linear trend between unWISE galaxy density and Gaia stellar density, and a three-parameter piecewise linear trend to the W2 5σ limiting magnitude. We determine uncertainties on the measured correlations using the variance of density values from 100 isotropic Gaussian mocks (no correlation with the maps of imaging systematics). For the Green sample, we use a piecewise linear fit with three free parameters for both stellar density and W2 5σ magnitude. We show the relationship between unWISE density and imaging systematics in Appendix J (Figures 45 and 46), both before and after applying weights. Before applying weights, the correlations between the galaxy density and all nine templates listed above are highly significant; after weighting, induced variations in the galaxy number density are reduced to ∼2%. While the χ^2

[43] At $\ell \gtrsim 100$, changing the Galactic (or ecliptic latitude) mask produced a scale-independent change in the unWISE autocorrelation (Krolewski et al. 2020). This is due to the fact that the selection properties of the galaxy catalog vary with Galactic or ecliptic latitude due to variations in the WISE coverage depth. This induces differences in the galaxy bias. We return to this in Section 7.2.

[44] The relationship between unWISE galaxy density and cSFD is nearly identical if we use the uncorrected SFD instead.

[45] https://lambda.gsfc.nasa.gov/product/cobe/dirbe_zsma_data_get.cfm

[46] https://lambda.gsfc.nasa.gov/product/cobe/c_90deg_skymap.html

[47] https://lambda.gsfc.nasa.gov/product/cobe/dirbe_dsza_data_get.cfm

for all correlations is significantly reduced, it is still indicative of statistically significant correlations in some cases. However, the covariance estimate is approximate (for instance, the errors are assumed to be diagonal) and potentially is an underestimate. Even the dramatic reduction in χ^2 after applying weights to correct the correlations with stellar density and W2 limiting magnitude leads to only a minor impact on the autospectrum (<3% on scales $\ell > 100$ corresponding to 0.5σ–1σ in terms of the band power uncertainties within our analysis range) and does not impact the cross-correlation spectrum significantly. We conclude that any residual correction will be negligible, given the size of our statistical errors. The impact of applying these weights on our parameter inference is $\Delta S_8 = 0.006$ ($\sim 0.3\sigma$).[48]

3.2. CMB Lensing from ACT

We use the CMB lensing convergence map reconstructed from the CMB temperature and polarization anisotropy data from the upcoming DR6 of ACT (MacCrann et al. 2023; Madhavacheril et al. 2024; Qu et al. 2024). This release is based on CMB measurements made between 2017 and 2021 (relying only on the nighttime data) at ∼90 and ∼150 GHz. It uses an early version of the ACT DR6 maps, labeled `dr6.01`.

The lensing maps cover 9400 deg^2 of the sky and are signal dominated on scales of $\ell < 150$. These maps are reconstructed using a cross-correlation-based estimator (Madhavacheril et al. 2021). Rather than using a single CMB map, the cross-correlation estimator uses several time-interleaved splits, ensuring that the instrumental noise of each map is independent. The resulting CMB lensing map is therefore insensitive to modeling of the instrumental noise.

Lensing is reconstructed with CMB scales from $600 < \ell < 3000$. The large scales of the input CMB map, $\ell < 600$, are excluded due to significant atmospheric noise, Galactic foregrounds, and a >10% correction for the large-scale transfer functions. The small scales are excluded to minimize contamination from astrophysical foregrounds like the thermal Sunyaev–Zel'dovich (tSZ) effect, the CIB, and radio sources MacCrann et al. (2023). To further mitigate extragalactic foregrounds, the lensing reconstruction uses a profile-hardened lensing estimator (Sailer et al. 2020). This involves constructing a quadratic estimator that is immune to the contribution to the CMB mode coupling arising from objects with radial profiles similar to those expected from tSZ clusters.

The baseline ACT DR6 lensing mask is constructed from a Galactic mask, which selects the 60% of the sky with the lowest dust contamination (see Qu et al. 2024, for a detailed discussion of the ACT lensing mask). As a consistency test, we also use an ACT lensing reconstruction using only the area within 40% of the sky with the lowest dust contamination (see Section 7). We will subsequently refer to these masks as the 60% and 40% Galactic masks, respectively.

3.3. CMB Lensing from Planck

The Planck PR4 lensing analysis (Carron et al. 2022) reconstructs lensing with CMB angular scales from $100 \leqslant \ell \leqslant 2048$ using the quadratic estimator. This analysis is based on the reprocessed PR4 `NPIPE` maps that incorporated around 8% more data compared to the 2018 Planck PR3 release. It also includes pipeline improvements such as optimal (anisotropic) filtering of the input CMB fields resulting in an increase of the overall signal-to-noise ratio (S/N) by around 20% compared to Planck PR3 (Planck Collaboration et al. 2020b) and a detection of the lensing power spectrum at 42σ.

Qu et al. (2024) demonstrated good consistency between the ACT and Planck PR4 lensing band powers, justifying combining the measurements at the likelihood level to obtain tighter constraints. Similar to the analysis in Qu et al. (2024) and Madhavacheril et al. (2024), we combine the cross-correlation of ACT DR6 CMB lensing and unWISE with the cross-correlation measurement between Planck PR4 CMB lensing and unWISE at the likelihood level taking into account the full relevant covariance matrix. The simulated ACT-Planck covariance matrix (see Section 6 for details) accounts for the use of identical galaxy samples, the partially overlapping areas, and the covariance between the ACT and Planck lensing reconstructions.

4. CMB Lensing Tomography

We measure the autospectra of the two galaxy samples described in Section 3.1.1 and their cross-correlation spectra with the lensing map from ACT described in Section 3.2 on the cut sky using a pseudo-C_ℓ estimator (Hivon et al. 2002).

Given two fields in the sky $a(\boldsymbol{\theta})$ and $b(\boldsymbol{\theta})$, a simple estimator of the pseudo-C_ℓ is

$$\tilde{C}_\ell^{ab} = \frac{1}{2\ell+1} \sum_{m=-\ell}^{\ell} a_{\ell m} (b_{\ell m})^\dagger, \tag{1}$$

where $a_{\ell m}$ and $b_{\ell m}$ are the spherical harmonic transforms of the fields a and b. These pseudo-C_ℓ differ from the true C_ℓ, due to mask-induced mode coupling. Their expectation value $\langle \tilde{C}_\ell \rangle$ can be related to the true C_ℓ as

$$\langle \tilde{C}_\ell \rangle = \sum_{\ell'} C_{\ell'} M_{\ell\ell'} \tag{2}$$

where $M_{\ell\ell'}$ is a mode-coupling matrix, which can be computed from the power spectrum of the mask alone. This relation can be approximately inverted if the power spectrum is assumed to be piecewise constant across a number of discrete bins (Hivon et al. 2002; Alonso et al. 2019). To perform the mode decoupling of the binned C_ℓ, we use the implementation in the `NaMaster` code[49] (Alonso et al. 2019). It should be noted that lensing reconstruction with a quadratic estimator, when performed on the masked sky, effectively convolves the mask with the signal in a nontrivial manner that is not captured exactly by the `NaMaster` algorithm. We approximate this added complexity by taking the mask used to compute the mode-coupling matrix to be the square of the ACT mask.[50] Our tests on simulations (see Section 5) suggest that this approximation performs to within better than 1% on the scales of interest. Small residuals are corrected using a transfer

[48] This includes the small change in the measured clustering redshifts due to the application of the weights (see Appendix K). The mean redshift of the Blue and Green samples changes by $\Delta\bar{z} = 0.007$ and $\Delta\bar{z} = -0.002$, respectively.

[49] https://github.com/LSSTDESC/NaMaster

[50] This is a good approximation (at least when the mask varies on much larger scales than the CMB and lensing scales of interest) since the lensing signal is reconstructed using a quadratic estimator, which reconstructs the lensing from the off-diagonal correlations in the temperature and polarization maps, which each carry one power of the mask.

function as described in Section 5. We use HEALPix maps with $\texttt{nside} = 2048$ and run NaMaster with $\ell_{\rm max}^{\rm NaMaster} = 3000$ even though we use only multipoles $\ell \leqslant 400$ in our analysis to avoid bias from the pseudo-C_ℓ method.

We measure the cross-correlation between the unWISE galaxies and the ACT DR6 lensing reconstruction (see Figure 2) with an S/N of 40 and 51 within our cosmological analysis range of $50 \leqslant \ell \leqslant 400$ for the two galaxy samples, Blue and Green, respectively. This range was set prior to unblinding. If we were able to reliably model smaller scales, we would be able to leverage even larger S/N, increasing to 67 and 74, respectively for $20 \leqslant \ell \leqslant 3000$.

The minimum multipole $\ell_{\rm min}$ is chosen based on our systematics tests presented in Section 7 to guard against contamination from large-scale observational systematics that may be correlated between the galaxy sample and the lensing reconstruction (as well as against potential misestimation of the lensing reconstruction mean field, which could lead to an underestimate of errors). The maximum multipole scale cut, $\ell_{\rm max}$, is predominantly set by the requirement for unbiased recovery of cosmological parameters, which becomes challenging with our chosen model on smaller scales (see Section 8.3). For the galaxy autocorrelation, C_ℓ^{gg}, we adopt a more conservative minimum scale cut, $\ell_{\rm min} = 100$, because the autocorrelation is more susceptible to observational systematics than the cross-correlation. On larger scales, we observe significant fluctuations of the autocorrelation signal, for example, for different choices of the mask (see Section 7.2 and also Section 7.3 in Krolewski et al. 2020).

5. Simulations for Power Spectrum Recovery and Covariance Estimation

To test recovery of unbiased power and to compute covariances we use 400 CMB lensing reconstruction simulations and appropriately correlated Gaussian simulations of the galaxy number density fields. The lensing simulations use a Gaussian lensing convergence to lens a randomly drawn CMB realization. We add realistic survey noise and masking (for details on the noise simulations see Atkins et al. 2023), and reconstruct the lensing convergence with the pipeline used on the data (Qu et al. 2024).

To generate the galaxy simulations, we measure $\hat{C}_\ell^{gg}$ and $\hat{C}_\ell^{\kappa g}$ on the two unWISE samples in narrow ℓ-bins. We fit a model with fixed cosmology and free nuisance parameters.[51] We use the ranges of $20 \leqslant \ell \leqslant 3000$ for $C_\ell^{\kappa g}$ and $100 \leqslant \ell \leqslant 3000$ for C_ℓ^{gg}. We do not fit $\hat{C}_\ell^{gg}$ and $\hat{C}_\ell^{\kappa g}$ jointly but rather individually. When fitting $\hat{C}_\ell^{gg}$ and $\hat{C}_\ell^{\kappa g}$ individually, the amplitude of the spectrum is completely degenerate with the galaxy bias. We do not assess the consistency of the galaxy bias found for the auto and cross-correlation in order not to compromise our blinding procedure. Using the model fit, we compute fiducial $C_{\ell,\rm fid}^{gg}$ and $C_{\ell,\rm fid}^{\kappa g}$, and convolve them with the appropriate pixel window function for our chosen map resolution of $\texttt{nside} = 2048$. To capture the excess noise present on large scales in $\hat{C}_\ell^{gg}$, we additionally fit a smoothly broken power law with an exponential cutoff at $\ell_{\rm noise,max} \leqslant 100$ to $\hat{C}_\ell^{gg} - C_{\ell,\rm fid}^{gg}$ on large scales. Using the Gaussian realizations of the lensing convergence field employed in generating the lensing simulations, we compute Gaussian realizations of the galaxy field that match the observed cross-correlation between CMB lensing and galaxy number density as

$$a_{\ell m}^{g} = \frac{C_{\ell,\rm fid}^{\kappa g}}{C_{\ell,\rm fid}^{\kappa\kappa}} a_{\ell m}^{\kappa} + a_{\ell m}^{g,\rm uncorrelated} + a_{\ell m}^{g,\rm noise}. \tag{3}$$

The contributions $a_{\ell m}^{g,\rm uncorrelated}$ and $a_{\ell m}^{g,\rm noise}$ are drawn such that

$$\langle a_{\ell m}^{g,\rm uncorr.} (a_{\ell' m'}^{g,\rm uncorr.})^* \rangle = \delta_{\ell\ell'}\delta_{mm'} \left(C_{\ell,\rm fid}^{gg} - \frac{(C_{\ell,\rm fid}^{\kappa g})^2}{C_{\ell,\rm fid}^{\kappa\kappa}} \right) \tag{4}$$

$$\langle a_{\ell m}^{g,\rm noise} (a_{\ell' m'}^{g,\rm noise})^* \rangle = \delta_{\ell\ell'}\delta_{mm'} C_{\ell,\rm noise}^{gg}. \tag{5}$$

This yields the correct auto- and cross-spectra. We do not include correlations between the different galaxy samples (for the purposes of the covariance computation in Section 6, we include an analytic approximation for the covariance between different samples). We measure the autocorrelations of these simulations as well as their correlation with lensing reconstruction simulations in exactly the same way as we treat the data. We then compare the measured and decoupled power spectra to the input power spectra. Note that, since the mode decoupling is only approximate, in order to make a fair comparison, we have to first convolve the input $C_{\ell,\rm fid}$ with the appropriate mode-coupling matrix (see Equation (2)) before binning them and applying the approximate decoupling applied to the measured $\hat{C}_\ell$. We find that the recovered $\hat{C}_\ell^{gg}$ and $\hat{C}_\ell^{\kappa g}$ are consistent with the inputs to within $\lesssim$1% in our cosmology range (see Figure 4). Our simulations mimic the large-scale excess of power present in the galaxy data and we use them to compute a multiplicative transfer function correcting for this effect and small inaccuracies in the mode decoupling. This excess (<0.5% for Blue and <1% for Green), which is present only in the lowest-ℓ band power in C_ℓ^{gg}, is much smaller than the uncertainty on our data band powers ($\sim$3% in the lowest-ℓ bin), but is detected significantly with 400 simulations.

6. Covariance Matrices

We use the suite of 400 Gaussian simulations of the galaxy and lensing fields discussed in Section 5 to estimate the covariance $\mathrm{Cov}(C_\ell^{XY}, C_{\ell'}^{AB})$ ($XY, AB \in \{gg, \kappa g\}$). The diagonal elements of the covariance matrix, as well as the diagonals of the $\mathrm{Cov}(C_\ell^{gg}, C_{\ell'}^{\kappa g})$ part of the covariance, are shown in Figure 5, and Figure 6 shows the correlation matrix for one of the two samples of galaxies.

We find large correlations (up to 60%) between C_ℓ^{gg} and $C_\ell^{\kappa g}$ at the same ℓ. Off-diagonal correlations (between unequal ℓ), on the other hand, are small ($\leqslant$10%). To account for the fact that the inverse of the above covariance matrix is not an unbiased estimate of the inverse covariance matrix, we rescale the inverse covariance matrix by the Hartlap factor (Hartlap et al. 2007):

$$\alpha_{\rm cov} = \frac{N_s - N_{\rm bins} - 2}{N_s - 1}. \tag{6}$$

Given our 400 simulations and the 13 combined data points for C_ℓ^{gg} and $C_\ell^{\kappa g}$, the Hartlap factor is approximately $\alpha_{\rm cov} = 0.96$

[51] The model and its parameters are described in Section 8. For this fit, we vary all nuisance parameters, including the galaxy bias, the shot noise, the higher-order bias parameters, and the principal component expansion coefficients for the cross-correlation redshifts. In total, there are eight parameters for the Blue sample and 10 parameters for Green.

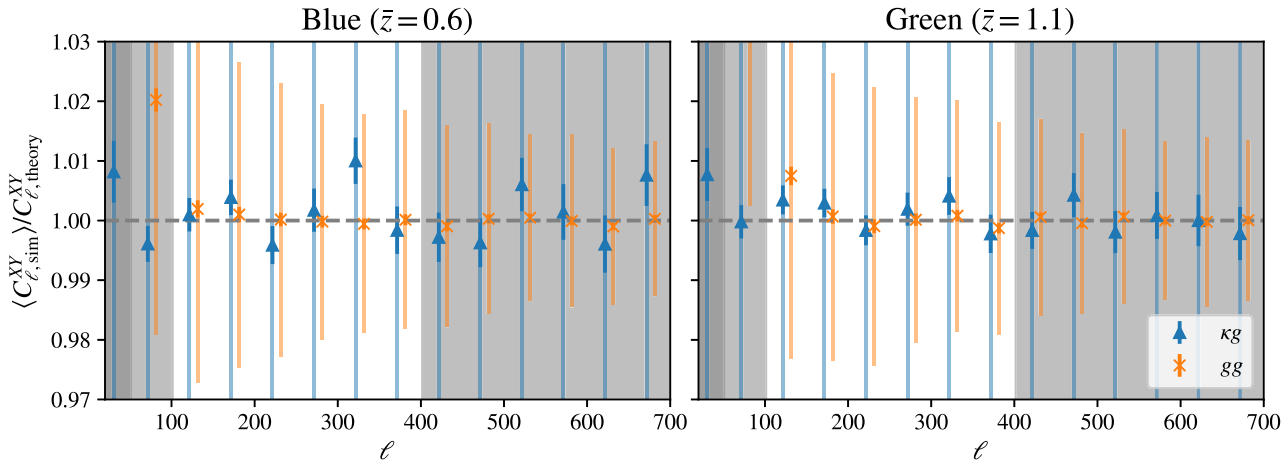

Figure 4. The recovery of C_ℓ^{gg} and $C_\ell^{\kappa g}$ on simulations when correctly accounting for the effect of mode coupling and the approximate inversion of the mode-coupling matrix is better than 1% on all scales. The lightly colored error bars indicate our measurement errors, while the dark error bars show the error on the mean of 400 Gaussian simulations.

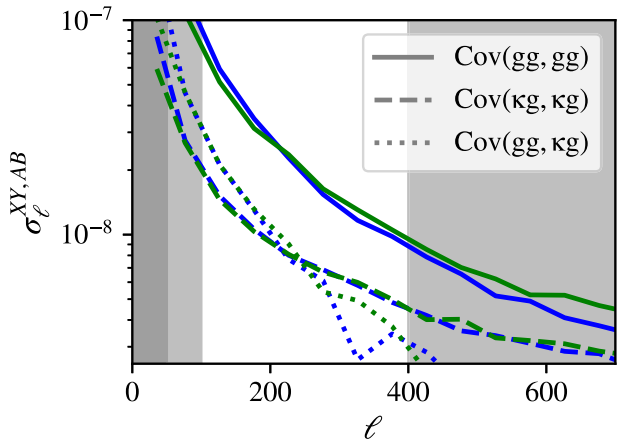

Figure 5. This figure shows the size of the diagonal elements of the covariance matrix as well as the off-diagonal covariance between C_ℓ^{gg} and $C_\ell^{\kappa g}$, which is substantial, due to the contribution from autocorrelation of the galaxy sample.

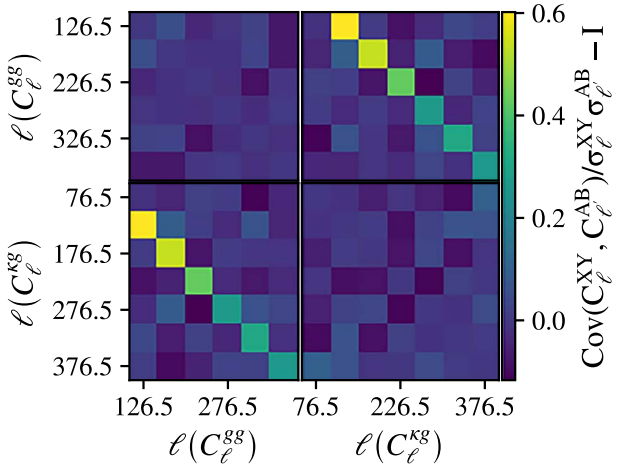

Figure 6. Correlations between C_ℓ^{gg} and $C_\ell^{\kappa g}$ are up to 60% on large scales (here shown for the Green sample of unWISE galaxies). Correlations between different scales are small; less than 10% in magnitude. We have subtracted the diagonal elements of the correlation matrix for better legibility.

for the analysis of a single sample and $\alpha_{\mathrm{cov}} = 0.93$ for the joint analysis of the two galaxy samples.

Since our Gaussian simulations do not include correlations between the two galaxy samples, we are unable to use these simulations to estimate the off-diagonal blocks of the covariance used in the joint analysis of both galaxy samples. Instead, we approximate those blocks analytically using the fiducial input spectra used for our simulations, a theory curve for the $C_\ell^{g_{\mathrm{Blue}}g_{\mathrm{Green}}}$power spectrum obtained from the fixed cosmology fits we employed to obtain the input autospectra for our Gaussian simulations (described in Section 5), and a measurement of $C_\ell^{\kappa\kappa}$, including the reconstruction noise from our simulations. Using the Gaussian covariance module implemented in `NaMaster` (Alonso et al. 2019; García-García et al. 2019), we compute a theory expression for the off-diagonal covariance. Correlations between the C_ℓ^{gg} for different samples are small (<20% on all scales of interest). The $C_\ell^{\kappa g}$, on the other hand, are significantly correlated (40%–60%) because this part of the covariance has a contribution proportional to the product of the cross-correlations, $C_\ell^{\kappa g_{\mathrm{Blue}}} C_\ell^{\kappa g_{\mathrm{Green}}}$.

In Section 9.6, we also present a combined analysis of the ACT DR6 cross-correlation with the unWISE galaxies and the corresponding cross-correlations with Planck PR4 lensing reconstructions. To estimate the covariance for this joint analysis, we proceed as follows: we use a set of 480 FFP10 CMB simulations used by Carron et al. (2022). These are Gaussian simulations that are very similar to those used in the ACT analysis, and for which there exist corresponding lensing reconstructions obtained using the Planck PR4 pipeline and the corresponding noise model. In an identical manner to the process described in Section 5, we obtain a set of correlated Gaussian galaxy realizations allowing us to estimate the covariance for the Planck cross-correlation analysis.

As described in Qu et al. (2024), we also obtained corresponding ACT DR6 reconstructions by analyzing the FFP10 simulations using the ACT DR6 pipeline, which uses a different, but overlapping, area of the sky and a different range of CMB scales to reconstruct the lensing convergence. These ACT simulations do not include the ACT noise model, but since instrumental and atmospheric noise in the ACT data are not correlated with Planck and ACT uses a lensing estimator based on cross-correlations of independent data splits, the noise does not enter the ACT-Planck covariance. The omission of the

ACT noise, in fact, improves the convergence of the cross-covariance. The partially correlated lensing reconstruction noise arising from CMB fluctuations, on the other hand, is captured by these simulations.

The correlation between the ACT and Planck lensing reconstructions is relatively small ($\lesssim$30%), as demonstrated in Qu et al. (2024). However, the cross-correlation covariance is substantial even though the survey areas only partially overlap since the identical galaxy sample is used in both cross-correlations. The correlation between the galaxy autocorrelations measured on the ACT and Planck footprints is up to 60%, while the cross-correlations are up to 50% correlated. As with the ACT-only analysis, we analytically estimate the covariance between different galaxy samples, which is small in the case of C_ℓ^{gg} (<20%) but again substantial for $C_\ell^{\kappa g}$ (up to 50%). We show a full summary of the level of off-diagonal correlations in Appendix A.

To assess the convergence of our covariance we produce an independent set of 400 further simulations. We find that the S/N is changed by $\lesssim$5% when computing the covariance using this set of simulations. In addition, we perform a consistency test with this set of simulations finding that our results are stable (see Section 9.7). We thus conclude that our covariance matrix is sufficiently converged.

6.1. Marginalization Over Uncertainty in the Lensing Normalization

As discussed in more detail in Qu et al. (2024; see in particular Appendix B therein), the unnormalized lensing reconstruction is sensitive to the product of the lensing deflection field, $\phi_{\ell m}$, and the lensing response function, $\mathcal{R}_\ell$. The lensing normalization, $\mathcal{R}_\ell^{-1}$, is, in principle, a function of the true underlying CMB two-point spectrum, but is, in practice, computed assuming a fiducial spectrum, $C_\ell^{\rm CMB,fid}$.[52] While the CMB power spectrum is well constrained by Planck, some residual uncertainty remains that must be propagated to the lensing normalization. Any deviation from the fiducial spectrum is expected to be small, and we thus Taylor expand the normalization around the fiducial value

$$\mathcal{R}_L^{-1}|_{C_\ell^{\rm CMB}} \approx \mathcal{R}_L^{-1}|_{C_\ell^{\rm CMB,fid}} \times [1 + M_L^\ell (C_\ell^{\rm CMB} - C_\ell^{\rm CMB,fid})], \quad (7)$$

where $M_L^\ell = \partial \ln \mathcal{R}_L^{-1} / \partial C_\ell^{\rm CMB}|_{C_\ell^{\rm CMB,fid}}$ is the linearized normalization correction matrix. As in Qu et al. (2024), we sample 1000 ΛCDM CMB power spectra from the ACT DR4 + Planck parameter chains presented in Aiola et al. (2020) to generate an ensemble of smooth power spectrum curves consistent with the ACT DR4 + Planck power spectrum measurements. Using Equation (7), we then propagate the scatter in these power spectra to additional uncertainties in the cross-correlation band powers. Qu et al. (2024) find this approach to be robust despite the use of smooth ΛCDM power spectra and the use of spectra drawn from the ACT DR4 + Planck chains. We note that at the time of writing, the ACT DR6 CMB power spectra were not yet available so a direct marginalization over the underlying spectra is not possible. In addition, the effect is significantly smaller for the cross-correlation than for the autospectrum, so we do not expect to incur any bias due to our treatment of the normalization marginalization.

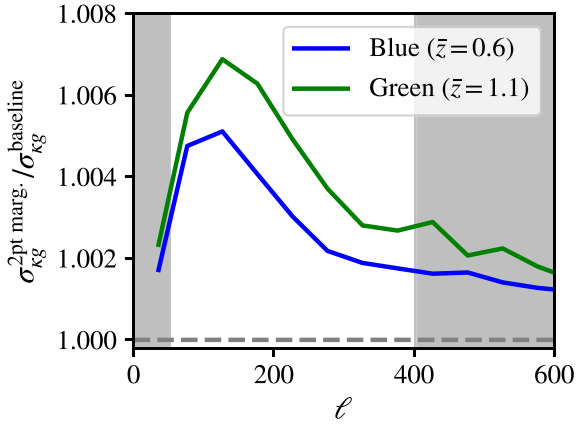

Figure 7. The contribution to the band power errors from marginalization over the lensing normalization is negligible. Nevertheless, because the contributions to the off-diagonal elements of the covariance are more significant, we include this effect in our analysis.

In Figure 7, we show the increase in the band power error bars; the change is less than 1%. For consistency with the analysis in Qu et al. (2024), and because the contributions to the off-diagonal elements of the covariance are slightly more significant, we still include these contributions in the covariance. We also implement the normalization marginalization self consistently for the covariance between different galaxy samples and the covariance between the ACT and Planck cross-correlations. However, accounting for the uncertainty in the normalization has no impact on our parameter constraints.

7. Tests for Systematic Errors

To test that our data is free from significant contamination that would affect our cosmological constraints, we perform a series of consistency checks. The tests are aimed at systematic errors in the lensing reconstruction that may correlate with the galaxy distribution; they are summarized in Section 7.1, with more details provided in Appendix B. Section 7.2 summarizes the consistency tests performed that target, in particular, spatial inhomogeneities in the galaxy samples. In addition, we estimate biases in the lensing cross-spectra due to extragalactic foreground contamination of the lensing reconstruction (see Section 7.3).

7.1. Testing for Contamination of the Lensing Reconstruction

We perform a series of null tests to demonstrate that our lensing reconstruction is free from systematic effects that could correlate with the galaxy samples. Such contamination could arise, for example, from the tSZ effect, which originates from inverse Compton scattering of CMB photons off thermal electrons in galaxy clusters; it can, if not appropriately mitigated, bias the lensing reconstruction (MacCrann et al. 2023). The tSZ signal also correlates with the large-scale matter distribution, and hence, the galaxy density. Similarly, CIB contamination, which originates from unresolved dusty galaxies, also correlates with the galaxy densities and can bias the lensing reconstruction. The ACT DR6 lensing

[52] The ACT lensing reconstruction adopts as the fiducial spectrum the ΛCDM model from Planck 2015 TTTEEE cosmology with an updated τ prior as in Calabrese et al. (2017).

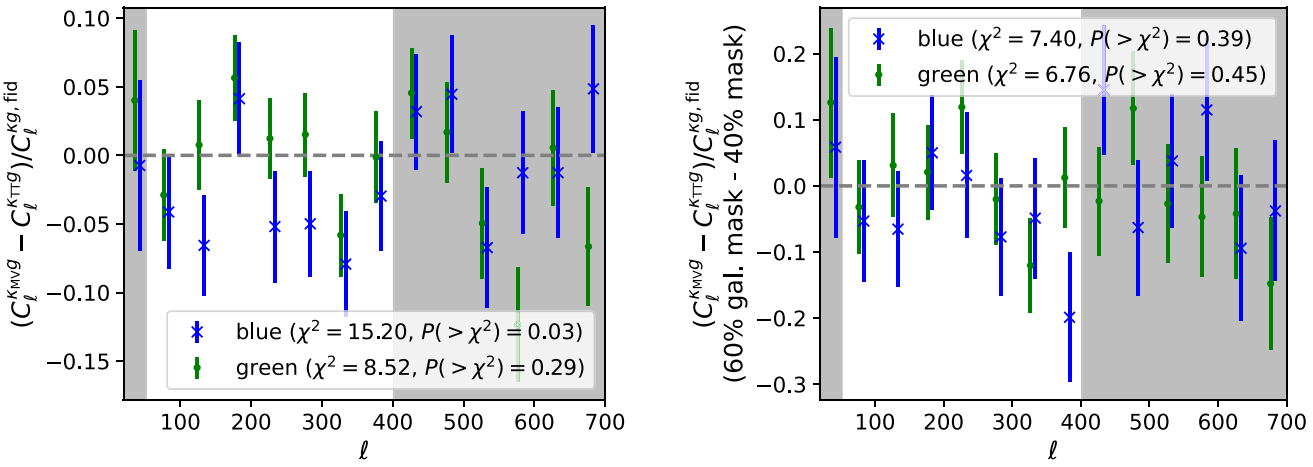

Figure 8. Here we show the band powers for two of our null tests comparing different lensing reconstructions (further tests are shown in Appendix B). When comparing band powers between the cross-correlations of the unWISE galaxies with the minimum variance lensing reconstruction and the temperature-only reconstruction, we observe a null test failure for the Blue sample of galaxies (left). As discussed in the body of the text, the one plausible systematic contamination that could cause this behavior is contamination from polarized Galactic dust emission. However, the failure does not show the scale dependence that is expected for such a failure, with the discrepancy increasing on larger scales, nor is the discrepancy observed in regions near the Galactic plane where this effect is expected to be most significant (right). As we discuss in the text, the number of observed failures is consistent with random fluctuations.

reconstruction used in this work adopts bias hardening methods to mitigate these biases (for details, see MacCrann et al. 2023; Qu et al. 2024). We verify here that contaminants are mitigated sufficiently and that potential residual contamination does not introduce significant biases in our analysis. In addition, there is, in principle, the potential of bias, due to Galactic contamination arising from a correlation of galaxy density with Galactic structure that also impacts the lensing reconstruction; this effect is easily tested and is mitigated by both masking of dust-contaminated regions and by the systematics weighting described in Section 3.1.3.

All our null tests are summarized within Appendix B, where we show χ^2 and PTEs in Table 4 and several figures showing the null test band powers (see Figures 28–33). We define a null test to be *passing* if it returns a PTE > 0.05. Overall, we consider our tests to be passing if the number of failures (PTE < 0.05) is consistent with expectations, due to random fluctuations.

We observe a total of four failures;[53] given that we perform a total of 28 null tests for $C_\ell^{\kappa g}$ across the two samples,[54] Blue and Green, this is slightly more than would be expected due to random fluctuations when neglecting correlations between the tests. We note, however, that all failing tests concern the Blue sample of galaxies, and at least three of them are highly correlated. To estimate the number of expected failures given the correlations between the null test, we performed these null tests on our 400 Gaussian simulations discussed in Section 5. We find that in 11% of cases, we observe more than the four failures found in the data. We conclude that the number of observed failures is not inconsistent with what could be expected due to random fluctuations. Nevertheless, we investigate below whether there is additional evidence that would suggest that the observed failures indicate systematic contamination of our data.

The failing tests are the following: (1) band power difference between the cross-correlations of the unWISE galaxies with the minimum variance lensing reconstruction and the temperature-only reconstruction (henceforth MV-TT, see left panel in Figure 8), (2) the difference between the cross-correlation band powers between the temperature-only and polarization-only reconstructions (henceforth TT-MVPOL), and (3) band power difference between the cross-correlations of the unWISE galaxies with the minimum variance lensing reconstruction and a reconstruction that explicitly deprojects the CIB (henceforth MV-CIBD). Additionally, we also observe PTE < 0.05 for (4) the null test between minimum variance lensing reconstruction and polarization-only reconstruction when performed using the 40% Galactic mask (henceforth MV_GAL040-MVPOL_GAL040).[55] We find the tests TT-MVPOL and MV_GAL040-MVPOL_GAL040 to be $\sim$77% and $\sim$32% correlated with MV-TT leading us to conclude that the joint failure of these three tests is not unexpected.

Regarding the failure of MV-CIBD, we note that the CIB deprojected analysis uses a slightly different lensing mask, removing a small additional area near the Galactic plane due to problems with Galactic dust. As we discuss in more detail in Section 7.2, the galaxy selection is not expected to be uniform on large scales, so the variations in the mask could lead to differences in the galaxy bias, leading null tests to fail without a significant impact on the inferred cosmology. When comparing the galaxy autocorrelation on the mask used in the CIB deprojected analysis with the baseline mask we also obtain a low PTE of 0.09. It is thus likely that the observed failure in this case is at least in part due to varying galaxy selection properties, which should not affect our cosmological inference.

One plausible systematic contamination that could induce the observed failures, given that all other null tests are passing, is contamination by polarized emission from Galactic dust. Dust emission correlates with dust extinction, which may also affect the galaxy samples. Weighting the unWISE galaxy number density to correct for a correlation with stellar density also significantly reduces the correlation with dust extinction (see Appendix J), but we nevertheless consider the possibility of residual contamination. Such contamination is expected to

[53] But no catastrophic failures with PTE < 0.01.

[54] This excludes all tests for which passing is not necessarily expected due to spatial variations in the galaxy selection, which affects the galaxy bias. See Section 7.2.

[55] The test of MV-MVPOL on the full footprint yields PTE $= 0.06$.

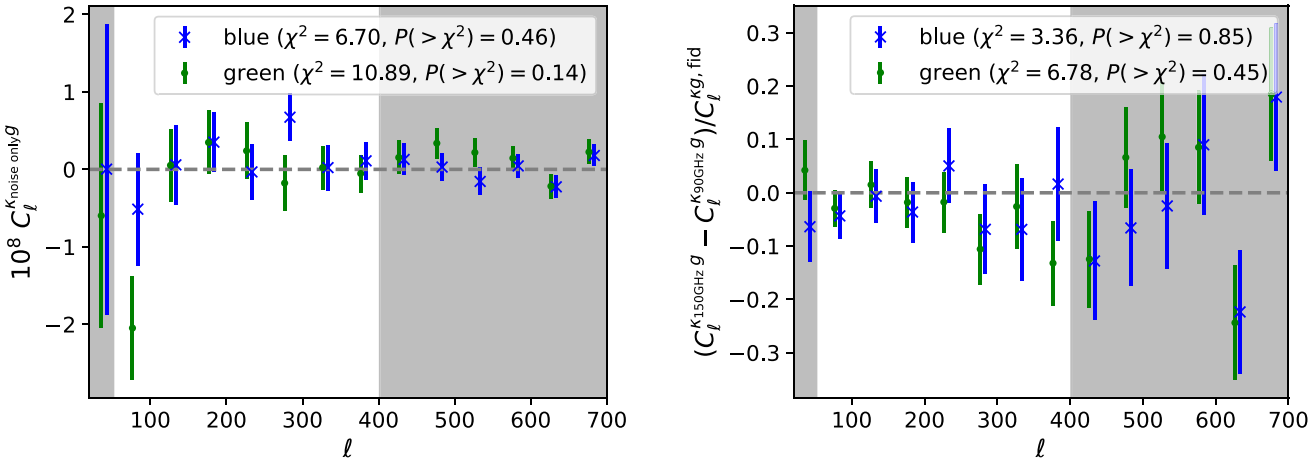

Figure 9. To test for contamination by extragalactic foregrounds, we conduct two kinds of frequency-level null tests. First, we take the difference between the observed temperature and polarization maps at 150 and 90 GHz to obtain a map containing only noise (and foregrounds) on which we perform lensing reconstruction. We then cross-correlate this map with our two galaxy samples (left). Second, we investigate the band power difference between cross-correlations measured using the reconstructions performed only on the 90 and 150 GHz data, respectively. In both cases our null tests are passed.

be significantly stronger near the Galactic plane. We hence perform the same tests of comparing minimum variance, temperature-only, and polarization-only reconstructions on the areas of the sky included in our 60% Galactic mask but not in the more restrictive 40% Galactic mask, most of which are at low Galactic latitude. We find all these tests are passing comfortably and hence, given their high sensitivity to dust contamination, conclude that there is no evidence for any contamination from Galactic dust emission.

In Section 9.7, we further discuss a parameter consistency test between our baseline analysis and an analysis using the temperature-only reconstruction. We find the inferred parameters to be consistent within the expected error on the difference.

To target extragalactic contamination, we perform a series of tests that leverage the distinctive frequency dependence of extragalactic foregrounds. We perform two kinds of frequency-level null tests. First, we take the difference between the observed temperature and polarization maps at 150 and 90 GHz to obtain a map containing only noise (and foregrounds) on which we perform lensing reconstruction. We then cross-correlate this map with our two galaxy samples. Second, we investigate the band power difference between cross-correlations measured using the reconstructions performed only on the 90 and 150 GHz data, respectively (see Figure 9 for both versions of this test). We find no failures for those tests.

7.2. Testing for Contamination and Homogeneity of the Galaxy Samples

To test the homogeneity of our observations, we perform null tests using different masks. We perform a test on the difference between cross-correlations using our 60% and 40% Galactic masks. Additionally, we construct a null test that compares our baseline footprint with a footprint restricted to ecliptic latitudes larger than 30°. Due to the unWISE survey's scan strategy, the survey depth varies with ecliptic latitude, which may affect our inference. Furthermore, zodiacal light, sunlight scattering of interplanetary dust, may contaminate the galaxy selection. Finally, we also split our sample into the NGC and SGC to perform a null test with two completely independent samples.

All tests employing the differences between different regions of the sky are complicated by the fact that the galaxy selection is not expected to be uniform on very large scales, due to the varying WISE depth of coverage. Thus, the galaxy bias, the shot noise, and the redshift distribution of our samples are expected to vary across the sky (see, for example, Figures 10 and 11 in Krolewski et al. 2019). In particular, when comparing C_ℓ^{gg}, which is measured to extremely high precision, we expect null tests to fail due to the differences in the galaxy bias and shot noise (see, e.g., Figure 10 for the comparison of different Galactic masks). However, since we marginalize over the galaxy bias, shot noise, and uncertainties in $b(z)dN/dz$ in our analysis, this does not bias our cosmological inference. We thus construct the quantity $(C_\ell^{\kappa g})^2/(C_\ell^{gg} - \hat{n}_{\rm shot})$[56], which at linear order is independent of the bias and directly proportional to S_8, the main parameter of interest in our analysis. The shot noise is here simply estimated as the inverse of the galaxy number density in the respective footprint. None of the scales used in our analysis are shot noise dominated, and hence, our tests are insensitive to small misestimations in the shot noise. Figure 11 shows the null test for two different Galactic masks using this bias-independent quantity. When considering $(C_\ell^{\kappa g})^2/C_\ell^{gg}$, we find PTE > 0.05 for all tests, but for C_ℓ^{gg} alone, we find several tests with PTE $\ll 0.05$ as expected. This implies that, up to differences in the galaxy bias, which do not affect our cosmological inference, the samples are homogeneous, yielding consistent amplitudes for different areas on the sky.

7.3. Simulation-based Test for Extragalactic Foregrounds

As a further test for systematic contamination, in particular from extragalactic foregrounds, which may contaminate the lensing reconstruction, we perform a series of tests on realistic foreground maps from the WEBSKY simulations (Stein et al. 2019, 2020). Following MacCrann et al. (2023), we make the assumption that any extragalactic contamination exclusively affects the observed CMB temperature so that $T = T_{\rm CMB} + T_{\rm fg}$, but leaves the polarization unaffected. We do not expect contaminants such as tSZ and CIB to be polarized at a

[56] For brevity we will usually neglect the shot noise subtraction in our notation.

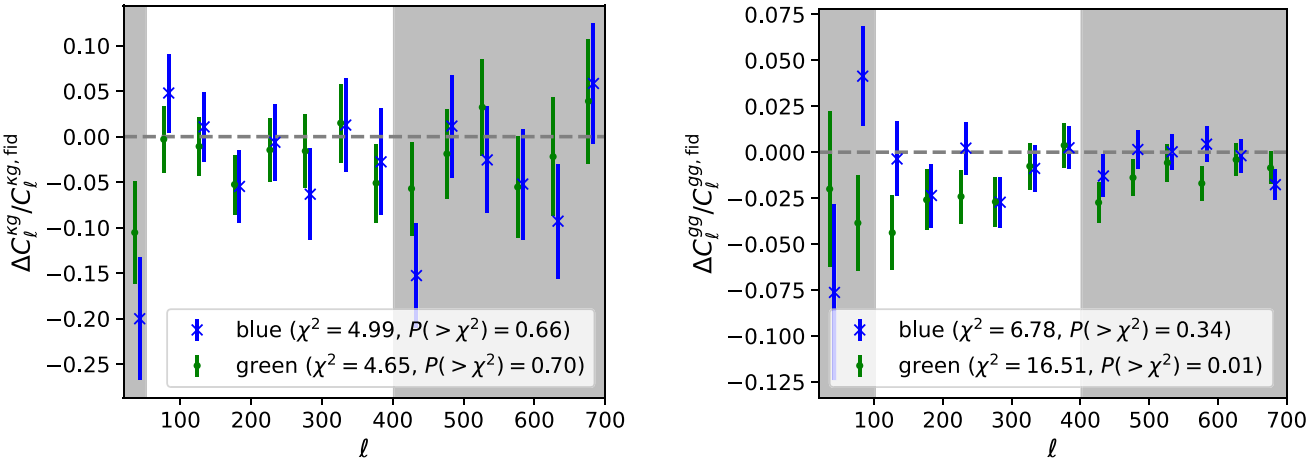

Figure 10. One of the tests targeting the spatial homogeneity of the sample is the comparison of our baseline footprint with a more conservative Galactic mask. While this null test passes for $C_\ell^{\kappa g}$ (left), we observe a failure in C_ℓ^{gg} for the Green sample (right). This is not unexpected due to varying galaxy bias arising from large-scale inhomogeneity of the galaxy selection. We thus investigate the approximately bias-independent combination $(C_\ell^{\kappa g})^2/C_\ell^{gg}$, which we observe to be passing (see Figure 11).

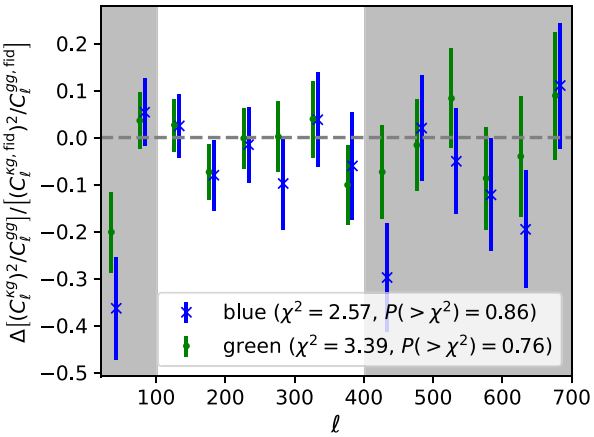

Figure 11. The combination $(C_\ell^{\kappa g})^2/C_\ell^{gg}$ is approximately independent of the linear order bias and thus less sensitive to spatial variations in the galaxy selection. Comparing this combination between our baseline mask and a more conservative Galactic mask shows consistency within the errors.

significant level for our observations, and any bright polarized sources in the DR6 data are masked and inpainted (Qu et al. 2024). Denoting the quadratic estimator used to estimate the lensing convergence field, $\hat{\kappa}$, from the two temperature fields T_A and T_B as $Q(T_A, T_B)$, and the cross-correlation with the galaxy field as $C_\ell^{Xg} = \langle Xg \rangle$, we obtain the bias on the cross-correlation of the temperature-only lensing reconstruction with the galaxy sample due to foreground contamination as (compare MacCrann et al. 2023)

$$\Delta C_\ell^{\hat{\kappa}g} = 2\langle Q(T_{\rm CMB}, T_{\rm fg})g \rangle + \langle Q(T_{\rm fg}, T_{\rm fg})g \rangle. \quad (8)$$

Assuming that the foregrounds are uncorrelated with the CMB temperature, which will be true to high accuracy, we can see that the only relevant bias arises from the correlation of a lensing-like signal, due to foreground contamination with the galaxy sample, $\langle Q(T_{\rm fg}, T_{\rm fg})g \rangle$.

We quantify the bias due to foreground contamination in terms of the bias on the cross-correlation amplitude, $A_\times$. Since we mostly aim to constrain and are sensitive to the amplitude of structure growth, this captures the relevant bias for our analysis well. The bias on $A_\times$ in terms of the uncertainty on this amplitude is given by

$$\frac{\Delta A_\times}{\sigma(A_\times)} = \frac{\sum_{\ell,\ell'} \Delta C_\ell^{\kappa g} \mathbb{C}_{\ell\ell'} C_{\ell'}^{\kappa g,\mathrm{fid}}}{\sqrt{\sum_{\ell,\ell'} C_\ell^{\kappa g,\mathrm{fid}} \mathbb{C}_{\ell\ell'} C_{\ell'}^{\kappa g,\mathrm{fid}}}}. \quad (9)$$

Here $\Delta C_\ell^{\kappa g}$ is the foreground induced bias, i.e., the cross-correlation spectrum between the galaxy sample and the lensing estimated from the foreground-only maps. Furthermore, $C_\ell^{\kappa g,\mathrm{fid}}$ is the true cross-correlation signal, and $\mathbb{C}_{\ell\ell'}$ is the appropriate covariance matrix.

In addition to estimating the lensing signal from the foreground-only maps as discussed in MacCrann et al. (2023), we populate the WEBSKY halo catalog with galaxies according to an HOD similar to the one described in Krolewski et al. (2020), with the minimum halo mass increased by 3%–5% to better account for the different mass resolution of the WEBSKY simulations. We then sample the resulting galaxy catalog to match the redshift distribution of our samples. We find a match between the spectra obtained from WEBSKY and from CROWCANYON described in Krolewski et al. (2020) to within about 5% on the scales used in our cosmology analysis.[57]

We find that in our baseline analysis, which employs frequency coadds and geometric profile hardening (Sailer et al. 2020), the residual bias is highly subdominant and can be safely neglected; $|\Delta A_\times/\sigma(A_\times)| \simeq 0.04$ for both our galaxy samples[58] (see Figure 12). Additionally, explicitly deprojecting the CIB does not yield any further gains. This is consistent with findings from MacCrann et al. (2023) and indicates that profile hardening, despite adopting a profile appropriate for tSZ clusters, also partially accounts for contamination from CIB, as was also found in Sailer et al. (2023). (For comparison, when performing no bias hardening, we find significant biases of $A_\times/\sigma(A_\times) \simeq -4.2$ and -3.1 for the Blue and Green samples, respectively.) We conclude that biases due to extragalactic foregrounds are small in comparison to the statistical errors.

[57] Since we are interested mainly in the amplitude of the fractional bias, an exact match to the data, in particular to the galaxy bias, is not required.

[58] Note that this is an upper limit on the bias since the minimum variance reconstruction we employ in our analysis also receives contributions from polarization, which contributes with a weight of about 30%.

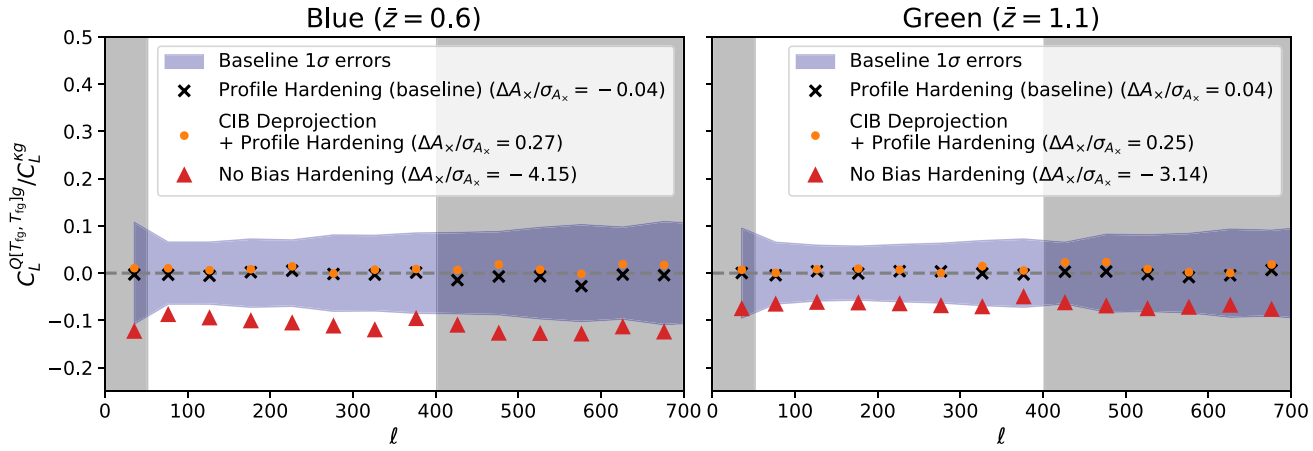

Figure 12. We estimate biases due to extragalactic foregrounds using realistic foreground simulations from WEBSKY (Stein et al. 2019, 2020). We perform lensing reconstruction on foreground-only maps using different foreground mitigation strategies and cross-correlate them with galaxy number density maps that we obtain by populating the WEBSKY halo catalog using an HOD. We find that our baseline analysis reduces all biases to $<0.05\sigma$ while the analysis without any mitigation yields significant biases (up to $\sim 4.2\sigma$).

8. The Model

In Section 4, we discussed the measurement of the angular power spectra of the unWISE galaxies, C_ℓ^{gg}, and their cross-spectra with CMB lensing reconstruction from ACT. In this section, we introduce the model to fit these data when measuring cosmological parameters. We present the 3D power spectrum model and its projection in Section 8.1 and detail our procedure for marginalizing over redshift uncertainties in Section 8.2. Finally, in Section 8.3 we test the model on N-body simulations to verify its accuracy.

8.1. Hybrid Power Spectrum Model

In the following four subsections, we detail the different components of our model. First, in Section 8.1.1, we describe our model for the three-dimensional clustering of galaxies and matter. Because we observe the galaxy number density and CMB lensing only in projection, we describe in Section 8.1.2 how we obtain the power spectra for the projected fields.

The projection kernel requires knowledge of the redshift distribution of the galaxy samples. Previously, we discussed how we measure these redshift distributions (see Section 3.1.2 with more details provided in Appendix K). Section 8.1.3 introduces the way in which we implement these redshift distribution measurements in the projected power spectra. Subsequently, in Section 8.1.4, we describe our model for the redshift evolution of all higher-order biases and the marginalization over their contribution to the observed power spectra. Finally, we show the relative contributions of various model components (Section 8.1.5).

8.1.1. 3D Power Spectra and Bias Expansion

We adopt an empirical hybrid model for the three-dimensional power spectra of the clustering of galaxies, matter, and their cross-clustering (P_{gg}, P_{mm}, and P_{mg}, respectively). This model combines fits to numerical simulations with beyond linear order terms from Lagrangian perturbation theory (LPT; Vlah et al. 2015, 2016; Modi et al. 2017; Chen et al. 2020a, 2020b). We note that these additional terms beyond linear bias are necessary to ensure unbiased results, as discussed in Section 8.3. In particular, we adopt the `HMCode` model from Mead et al. (2016) as implemented in CAMB[59] (Lewis et al. 1999; Howlett et al. 2012) and the formalism for P_{gg} and P_{gm} described in Kitanidis & White (2020) with some substitutions described below (similar to Pandey et al. 2020).

In the LPT model, the bias expansion for the clustering of galaxies and their cross-clustering with matter is given by (Modi et al. 2017; Chen et al. 2020a, 2020b; Kitanidis & White 2020)

$$\begin{aligned} P_{gg} = &\left(1 - \frac{\alpha_{\rm auto} k^2}{2}\right) P_Z + P_{1-\rm loop} \\ &+ b_{1,L} P_{b_1} + b_{2,L} P_{b_2} + b_{s,L} P_{b_s} \\ &+ b_{1,L} b_{2,L} P_{b_1 b_2} + b_{1,L} b_{s,L} P_{b_1 b_s} + b_{2,L} b_{s,L} P_{b_2 b_s} \\ &+ b_{1,L}^2 P_{b_1^2} + b_{2,L}^2 P_{b_2^2} + b_{s,L}^2 P_{b_s^2} + P_{\rm shot\ noise}, \end{aligned} \tag{10a}$$

$$\begin{aligned} P_{mg} = &\left(1 - \frac{\alpha_{\rm cross} k^2}{2}\right) P_Z + P_{\rm one-loop} \\ &+ \frac{b_{1,L}}{2} P_{b_1} + \frac{b_{2,L}}{2} P_{b_2} + \frac{b_{s,L}}{2} P_{b_s}, \end{aligned} \tag{10b}$$

where $b_{X,L}$ are free bias coefficients and P_Z and $P_{\rm one-loop}$ are the Zel'dovich and one-loop power spectra, the lowest-order contributions to the theory. The P_Z, $P_{\rm one-loop}$, and higher-order contributions (P_{b_2}, P_{b_s}, etc.) can be computed analytically from the linear power spectrum $P_{mm,\rm lin}$.

The term

$$P_{mm} = \left(1 - \frac{\alpha k^2}{2}\right) P_Z + P_{\rm one-loop} \tag{11}$$

captures the dark matter contribution to the clustering (Vlah et al. 2015). The parameter α allows marginalization over the impact from small-scale physics beyond the cutoff of the theory, and is generically not assumed to be identical in the auto- and cross-clustering. This contribution is what the `HMCode` model emulates numerically, which motivates the following substitution:

$$P_{mm} = \left(1 - \frac{\alpha k^2}{2}\right) P_Z + P_{\rm one-loop} \rightarrow P_{mm,\rm HM}. \tag{12}$$

[59] https://github.com/cmbant/CAMB

This approach incorporates all higher-order effects in the dark matter clustering.

The remaining terms in the LPT bias expansion encode the response of the galaxy clustering to the large-scale matter distribution. Assuming that at lowest-order galaxies are linearly biased tracers of the matter density yields

$$P_{gg} = b_{1,E}^2 P_{mm,\mathrm{HM}} + \text{higher order terms and} \tag{13a}$$

$$P_{mg} = b_{1,E} P_{mm,\mathrm{HM}} + \text{higher order terms}, \tag{13b}$$

where $b_{1,E}$ is the lowest-order Eulerian bias. It is related to the lowest-order bias in the Lagrangian formalism, $b_{1,L}$, as $b_{1,E} = b_{1,L} + 1$ (we use subscripts E and L to distinguish Eulerian and Lagrangian biases). Assuming furthermore that the impact of small-scale physics on the cross- and auto-clustering is identical (i.e., applying the substitution from Equation (12) to both Equations (10a) and (10b), setting $\alpha = \alpha_{\mathrm{auto}} = \alpha_{\mathrm{cross}}$) then requires the further substitutions

$$P_{b_1} \to 2P_{mm,\mathrm{HM}} \quad \text{and} \tag{14a}$$

$$P_{b_1^2} \to P_{mm,\mathrm{HM}}, \tag{14b}$$

to recover the linear bias model at the lowest order.

With these substitutions, the galaxy–galaxy, galaxy-matter, and matter–matter power spectra are given in detail by

$$\begin{aligned} P_{gg}(k, z) = {} & b_{1,E}^2(z) P_{mm,\mathrm{HM}} + b_{2,L}(z) P_{b_2}(k, z) \\ & + b_{s,L}(z) P_{b_s}(k, z) \\ & + b_{1,L}(z) b_{2,L}(z) P_{b_1 b_2}(k, z) \\ & + b_{1,L}(z) b_{s,L}(z) P_{b_1 b_s}(k, z) \\ & + b_{2,L}(z) b_{s,L}(z) P_{b_2 b_s}(k, z) \\ & + b_{2,L}^2(z) P_{b_2^2}(k, z) \\ & + b_{s,L}^2(z) P_{b_s^2}(k, z) + P_{\text{shot noise}}, \end{aligned} \tag{15a}$$

$$\begin{aligned} P_{gm}(k, z) = {} & b_{1,E}(z) P_{mm,\mathrm{HM}} + \frac{b_{2,L}(z)}{2} P_{b_2}(k, z) \\ & + \frac{b_{s,L}(z)}{2} P_{b_s}(k, z), \quad \text{and} \end{aligned} \tag{15b}$$

$$P_{mm}(k, z) = P_{mm,\mathrm{HM}}(k, z). \tag{15c}$$

Approaches similar to this have been shown to work well on simulations (e.g., Pandey et al. 2020).

To compute the effective field theory contributions, P_{b_2}, P_{b_s}, etc., we rely on the `velocileptors` code.[60] Following Chen et al. (2022b), we adopt the baryon and dark-matter-only power spectrum for all contributions to P_{gg} (i.e., we exclude the contribution from neutrinos, which, to a good approximation, do not cluster and hence do not contribute to the galaxy clustering). For $P_{mg,}$ we use the cross-power spectrum between the baryon and dark matter density on the one hand and the total matter density (including neutrinos) on the other.

[60] https://github.com/sfschen/velocileptors

8.1.2. Power Spectra of Projected Fields

Since we observe the galaxy overdensity and CMB lensing only projected along the line of sight, we require a model for the projected galaxy–galaxy and galaxy-CMB lensing power spectra. To obtain those spectra we employ the Limber approximation[61] (Limber 1953; LoVerde & Afshordi 2008)

$$C_\ell^{gg} = \int d\chi \frac{W_g^2(z)}{\chi^2} P_{gg}(k\chi = l + 1/2, z), \tag{16}$$

$$C_\ell^{\kappa g} = \int d\chi \frac{W_g(z) W_\kappa(z)}{\chi^2} P_{gm}(k\chi = l + 1/2, z). \tag{17}$$

Here χ is the comoving distance to redshift z along the line of sight. The galaxy and lensing projection kernels, W_g and W_κ, are given by

$$W_g(z) = H(z) \frac{dN}{dz} \quad \text{and} \tag{18}$$

$$W_\kappa(z) = \frac{3}{2} \Omega_m H_0^2 (1 + z) \frac{\chi(\chi_\star - \chi)}{\chi_\star}. \tag{19}$$

The total matter density, Ω_m, includes the density of neutrinos that are nonrelativistic at low redshifts. Additionally, $\chi_\star$ is the comoving distance to the last scattering surface, $H(z)$ is the Hubble rate, and $H_0 = H(z = 0)$.

In addition to the contribution from the correlation of galaxy clustering with the matter field that gives rise to the CMB lensing, the measured angular power spectra also contain relevant contributions from the lensing magnification bias (Krolewski et al. 2020). This effect arises because individual galaxies may be gravitationally lensed and magnified (or demagnified) by foreground structure, affecting our sample selection by artificially increasing (or decreasing) the magnitude of a galaxy in a way that is correlated with the large-scale structure. We use the index μ to denote quantities related to the magnification bias. We model the additional contributions as

$$C_\ell^{g\mu} = \int d\chi \frac{W_g(z) W_\mu(z)}{\chi^2} P_{gm}(k\chi = l + 1/2, z), \tag{20}$$

$$C_\ell^{\kappa\mu} = \int d\chi \frac{W_\kappa(z) W_\mu(z)}{\chi^2} P_{mm}(k\chi = l + 1/2, z), \text{ and} \tag{21}$$

$$C_\ell^{\mu\mu} = \int d\chi \frac{W_\mu(z) W_\mu(z)}{\chi^2} P_{mm}(k\chi = l + 1/2, z) \tag{22}$$

with the lensing magnification kernel given by (Villumsen 1995; Moessner et al. 1997; Bartelmann & Schneider 1999)

$$\begin{aligned} W_\mu(z) = {} & (5 s_\mu - 2) \frac{3}{2} \Omega_m H_0^2 (1 + z) \\ & \times \int_\chi^{\chi_\star} d\chi' \frac{\chi(\chi' - \chi)}{\chi'} H(z') \frac{dN}{dz'}. \end{aligned} \tag{23}$$

The parameter $s_\mu \equiv d \log_{10} N / dm$ is the response of the galaxy number density to a change in magnitude. This parameter is measured from the data by perturbing the photometry of the unWISE galaxies and reapplying the selection criteria (see

[61] Using the implementation in the `Core Cosmology Library` package (https://github.com/LSSTDESC/CCL; Chisari et al. 2019), we checked that the leading beyond-limber contribution, arising from RSDs, is less than 0.1% on all scales used in our analysis and thus safely negligible.

Appendix D of Krolewski et al. 2020). However, in principle, the magnification bias parameter is the derivative of the number density of the true underlying galaxy population (rather than the observed one), which is unknown. In addition, Krolewski et al. (2020) showed some variations of s_μ with survey depth (by about 5%; see Figure 20 in Krolewski et al. 2020). Therefore, we marginalize over this parameter in our analysis with a conservative 10% Gaussian prior. We note that $C_\ell^{\kappa\mu}$ and $C_\ell^{\mu\mu}$ depend on the matter–matter power spectrum, P_{mm}. The total observed galaxy–galaxy and galaxy-CMB lensing spectra are then given by $C_\ell^{gg} + 2C_\ell^{g\mu} + C_\ell^{\mu\mu}$ and $C_\ell^{\kappa g} + C_\ell^{\kappa\mu}$.

8.1.3. Redshift Distribution and Bias Evolution

While the lensing projection kernel (Equation (19)) is determined by the cosmological model alone, the galaxy and magnification bias kernels (Equations (18) and (23)) depend on measurements of the galaxy redshift distributions, dN/dz. As discussed in Section 3.1.2, we have two ways of measuring the redshift distribution of the unWISE samples, one relying on cross-correlations with spectroscopic tracers and one relying on crossmatching, with a deep photometric sample from COSMOS.

Conveniently, cross-correlation redshifts are sensitive to the product $b_{1,E}(z)dN/dz$. We normalize those redshift distributions so that

$$W^{\rm xc}(z) = \frac{\left(\widehat{b_{1,E}(z)\frac{dN}{dz}}\right)_{\rm cross-correlation}}{b_{1,E}^{\rm eff}}, \tag{24}$$

where $b_{\rm eff}$ is chosen such that $\int dz W^{\rm xc}(z) = 1$. In this context, $\widehat{X}$ shall denote our observational estimate of the quantity X. Wherever the product $b_{1,E}(z)W_g(z)$ appears in our model, we thus use $b_g W^{\rm xc}(z)H(z)$,[62] where b_g is a free parameter in our analysis over which we marginalize. In this manner, we encode the correct bias evolution for all the dominant terms in C_ℓ^{gg} and $C_\ell^{\kappa g}$ while allowing the amplitude of the bias to vary. This comes at the cost of introducing a dependence on the fiducial cosmology assumed when computing the cross-correlation redshifts. In Appendix C.1, we discuss how we correct for this effect. Where $W_g(z)$ appears in a term that is not also proportional to $b_{1,E}$, we rely on the crossmatch derived redshifts, defining a normalized kernel

$$W_g(z) \rightarrow W^{\rm xm}(z)H(z) = \frac{\left(\widehat{\frac{dN}{dz}}\right)_{\rm cross-match}}{N}H(z) \tag{25}$$

with N chosen again such that $\int dz W^{\rm xm}(z) = 1$. A special case arises for terms proportional to $b_{1,L}(z)W_g(z)$. Since $b_{1,L} = b_{1,E} - 1$ we model these terms as $b_{1,L}(z)W_g(z) \rightarrow b_g W^{\rm xc}(z)H(z) - W^{\rm xm}(z)H(z)$.

8.1.4. Redshift Evolution of Higher-order Biases and Marginalization

In the preceding section, we discussed the inclusion of the bias evolution for the lowest-order bias. The higher-order biases, relevant to the LPT terms in our model, also exhibit significant redshift evolution. Keeping with the model in Krolewski et al. (2021), we capture the redshift dependence of $b_{2,L}$ and $b_{s,L}$ (in part) by defining them through coevolution relations as functions of the lowest-order bias $b_{1,L} = b_{1,E} - 1$. To obtain $b_{2,L}^{\rm co-evol.}(b_{1,L})$ and $b_{s,L}^{\rm co-evol.}(b_{1,L})$, we use the relations presented in Abidi & Baldauf (2018; see their Figure 8, and for our fit to those measurements, see Figure 13), which are measured from clustering of protohalos in N-body simulations. Since we do not know $b_{1,L}$, this requires assuming a fiducial redshift evolution, $b_{1,L}^{\rm fid}$, which we adopt from Krolewski et al. (2020, 2021),

$$b_{1,L}^{\rm fid}(z) = 0.8 + 1.2z - 1 \text{ Blue} \tag{26a}$$

$$b_{1,L}^{\rm fid}(z) = \max(1.6z^2, 1) - 1 \text{ Green} \tag{26b}$$

$$b_{1,L}^{\rm fid}(z) = \max(2z^{1.5}, 1) - 1 \text{ Red}. \tag{26c}$$

This evolution is consistent with the observed clustering and with the expected bias evolution from a simple HOD of the unWISE samples (Krolewski et al. 2020). We show these fiducial bias evolutions as well as the resulting evolution of $b_{2,L}$ and $b_{s,L}$ in Figure 14.

In going beyond the model described in Krolewski et al. (2021), we allow some freedom in the coevolution by adding a free offset over which we marginalize in our analysis. The higher-order biases are thus given effectively as $b_{X,L}(z) = b_{X,L}^{\rm co-evol.}(b_{1,L}^{\rm fid}(z)) + c_{X,L}$. To set priors on each $c_{X,L}$, we run our pipeline on the N-body simulations we use for model verification while holding the cosmology fixed. We then take the prior on $c_{X,L}$ to be a Gaussian approximation of the resulting posterior but increase the width (if necessary) such that the standard coevolution is allowed at 1σ, i.e., $\mathcal{N}(\mu_{c_{X,L}}, \max(|\mu_{c_{X,L}}|, \sigma_{c_{X,L}}))$.

Since we observe only projected spectra, redshift-dependent deviations from the fiducial bias evolution can largely be absorbed in an effective amplitude. To demonstrate this, we tested a rescaling of the fiducial bias evolution (in addition to the free offset), letting $b_{X,L}(z) = a_{X,L} b_{X,L}^{\rm co-evol.}(b_{1,L}^{\rm fid}(z)) + c_{X,L}$, where both $a_{X,L}$ and $c_{X,L}$ are free parameters. From runs on simulations, we found these parameters to be nearly completely degenerate. Furthermore, we tested including an offset in the form of a third-degree polynomial $b_{X,L}(z) = b_{X,L}^{\rm co-evol.}(b_{1,L}^{\rm fid}(z)) + c_{X,L} + \sum_{n=1}^{3} c_{X,L}^{(n)}(1+z)^n$ after minimizing over the constant offset within the prior range used in our model (while holding all other parameters fixed to their best-fit values) we find no significant deviations in the goodness of fit ($\Delta\chi^2 < 1$) even for a bias evolution, which differs significantly ($\mathcal{O}(1)$) from the fiducial one. This indicates that the

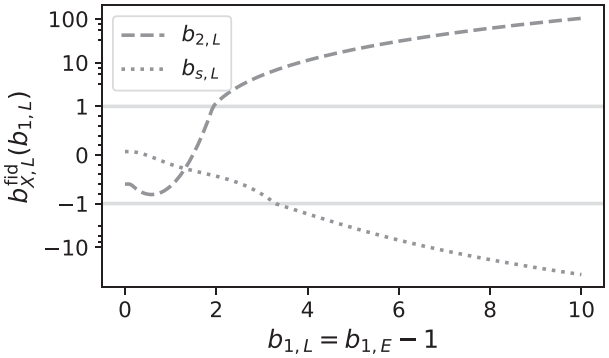

Figure 13. We show here the coevolution relations between the higher-order Lagrangian bias parameters and the lowest-order bias used to obtain the redshift evolution of higher-order biases. The higher-order Lagrangian biases, $b_{2,L}$ and $b_{s,L}$, are given as functions of the lowest-order bias, $b_{1,L}$. These relations are derived from fits to numerical simulations presented in Abidi & Baldauf (2018).

[62] Note the factor of the Hubble rate $H(z)$ in the definition of $W_g(z)$; Equation (18)).

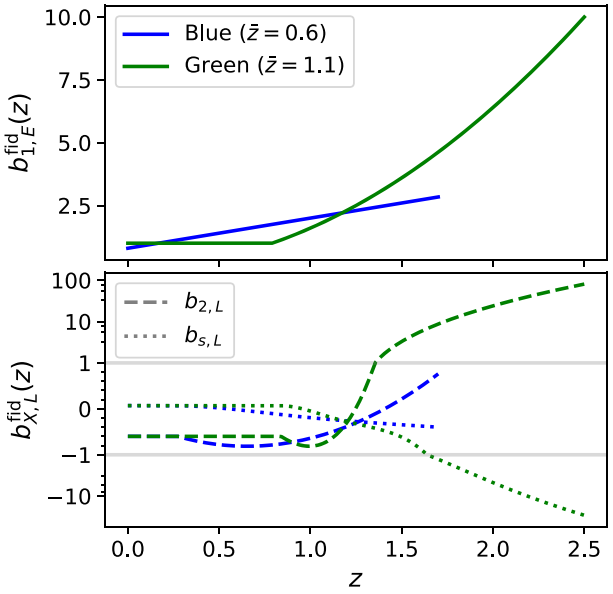

Figure 14. Here we show the fiducial redshift evolution of lowest-order linear bias parameters (taken from Krolewski et al. 2020, 2021; upper panel) and the resulting Lagrangian bias evolution for both unWISE samples (lower panel). The redshift evolution of the higher-order biases is obtained by applying the coevolution relation shown in Figure 13 to the fiducial lowest-order bias.

parameterization through a single offset allows for sufficient freedom in the higher-order contributions to the spectrum.

In simulations, we also find the cosmology dependence of all higher-order contributions to the final projected spectra (arising from P_{b_2}, P_{b_s}, $P_{b_1 b_2}$, etc.) can effectively be absorbed into a change in the amplitude of those model components. We thus choose to compute them at a fixed fiducial cosmology taken to be the mean cosmology found in Planck Collaboration et al. (2020a).[63]

8.1.5. Relative Contributions of Model Components

In Figure 15, we show the contributions of various model components assuming the best-fitting cosmology for the joint fit to the cross-correlation of the Blue and Green samples with ACT DR6, including BAO information on the matter density (as described in Section 9.5). The contribution of higher-order terms to the total C_ℓ^{gg} is at most 7% for the Blue sample and 5% for the Green sample. While lensing magnification does not exceed 1% for the Blue sample, it contributes up to 5% to the signal on large scales for the Green sample. For $C_\ell^{\kappa g}$, the contributions from higher-order terms are even more subdominant (at most 2% for the Blue sample; see Figure 16). Lensing magnification contributes about 6% to the observed $C_\ell^{\kappa g}$ for the Green sample. Since these contributions to our model are subdominant, we do not expect our results to be sensitive to the detailed modeling choices (e.g., the exact higher-order bias evolution or the estimate of the magnification bias parameter).

In summary, our power spectrum model has four free bias parameters per galaxy sample. This includes the amplitude of the linear order bias, free offsets to the fiducial redshift evolution for the second-order and shear biases, and the magnification bias parameter. In addition, we will also marginalize over the amplitude of the shot noise contribution. In Section 9.7, we return to the impact of the different model components on our cosmological inference. We find that neglecting all higher-order corrections only yields a small shift in S_8 ($\Delta S_8 \simeq 0.1\sigma$). However, it is known that the observed clustering statistics are, in principle, sensitive to the higher moments of the matter distribution and tidal effects, which are encoded in the LPT terms. The impact the inclusion of these terms has on the mean inferred cosmological parameters is sensitive to the value of the higher-order biases in our data, which is a priori unknown and so we conservatively maintain those free parameters in our model. This approach propagates the modeling uncertainty arising from our lack of knowledge of the higher-order biases, which our data does not constrain well to the inferred cosmological parameters of interest. Neglecting the magnification bias terms leads to a shift of $\Delta S_8 \simeq -0.2\sigma$, but again since such an effect is, in principle, expected, we include it in our model to appropriately propagate the resulting uncertainties.

8.2. Marginalization Over Redshift Uncertainties

As discussed in Section 3.1.2 and Krolewski et al. (2020, 2021), the measured redshift distribution of galaxies is subject to significant statistical errors. Here we describe a method based on a principal component analysis (PCA) for propagating these uncertainties to our cosmological results.

In principle, both our measurements of the redshift distribution, those based on crossmatching with spectroscopic samples, $W^{\rm xm}(z)$, as well as those based on cross-correlations with spectroscopic surveys, $W^{\rm xc}(z)$, are affected by statistical uncertainty. However, the contribution to the uncertainty in our final spectra from any uncertainty in the crossmatch redshift distributions is expected to be subdominant since those measurements only affect terms that do not depend on the galaxy bias, and these terms contribute at most at the few percent level to the total signal (see Figures 15 and 16). Hence, we choose to neglect this source of uncertainty and focus instead on the uncertainty in the cross-correlation-based redshift distribution measurements.

We generate 1000 realizations of $W^{\rm xc} \propto b(z)dN/dz$ as described in Krolewski et al. (2021). We draw 1000 Gaussian realizations of the cross-correlation redshift estimate using the noise covariance obtained for those measurements and interpolate the resulting samples using a B-spline with a positivity constraint before normalizing them. We then perform a PCA on the difference between these realizations and the normalized spline interpolation of the best fit, $\hat{W}^{\rm xc}(z)$. We show the resulting principal components in Figure 17. In our cosmology analysis, we then use

$$W^{\rm xc}(z) = \hat{W}^{\rm xc}(z) + \Delta W_0^{\rm xc}(z) + \sum_{i=1}^{n} c_i \Delta W_i^{\rm xc}(z), \qquad (27)$$

where $\Delta W_0^{\rm xc}(z)$ is the mean difference between the 1000 random realizations and the best fit and $\Delta W_i^{\rm xc}(z)$ are the ith principal components. The coefficients c_i are marginalized over. We keep principal components up to $n = 3$ and 5 for the Blue and Green samples, respectively. This n is chosen to account for at least 90% of the variance observed in the realizations. Due to the projection over redshift, oscillatory features in the redshift distribution of galaxies as expressed by higher principal components (which have an increasing number of nodes) will contribute less to the projected power spectrum. Therefore, it is expected that while we capture only 90% of the variance in the bias-weighted redshift distribution, a larger fraction of the induced power spectrum variance is due to the

[63] Adopting the analysis including TT, TE, and EE spectra for multipoles $\ell \geqslant 30$, as well as the EE spectrum for multipoles $2 \leqslant \ell \leqslant 29$, Planck lensing, and BAO.

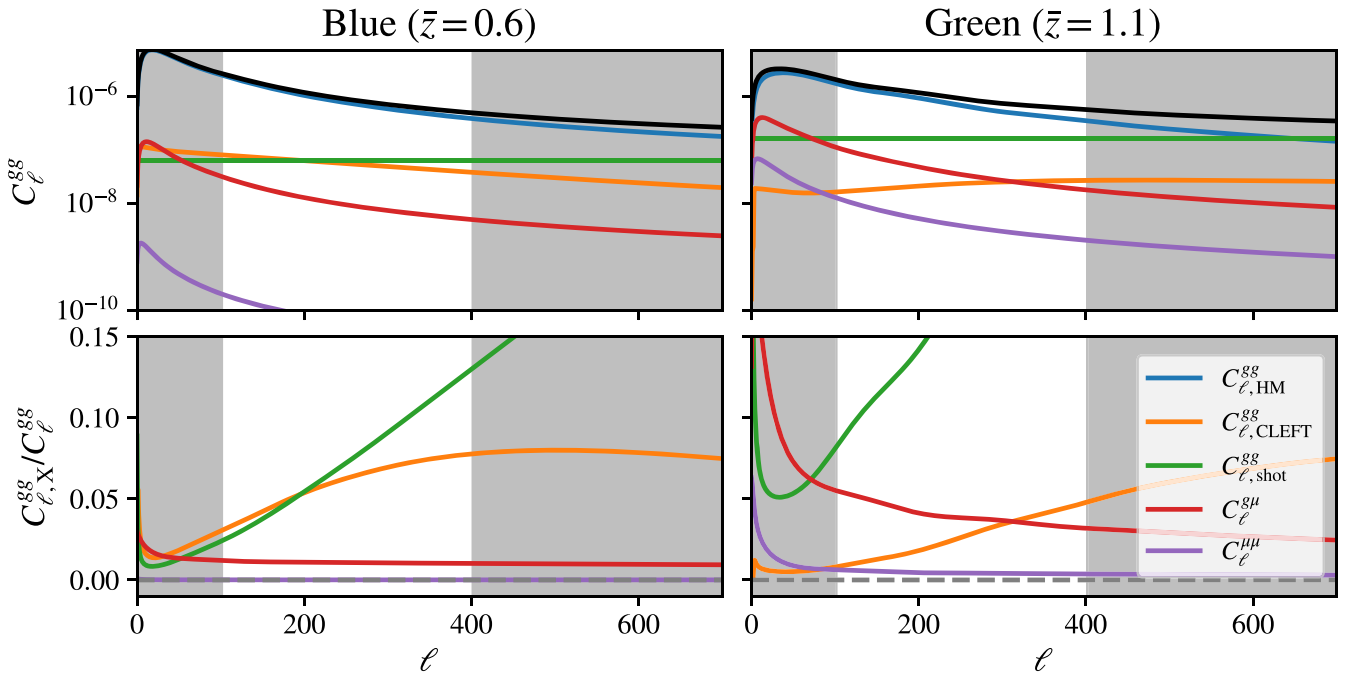

Figure 15. Contribution of various model components to C_ℓ^{gg} ($C_{\ell,\mathrm{HM}}^{gg}$: `HMCode` matter power spectrum; $C_{\ell,\mathrm{CLEFT}}^{gg}$: higher-order terms; $C_{\ell,\mathrm{shot}}^{gg}$: shot noise; $C_\ell^{g\mu}$ and $C_\ell^{\mu\mu}$: magnification bias). The most important contributions to the galaxy power spectrum arise from the `HMCode` contribution at the lowest order and the shot noise. The higher-order contributions contribute at most 7% and 5% of the signal for the Blue and Green samples, respectively. While lensing magnification plays a negligible role for the Blue sample, it contributes up to 5% of the signal on large scales for the Green sample. This figure assumes the best-fitting cosmology for the joint fit to the cross-correlation of the Blue and Green samples with ACT DR6.

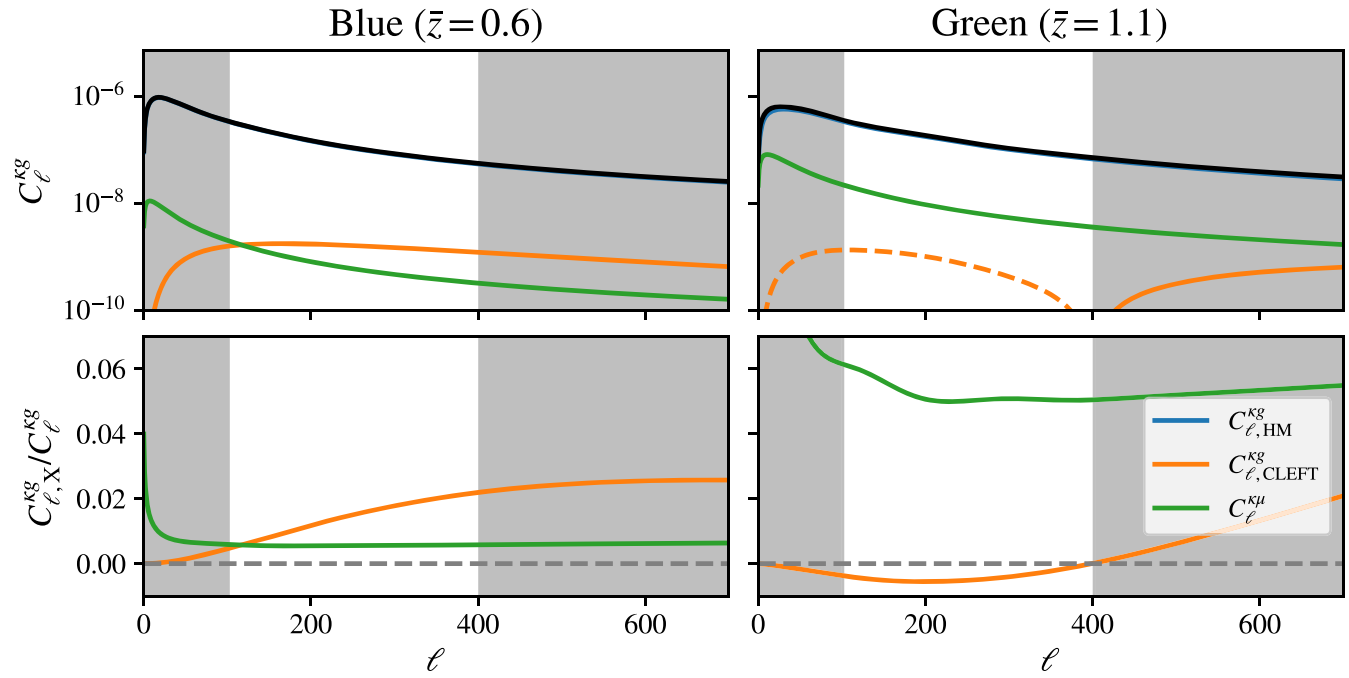

Figure 16. Contribution of various model components to $C_\ell^{\kappa g}$ ($C_{\ell,\mathrm{HM}}^{\kappa g}$: `HMCode` matter power spectrum; $C_{\ell,\mathrm{CLEFT}}^{\kappa g}$: higher-order terms; $C_\ell^{\kappa\mu}$: magnification bias). As in the case of C_ℓ^{gg}, the signal is dominated by the contribution from the `HMCode` power spectrum and has small but non-negligible contributions from lensing magnification (<1% for Blue and about 6% for Green) and higher-order contributions (up to about 2% for Blue and <1% for Green).

first few principal components. Using a larger number of principal components (capturing 99% of the W^{xc} variance; $n=6$ and 9 for the Blue and Green samples, respectively), we checked that the residual C_ℓ^{gg} variance not captured by the first few principal components is at most ∼10% of the uncertainty on the galaxy power spectrum, while the variance captured by this marginalization is comparable to the 1σ error bars. Nevertheless, we also perform a consistency test by running the full parameter inference pipeline with this larger set of principal components and find no significant shift in the mean cosmological parameters. The uncertainty on $S_8^\times$ is inflated by 2% and 14% when analyzing the Blue and Green samples,

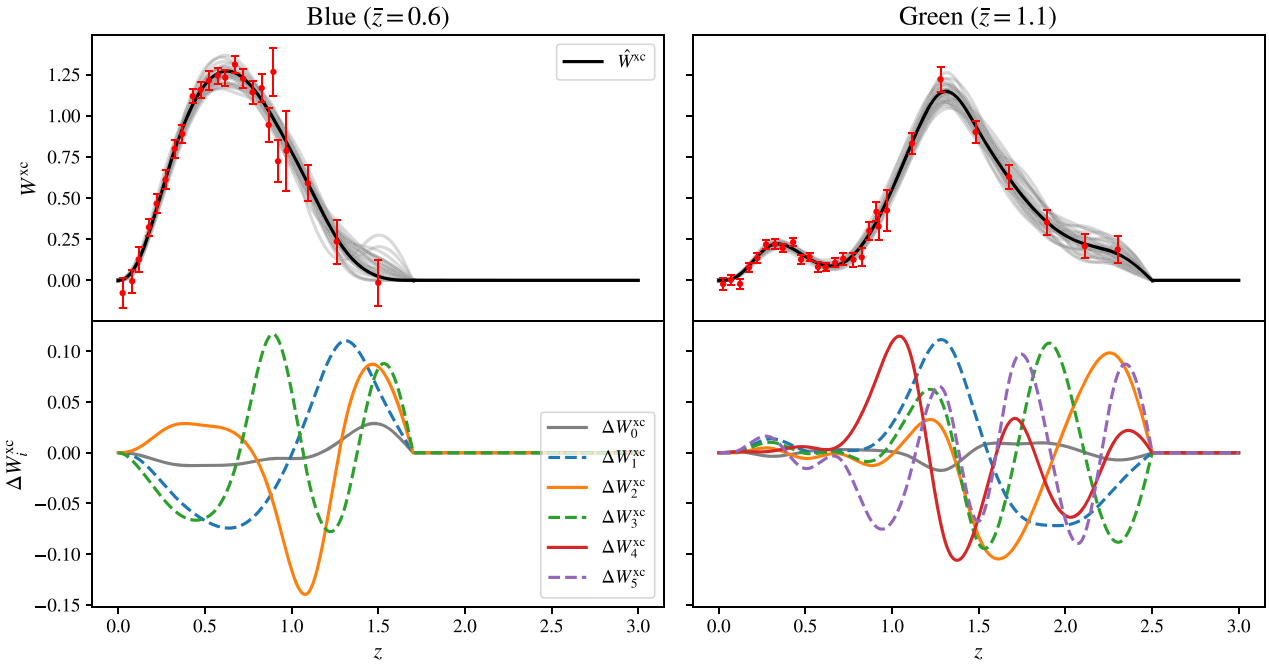

Figure 17. To propagate uncertainties in the measurement of the cross-correlation redshifts to our cosmological analysis, we draw 1000 Gaussian realizations of W^{xc} in a manner consistent with the noise covariance (the best-fitting $\hat{W}^{xc}$ and a subset of the noisy realizations are reproduced here from Figure 3 to facilitate comparison with the PCA noise components). We then perform a PCA analysis on the difference between the realizations and the best fit. The lower panel shows the principal components ($i = 1,...,4$) along with the mean difference between the best-fitting $\hat{W}^{xc}$ and the noise realizations ($i = 0$). In our cosmological analysis, we marginalize over the principal component coefficients.

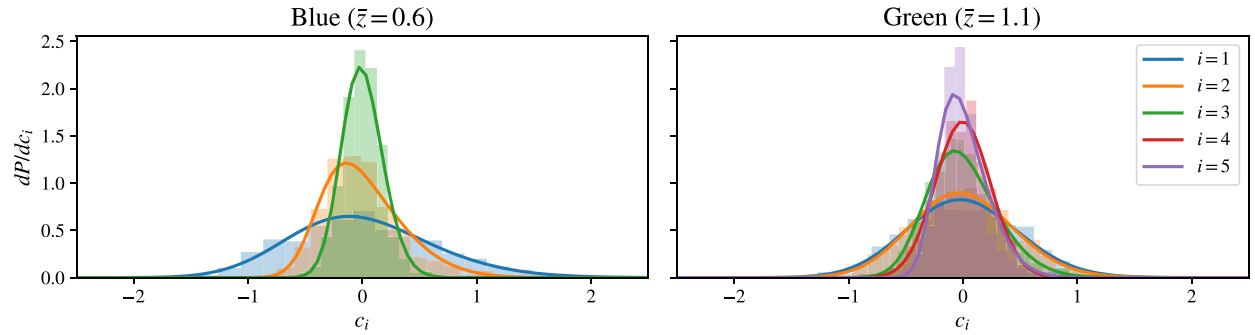

Figure 18. We obtain priors on the principal component coefficients, c_i, by transforming the 1000 realizations of W^{xc} into the basis of principal components and fit the distribution of coefficients observed using skew-normal distributions.

respectively, and remains the same within the convergence limits of our chains when combining both samples (see also Section 9.7).

The uncertainty on our measurement of the clustering redshifts is then expressed in terms of priors on the c_i. We transform the 1000 realizations above into the basis of principal components and fit the distribution of coefficients observed using skew-normal distributions (shown in Figure 18), which we use as priors on each c_i in our analysis.

We note that the marginalization over the uncertainties in the redshift distribution measurements introduces a noise bias in our model prediction. This is because we enforce a positivity constraint on the spline interpolation of the cross-correlation redshift estimates. Additionally, C_ℓ^{gg} depends on the square of $W^{xc}(z)$, and so the final spectra are a nonlinear function of this noisy quantity. The resulting noise bias can be as large as 5% for some of the components contributing to C_ℓ^{gg}. Our method for mitigating this bias is discussed in Appendix C.2.

8.3. Testing the Model on Mocks

For model verification we adopt the CrowCanyon simulations discussed in Krolewski et al. (2021). These simulations are generated using the FastPM code (Feng et al. 2016) using 8192^3 equal mass particles in a $4096h^{-1}$ Mpc a side cubic volume with periodic boundary conditions. The resulting mass resolution is $1.1 \times 10^{10} h^{-1} M_\odot$. The simulation uses a fiducial cosmology close to the mean cosmology found in Planck Collaboration et al. (2020a) with $\Omega_m = 0.3092$, $\Omega_b = 0.0496$, $h = 0.677$, $n_s = 0.968$, and $\sigma_8 = 0.822$.

The lensing convergence and magnification fields are computed by integrating the matter density on the light cone and weighting by the appropriate kernels (for details, see Krolewski et al. 2021). We note that since no lensing reconstruction is performed, the lensing observable does not include any reconstruction noise. To obtain realistic galaxy samples, an HOD tuned to reproduce the unWISE samples is applied to the halos identified in the CrowCanyon simulation. This HOD is available as part of the

Table 1
Analysis of Synthetic Galaxy Clustering and Galaxy-lensing Cross-correlation Observations from *N*-body Simulations[1]

	Ω_m	$\Delta\Omega_m/\sigma_{\Omega_m}$	σ_8	$\Delta\sigma_8/\sigma_{\sigma 8}$	S_8	$\Delta S_8/\sigma_{S_8}$	$S_8^\times$	$\Delta S_8^\times/\sigma_{S_8^\times}$
Simulation input value	0.3092	⋯	0.8222	⋯	0.8347	⋯	0.8335	⋯
				Simulation errors				
Blue	$0.319^{+0.034}_{-0.043}$	0.19	0.825 ± 0.043	0.05	$0.8466^{+0.0091}_{-0.021}$	0.60	$0.8443^{+0.0076}_{-0.018}$	0.67
Green	$0.304^{+0.016}_{-0.018}$	−0.31	0.830 ± 0.018	0.40	$0.8350^{+0.0095}_{-0.013}$	−0.05	$0.8344^{+0.0080}_{-0.012}$	0.01
Joint	$0.306^{+0.013}_{-0.015}$	−0.26	0.829 ± 0.016	0.39	$0.8360^{+0.0068}_{-0.0089}$	0.10	$0.8353^{+0.0059}_{-0.0078}$	0.20
				ACT DR6 × unWISE-like errors				
Blue	$0.335^{+0.053}_{-0.100}$	0.18	$0.819^{+0.083}_{-0.098}$	−0.07	$0.848^{+0.026}_{-0.041}$	0.28	$0.844^{+0.024}_{-0.036}$	0.26
Green	$0.318^{+0.035}_{-0.043}$	0.18	$0.817^{+0.043}_{-0.048}$	−0.14	0.837 ± 0.025	0.07	0.835 ± 0.023	0.05
Joint	$0.318^{+0.033}_{-0.041}$	0.19	$0.816^{+0.042}_{-0.047}$	−0.16	0.836 ± 0.020	0.08	0.834 ± 0.019	0.03

Note. With the smaller theory covariance appropriate for the (somewhat larger) volume of the simulations, we still recover the input cosmology to within about 0.6σ in terms of the now substantially tighter constraints.

[1] When analyzing synthetic galaxy clustering and galaxy-lensing cross-correlation observations from N-body simulations, the Input cosmology is recovered to within better than 0.3σ when adopting the appropriate data covariance for our ACT DR6 cross-correlation analysis.

SIMPLEHOD package.[64] Finally, C_ℓ^{gg} and $C_\ell^{\kappa g}$ are measured from these simulations on the full sky; they hence differ from data in that no mask has been applied, and consequently, no mode coupling is introduced.

The total simulated volume is $\sim 69 h^{-3}\,\mathrm{Gpc}^3$ and thus not overwhelmingly larger than the volume probed by the data (approximately by a factor of 4). Since we restrict ourselves to relatively large scales in our analysis, we expect some fluctuations, due to cosmic variance and sample variance. Therefore, we consider our model unbiased if we are able to recover the input cosmology to within 0.5σ when using the covariance appropriate for our observations with real data. We also perform a test in which we adopt a theory covariance appropriate for the simulation volume, which additionally neglects the lensing reconstruction noise as this is not present in the mocks. For this test, we still recover the input cosmology to within 0.7σ across all cosmological parameters (see Table 1).

Krolewski et al. (2021) measured $b(z)dN/dz$ for these mock samples and found a good match to the observed clustering redshift estimates. Random realizations of $W^{\rm xc}(z)$ were generated in a similar way as for the data assuming the same noise covariance found for the data.

We find that modeling biases on all cosmological parameters considered in our analysis are well under control, not exceeding 0.3σ in all cases (see Table 1). This is a slight improvement over the $\sim 0.5\sigma$ modeling biases in Krolewski et al. (2021).

To establish that an alternative, much simpler choice of model, would not suffice to model the data, we analyze the *N*-body simulations described above with alternative models. We consider two such simpler models: using only the matter power spectrum from `HMCode` or adopting a fixed fiducial evolution of higher-order bias parameters without a free offset (as in Krolewski et al. 2021). For this test, we adopt the covariance appropriate for the simulation volume to perform a maximally stringent test of the input parameter recovery. We find that both models are significantly biased, exhibiting shifts much larger than the expected $\sim 1\sigma$. An `HMCode`-only model underpredicts S_8 by $\sim 2.2\sigma$, while the model from Krolewski et al. (2021) yields a value for S_8that is about 4σ larger than the true value in the simulations. The shifts are less significant when considering a realistic data covariance ($\sim 0.3\sigma$ for the `HMCode`-only model and $\sim 1.2\sigma$ for the model with fixed higher-order biases), but because the value of the true higher-order biases is unknown and could induce larger biases in our data analysis, we adopt the more conservative model.

[64] https://github.com/bccp/simplehod/blob/master/scripts/wlen.py

9. Cosmological Analysis

9.1. Blinding Policy

In the process of preparing the analysis presented in this paper, constraints on cosmological parameters were blinded until we could demonstrate passing a sequence of tests detailed below. We were, however, not blind to the measured spectra, which, at least in the case of C_ℓ^{gg} had already been presented in previous work (Krolewski et al. 2020). Our process toward unblinding cosmological constraints involved the following steps:

1. We tested parameter recovery with our model on *N*-body simulations, as discussed in Section 8.3. Since the volume of these simulations is comparable to that of the observations, deviations from the input cosmology are expected. Hence, we consider our model to be unbiased if we are able to recover the input cosmology to within 0.5σ when using the covariance appropriate for our observations.
2. To verify that our data are not contaminated by foregrounds, including Galactic and extragalactic foregrounds, we run a series of tests described in Section 7. We do not perform such extensive testing for the galaxy–galaxy autospectrum since these have been presented in previous work (Krolewski et al. 2020, 2021). However, since we added systematics weighting for this work, we performed a smaller number of tests to reverify the stability of the galaxy–galaxy autospectrum to different mask choices.

   We qualify a test to be passing if it yields a PTE greater than 0.05. We are satisfied that our mitigation strategies are sufficient if the number of failures (PTE < 0.05) is approximately consistent with what would be expected from random fluctuations when accounting for the correlations between different tests.[65]
3. As a final test, we investigate the consistency of parameters recovered with different analysis choices,

[65] We chose not to consider tests yielding PTE > 0.95 as failures, to minimize the potential for spurious failures, and to focus our null tests on systematic contamination of the data in contrast to a mismodeling of the covariance matrix. Furthermore, the lensing noise modeling has already been tested in detail in Qu et al. (2024). We also note, after the fact, that we do not observe any PTE > 0.95.

including different sky masks, different lensing reconstruction, and bias mitigation methods, varying choices for the measurement of the cross-correlation redshifts, and for the higher-order bias priors. For this purpose, we run parameter inference on the data, but add random offsets to all cosmological parameters that we explicitly sample in the analysis or vary as a function of other parameters (A_s, Ω_m, $\omega_{\rm cdm}$ H_0, σ_8, and S_8).
4. Before unblinding, we freeze all baseline analysis choices. This includes the range of angular scales used in C_ℓ^{gg} and $C_\ell^{\kappa g}$ and all priors on cosmological as well as nuisance parameters.

9.2. Post-unblinding Changes

A few minor aspects of the analysis were corrected post-unblinding, but the impact of these changes is small, and they are partially offset. Consequently, the inferred value of S_8 for our baseline analysis, including only the galaxy autocorrelation of both redshift samples and the cross-correlations with CMB lensing from ACT, is practically unaffected, changing by -0.1σ from our initial unblinded results ($\Delta S_8 = -0.002$, -0.25%). The post-unblinding changes included a modification to the treatment of mask-induced mode coupling of the shot noise component and a small correction to the transfer function obtained from simulations ($+0.2\sigma$). Additionally, the cross-covariance between the two redshift samples had erroneously been neglected (-0.3σ). Finally, we noticed a bug in the model code, which meant that the evolution of the fiducial bias for $b_{2,L}$ was erroneously adopted for $b_{s,L}$ as well. This correction required redetermining the priors on the higher-order biases from the N-body simulations and reverifying the model. Fortunately, the model remains unbiased, and we infer the same value of S_8 for the joint analysis of the cross-correlations of the Blue and Green samples with ACT with only a 5% increase in uncertainty. More detail on these post-unblinding changes is provided in Appendix L.

9.3. Parameter Inference and Priors

We obtain cosmological constraints by constructing a Gaussian likelihood,

$$-2\ln\mathcal{L} \propto \sum_{bb'} \begin{bmatrix} \Delta\hat{C}_b^{gg}(\boldsymbol{\theta}) \\ \Delta\hat{C}_b^{\kappa g}(\boldsymbol{\theta}) \end{bmatrix} \mathbb{C}^{-1} \begin{bmatrix} \Delta\hat{C}_{b'}^{gg}(\boldsymbol{\theta}) \\ \Delta\hat{C}_{b'}^{\kappa g}(\boldsymbol{\theta}) \end{bmatrix}, \tag{28}$$

where the $\Delta\hat{C}_b^{gg}$ and $\Delta\hat{C}_b^{\kappa g}$ are the residuals between our observed galaxy–galaxy and galaxy-lensing spectra, $\hat{C}_b^{gg}$ and $\hat{C}_b^{\kappa g}$, and the respective band window convolved theory spectra, C_b^{gg} and $C_b^{\kappa g}$. The covariance $\mathbb{C}$ has the form

$$\mathbb{C} = \begin{bmatrix} \mathbb{C}_{bb'}^{gg-gg} & \mathbb{C}_{bb'}^{gg-\kappa g} \\ (\mathbb{C}_{bb'}^{gg-\kappa g})^T & \mathbb{C}_{bb'}^{\kappa g-\kappa g} \end{bmatrix}, \tag{29}$$

where $\mathbb{C}_{bb'}^{gg-gg}$, $\mathbb{C}_{bb'}^{\kappa g-\kappa g}$, and $\mathbb{C}_{bb'}^{gg-\kappa g}$ are the galaxy autospectrum covariance, the galaxy-lensing cross-spectrum covariance, and the cross-covariance between them. These are estimated from simulations as described above in Section 6.

We use the Markov Chain Monte Carlo code `cobaya`[66] (Torrado & Lewis 2021) to infer parameters from our galaxy–galaxy and galaxy-CMB lensing data using the model described in Section 8. We consider chains to be converged if the Gelman–Rubin statistic (Gelman & Rubin 1992; Brooks & Gelman 1998) satisfies $R-1 \leqslant 0.01$.

Our data is insensitive to the optical depth to reionization, and we thus fix it to the best-fit value from Planck, $67\tau = 0.0561$ (Planck Collaboration et al. 2020a). Since we are using low-redshift projected tracers alone, the information from the BAO feature in the power spectrum is largely erased, and thus, our data is primarily sensitive to the total matter density, Ω_m. We, therefore, again choose to fix Ωbh2 to the central value from Planck, Ωbh2 = 0.2242 (Planck Collaboration et al. 2020a), and vary only Ωm. Additionally, our measurement of the lensing amplitude is largely degenerate with the distance to the unWISE redshifts, which is primarily set by the Hubble parameter, h. In keeping with Krolewski et al. (2021), we break this degeneracy by fixing the projected angular size of the sound horizon to the value measured from the CMB by the Planck Collaboration, $\theta_{\rm MC}$. It can be shown that $\theta_{\rm MC}$ is predominantly sensitive to the product $\Omega_m h^3$ (Percival et al. 2002). Hence, we fix this combination to $\Omega_m h^3 = 0.09635$, the mean value obtained by the Planck Collaboration (Planck Collaboration et al. 2020a). It should be noted that this combination is largely independent of the complex physics and possible observational systematics that affect the broadband shape of the CMB. It is determined to be approximately 0.3% by Planck, so any uncertainty on this combination would be subdominant to our measurement uncertainties. Finally, we also fix the tilt of the primordial power spectrum to $n_s = 0.9665$ (Planck Collaboration et al. 2020a) and assume the minimum neutrino mass allowed in the normal hierarchy ($\sum m_\nu = 0.06$ eV). Low-redshift data alone is largely insensitive to the sum of the neutrino masses. We will explore the implications of our data in combination with high-redshift information from the primary CMB for neutrino mass constraints in future work. We explore an alternative set of priors on cosmological parameters adopted from the ACT DR6 lensing power spectrum analysis (Qu et al. 2024) in Appendix G. We show that these alternative priors do not significantly affect any of our conclusions.

Our procedure for setting priors on the higher-order bias parameters, $c_{X,L}$, and the redshift marginalization parameters, $c_{dN/dz{\rm PCA},i}$, are described in detail in Sections 8.1 and 8.2, respectively, and the resulting priors are summarized in Table 2. We note that the priors on the redshift marginalization parameters shown here are the ones adopted for our baseline analysis, which includes both the full spectroscopic data set from BOSS and eBOSS and the appropriate weighting of the unWISE data to determine the cross-correlation redshifts (see Section 3.1.2). For some of our consistency tests, we adopt different subsets of the spectroscopic data or neglect the systematics weighting when measuring the cross-correlation redshifts; in each case, we adopt the priors appropriate for the specific cross-correlation measurement used, which can differ somewhat from the ones shown here. As in Krolewski et al. (2021), we adopt 10% Gaussian priors on the measured lensing magnification bias and Gaussian priors with a standard deviation of 0.2 on the logarithm of the shot noise, $\log_{10} P_{\rm shot}$

[66] https://github.com/CobayaSampler/cobaya

[67] We adopt the results obtained in Planck Collaboration et al. (2020a) by including the TT, TE, and EE spectra for multipoles $\ell \geqslant 30$, the EE spectrum for lower multipoles $2 \leqslant \ell \leqslant 29$ ("lowE" likelihood), and additionally Planck lensing and BAO Planck Collaboration et al. (2020a), see Table 2 therein.

Table 2
Parameters and Priors Used in This Work

Parameter	Prior
Sampled cosmological parameters	
Ω_m	[0.01, 0.95]
$\ln(10^{10}A_s)$	[1.0, 4.0]
Fixed and derived cosmological parameters	
n_s	Fixed (0.9665)
τ	Fixed (0.0561)
$\Omega_m h^3$	Fixed (0.09635)
$\Omega_b h^2$	Fixed (0.02242)
$\sum m_\nu$	Fixed (0.06 eV)
h	Derived ($[\Omega_m h^3/\Omega_m]^{1/3}$)
$\Omega_c h^2$	Derived ($\Omega_m h^2 - \Omega_b h^2 - \sum m_\nu/93.14$ eV)
Galaxy model parameters	
Blue sample ($\bar{z} = 0.6$)	
$b_{1,E}^{\rm Blue}$	[0.5, 3.9]
$\log_{10} P_{\rm shot}^{\rm Blue}$	$\mathcal{N}(-7.05, 0.2)$
$s_\mu^{\rm Blue}$	$\mathcal{N}(0.455, 0.0455)$
$c_{2,L}^{\rm Blue}$	$\mathcal{N}(0.55, 0.55)$
$c_{s,L}^{\rm Blue}$	$\mathcal{N}(0.17, 0.29)$
$c_{dN/dz\ {\rm PCA},1}^{\rm Blue}$	$\mathcal{N}_s(-0.58, 0.86, 1.61)$
$c_{dN/dz\ {\rm PCA},2}^{\rm Blue}$	$\mathcal{N}_s(-0.40, 0.54, 2.94)$
$c_{dN/dz\ {\rm PCA},3}^{\rm Blue}$	$\mathcal{N}_s(-0.14, 0.23, 1.27)$
Green sample ($\bar{z} = 1.1$)	
$b_{1,E}^{\rm Green}$	[0.7, 4.2]
$\log_{10} P_{\rm shot}^{\rm Green}$	$\mathcal{N}(-6.79, 0.2)$
$s_\mu^{\rm Green}$	$\mathcal{N}(0.653, 0.0653)$
$c_{2,L}^{\rm Green}$	$\mathcal{N}(0.42, 0.42)$
$c_{s,L}^{\rm Green}$	$\mathcal{N}(0.22, 0.50)$
$c_{dN/dz\ {\rm PCA},1}^{\rm Green}$	$\mathcal{N}_s(-0.30, 0.57, 0.88)$
$c_{dN/dz\ {\rm PCA},2}^{\rm Green}$	$\mathcal{N}_s(-0.30, 0.54, 0.99)$
$c_{dN/dz\ {\rm PCA},3}^{\rm Green}$	$\mathcal{N}_s(-0.31, 0.44, 1.90)$
$c_{dN/dz\ {\rm PCA},4}^{\rm Green}$	$\mathcal{N}_s(-0.09, 0.26, 0.51)$
$c_{dN/dz\ {\rm PCA},5}^{\rm Green}$	$\mathcal{N}_s(-0.24, 0.33, 2.65)$

Note. $\mathcal{N}(\mu, \sigma)$ indicates a Gaussian prior with mean μ and variance σ^2, while $\mathcal{N}_s(\xi, \omega, \alpha)$ indicates a skew-normal prior with location ξ, scale ω, and shape α. Uniform priors are indicated by square brackets. The priors on the magnification bias parameters are adopted from Krolewski et al. (2020), the procedure for obtaining priors on the free parameters in the higher-order bias evolution is described in Section 8.1.4, and the priors on the redshift marginalization parameters are described in Section 8.2.

(translating to a prior of approximately 60% on the amplitude of the shot noise).

9.4. BAO Likelihoods

Weak lensing measurements depend primarily on the amplitude of matter fluctuations σ_8 and the matter density Ω_m. In order to break the degeneracies of our σ_8 constraint with the latter parameter and allow for more powerful comparisons with other probes (including the primary CMB, optical weak lensing measurements, and constraints from CMB lensing autospectra), we include information on BAOs from the 6dF and SDSS surveys. We adopt the same likelihoods used in Madhavacheril et al. (2024). The data we include measure the BAO signature in the clustering of galaxies with samples spanning redshifts up to $z \simeq 1$, including 6dFGS (Beutler et al. 2011), SDSS DR7 Main Galaxy Sample (Ross et al. 2015), BOSS DR12 LRGs (Alam et al. 2017), and eBOSS DR16 LRGs (Alam et al. 2021). We do not use the higher redshift ELGs (Comparat et al. 2016), Lyα (du Mas des Bourboux et al. 2020), and quasar samples (Alam et al. 2021), though we hope to include these in future analyses. We only include the BAO information from these surveys (which for our purposes, primarily constrains Ω_m) and do not include information on the structure growth in the redshift-space distortion (RSD) component of galaxy clustering. We make this choice so as to isolate information on structure formation purely from the cross-correlation alone.

9.5. Constraints on the Cosmological Parameters from the Cross-correlation of ACT DR6 Lensing and unWISE

Jointly analyzing the autocorrelation of the two samples of unWISE galaxies and the cross-correlation of each with the ACT DR6 lensing reconstruction, we obtain a 2.6% constraint on $S_8 \equiv \sigma_8(\Omega_m/0.3)^{0.5}$ of

$$S_8 = 0.813 \pm 0.021. \tag{30}$$

The best-constrained parameter in our analysis actually differs slightly from S_8 and we empirically determined it to be closer to $S_8^\times \equiv \sigma_8(\Omega_m/0.3)^{0.45}$, which we constrain to 2.3% ($S_8^\times = 0.817 \pm 0.019$). All parameter constraints are summarized in Table 3, with the posteriors on cosmological parameters shown in Figure 19.

We note that when analyzing only a single tomographic sample without additional information to break the degeneracy between σ_8 and Ω_m, these parameters are individually only poorly constrained. While the marginalized one-dimensional posteriors on Ω_m and σ_8 obtained from the Blue and Green samples may visually appear to be in some tension, the two samples are consistent within 1.7σ in the full σ_8–Ω_m parameter space.[68] We discuss the consistency of the two redshift samples in more detail in Appendix E.

We can break the degeneracy between σ_8 and Ω_m through the addition of external information. In particular, we combine our analysis with publicly available BAO likelihoods described in Section 9.4, which primarily constrain the matter density, Ω_m. In combination with BAO, we are able to place competitive constraints on σ_8 alone. With the degeneracy broken, the amplitude of the spectra becomes the dominant source of information on σ_8. We find that the combination of the cross- and autocorrelations of the Blue and Green samples with BAO yields

$$\sigma_8 = 0.813 \pm 0.020. \tag{31}$$

The change in S_8 inferred from the joint analysis of the Blue and Green cross-correlations using the alternative priors from Appendix G is small (0.3% or 0.14σ); we find $S_8 = 0.810 \pm 0.021$, indicating that the choice of alternative priors does not significantly affect our constraining power on S_8. When including BAO, we find $\sigma_8 = 0.813 \pm 0.022$ for this alternative set of priors, showing no shift from the mean value obtained with our baseline analysis, but 10% wider errors.

[68] We used the TENSIOMETER package to estimate the significance (https://github.com/mraveri/tensiometer).

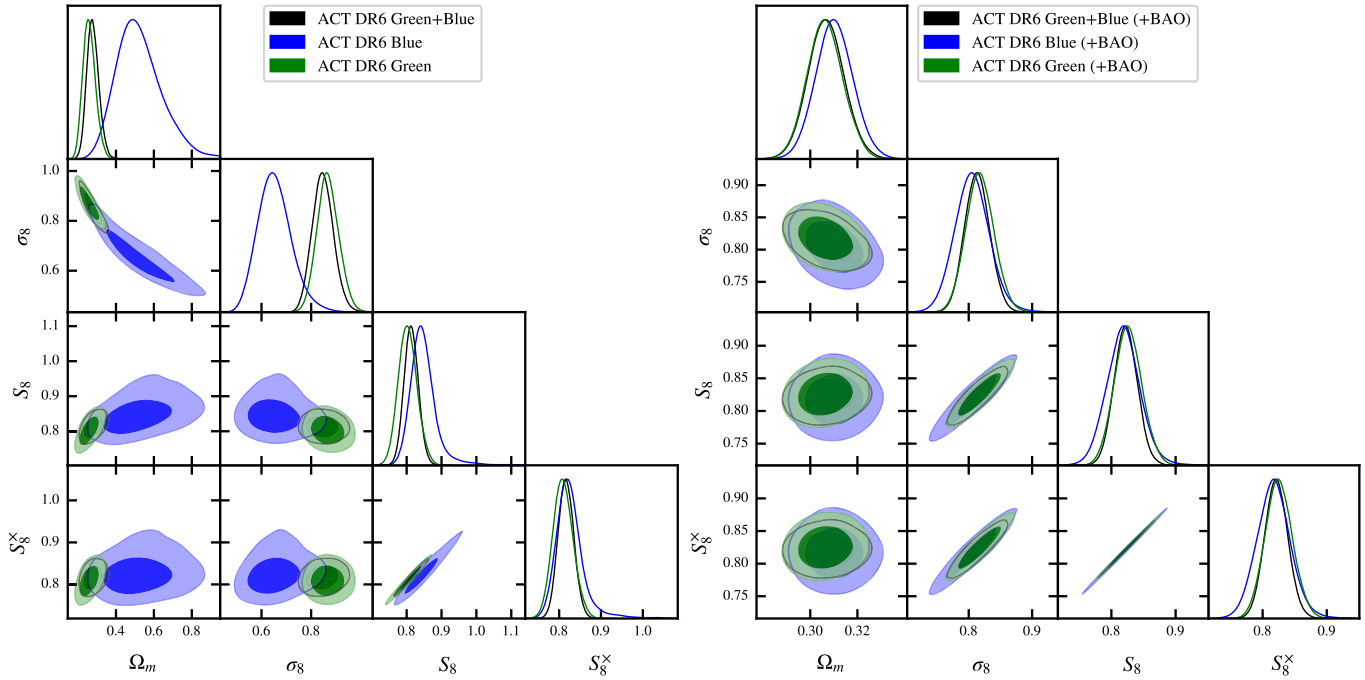

Figure 19. Parameter constraints from the cross-correlation of ACT DR6 lensing and unWISE galaxies. From the combination of C_ℓ^{gg} and $C_\ell^{\kappa g}$ only for both samples of unWISE galaxies (left), we find $S_8 = 0.813 \pm 0.021$. As described in the text, the Blue and Green samples are consistent to within 1.7σ. With additional information on Ω_m from BAO (right), the degeneracy between Ω_m and σ_8 is broken, and we place competitive constraints on $\sigma_8 = 0.813 \pm 0.020$.

Table 3
Summary of the Constraints on Cosmological Parameters Obtained from the Cross-correlation of unWISE Galaxies with ACT DR6 Lensing Reconstruction

	Ω_m		σ_8		S_8		$S_8^\times$	
				ACT DR6 × unWISE only				
Blue	$0.523^{+0.093}_{-0.14}$	(0.476)	$0.654^{+0.058}_{-0.074}$	(0.659)	$0.849^{+0.024}_{-0.040}$	(0.831)	$0.827^{+0.021}_{-0.035}$	(0.812)
Green	$0.259^{+0.029}_{-0.037}$	(0.245)	$0.868^{+0.041}_{-0.046}$	(0.878)	$0.803^{+0.025}_{-0.028}$	(0.793)	$0.809^{+0.022}_{-0.025}$	(0.801)
Joint	$0.279^{+0.028}_{-0.035}$	(0.276)	$0.843^{+0.038}_{-0.044}$	(0.848)	0.813 ± 0.021	(0.813)	0.817 ± 0.019	(0.816)
				ACT DR6 × unWISE + BAO				
Blue	0.3102 ± 0.0079	(0.310)	0.806 ± 0.028	(0.808)	0.819 ± 0.027	(0.821)	0.818 ± 0.027	(0.820)
Green	0.3063 ± 0.0076	(0.306)	0.818 ± 0.022	(0.816)	0.826 ± 0.022	(0.824)	0.825 ± 0.021	(0.823)
Joint	0.3068 ± 0.0077	(0.306)	0.813 ± 0.020	(0.811)	0.822 ± 0.018	(0.819)	0.822 ± 0.018	(0.818)
				ACT DR6 × unWISE + Planck PR4 × unWISE				
Blue	$0.440^{+0.056}_{-0.082}$	(0.424)	0.692 ± 0.051	(0.690)	0.830 ± 0.021	(0.820)	0.815 ± 0.019	(0.806)
Green	$0.263^{+0.020}_{-0.023}$	(0.275)	0.861 ± 0.029	(0.857)	0.804 ± 0.019	(0.793)	0.809 ± 0.017	(0.799)
Joint	$0.274^{+0.019}_{-0.022}$	(0.264)	0.849 ± 0.029	(0.860)	0.810 ± 0.015	(0.808)	0.814 ± 0.014	(0.813)
				ACT DR6 × unWISE + Planck PR4 × unWISE + BAO				
Blue	0.3109 ± 0.0079	(0.309)	0.801 ± 0.021	(0.805)	0.816 ± 0.019	(0.817)	0.814 ± 0.019	(0.816)
Green	0.3039 ± 0.0074	(0.303)	0.818 ± 0.017	(0.818)	0.823 ± 0.016	(0.821)	0.823 ± 0.016	(0.821)
Joint	0.3046 ± 0.0074	(0.305)	0.813 ± 0.015	(0.809)	0.819 ± 0.014	(0.815)	0.819 ± 0.014	(0.815)

Note. Best-fit values (MAP) are shown in parentheses following the one-dimensional marginalized constraints. The combination of the galaxy-lensing cross-correlation and the galaxy clustering autospectrum is primarily sensitive to the parameter S_8. To break the degeneracy between the matter density, Ω_m, and the amplitude of fluctuations, σ_8, we analyze our data jointly with BAO. We also present constraints from the joint analysis of the Planck and ACT cross-correlations.

9.6. Combination with the Cross-correlation of Planck Lensing and unWISE

In Appendix I, we present a reanalysis of the cross-correlation between Planck CMB lensing and the two unWISE galaxy samples studied in this work using our improved model dN/dz and systematics weights, implementing the previously neglected Monte Carlo lensing norm correction, and updating to Planck PR4. We find

$$S_8 = 0.805 \pm 0.018 \quad (32)$$

from the cross-correlation alone and

$$\sigma_8 = 0.810 \pm 0.018 \quad (33)$$

when combined with BAO. Despite the significant improvement in lensing noise for ACT, these results from the cross-correlation with Planck constrain S_8 and σ_8 more tightly than the results presented in Section 9.5. This is due to the significantly smaller sky area in ACT (∼60% versus ∼20%). Since the results from ACT and Planck are consistent, we also

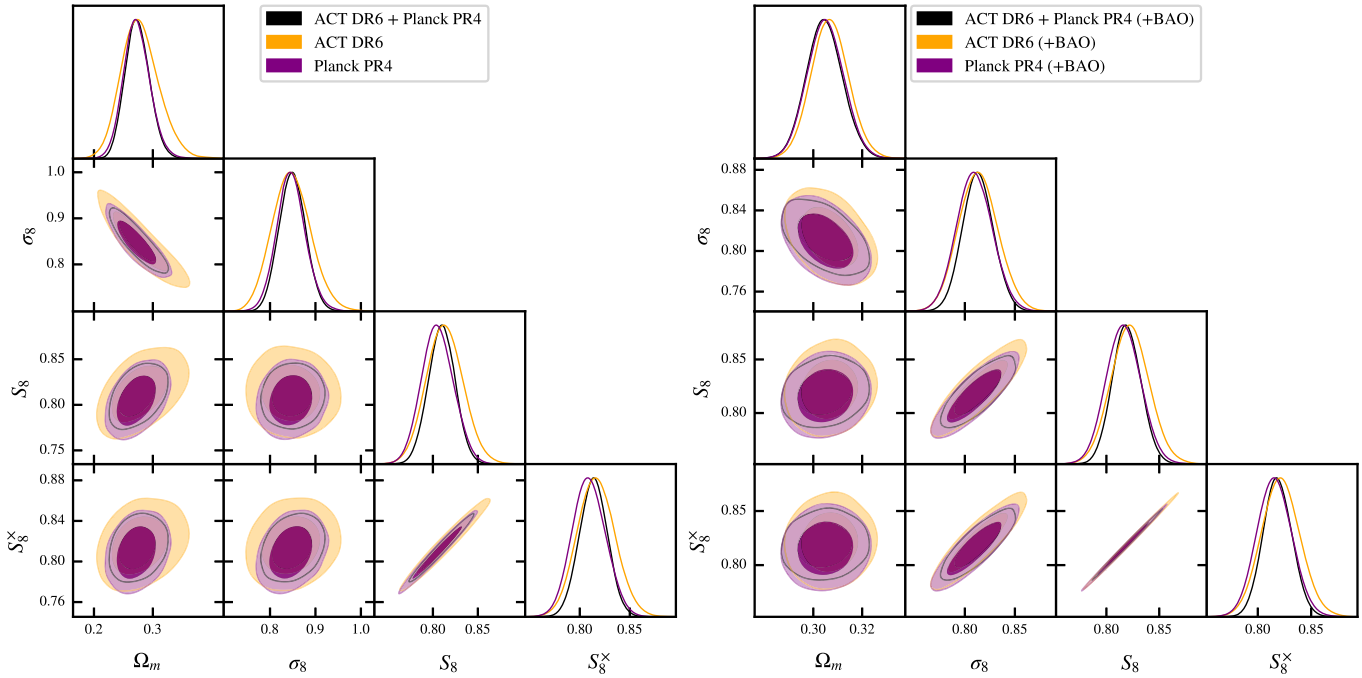

Figure 20. We combine the cross-correlations of unWISE galaxies with lensing reconstructions from ACT DR6 and Planck PR4 at the likelihood level to obtain further tightened constraints on cosmological parameters. Here we show a comparison of the joint analysis of both redshift samples from ACT only, Planck only, and the combination of ACT and Planck. As above, the left panel shows constraints using C_ℓ^{gg} and $C_\ell^{\kappa g}$ only, for which we find $S_8 = 0.810 \pm 0.015$. Including BAO information (right) yields $\sigma_8 = 0.813 \pm 0.015$.

present a joint analysis of the cross-correlation of unWISE galaxies with ACT DR6 and Planck PR4 lensing.

In Section 6, we described how we estimate the cross-covariance between the ACT and Planck cross-correlations. We established in Section 7.2 that the galaxy nuisance parameters, principally the linear galaxy bias, are expected to vary across the sky. Hence, we do not assume these to be identical in the ACT and Planck footprints. We, therefore, include C_ℓ^{gg} measured with both the ACT and Planck masks in our analysis and independently marginalize over the nuisance parameters for both sets of observations. We include the significant cross-covariance between $C_\ell^{gg,\mathrm{ACT}}$ and $C_\ell^{gg,\mathrm{Planck}}$, which is also estimated from our Gaussian simulations and correctly captures the overlap in the area of both observations.

The combination of ACT DR6 and Planck PR4 cross-correlations with unWISE yields a joint constraint

$$S_8 = 0.810 \pm 0.015, \tag{34}$$

a 29% and 17% improvement over the constraints from ACT DR6 and Planck PR4 alone, respectively. In combination with BAO we find

$$\sigma_8 = 0.813 \pm 0.015, \tag{35}$$

again improving the individual constraints from ACT(+BAO) and Planck(+BAO) by 25% and 17%, respectively. The joint constraints are shown alongside the constraints from ACT and Planck alone in Figure 20.

9.7. Parameter-based Consistency Test

As discussed in Section 9.1, we performed a series of parameter-level consistency tests on the ACT data by running our full analysis pipeline using different lensing reconstruction methods and data subsets. These tests were originally performed blindly by consistently adding random offsets to the cosmological parameters. Here we present the unblinded versions of these tests. The alternative analyses using simplified models, discussed toward the end of this section, were not performed prior to unblinding. Figure 21 illustrates a summary of the results of these tests.

We compare the following data subsets to our baseline analysis: (1) cross-correlations measured using the temperature-only lensing reconstruction, (2) an analysis restricted to ecliptic latitudes greater than 30° (additionally, 2b) also restricting the cross-correlation redshift estimation to this region), (3) an analysis using a more restrictive Galactic mask, which includes only the 40% of the sky with the lowest Galactic contamination, (4) two analyses further restricting the range of scales used in our analysis, once by increasing ℓ_{min} to 150 and 100 for C_ℓ^{gg} and $C_\ell^{\kappa g}$, respectively, and once by reducing ℓ_{max} to 300 for both C_ℓ^{gg} and $C_\ell^{\kappa g}$, (5) an analysis using two times wider priors on the higher-order bias parameters, (6) an analysis using a more restrictive scale cut for the cross-correlation redshift estimation (minimum scale of 4 h^{-1} Mpc rather than 2.5 h^{-1} Mpc), and (7) an analysis using more principal components for redshift marginalization (capturing 99% of the variance in the bias-weighted redshifts; $n = 6$ and 9 for the Blue and Green samples, respectively).

Furthermore, we compare our results to the constraints obtained using a different set of priors adopted from the analysis in Qu et al. (2024), as discussed above and in Appendix G. Finally, we also produce a comparison between measurements conducted exclusively on the NGC and SGC regions. These are fully independent as they also rely on measuring the cross-correlation redshifts on the respective regions.

We estimate the statistical likelihood of observing the shifts obtained by considering the shift in the best-constrained parameter $S_8^\times$, effectively assuming that we are only measuring

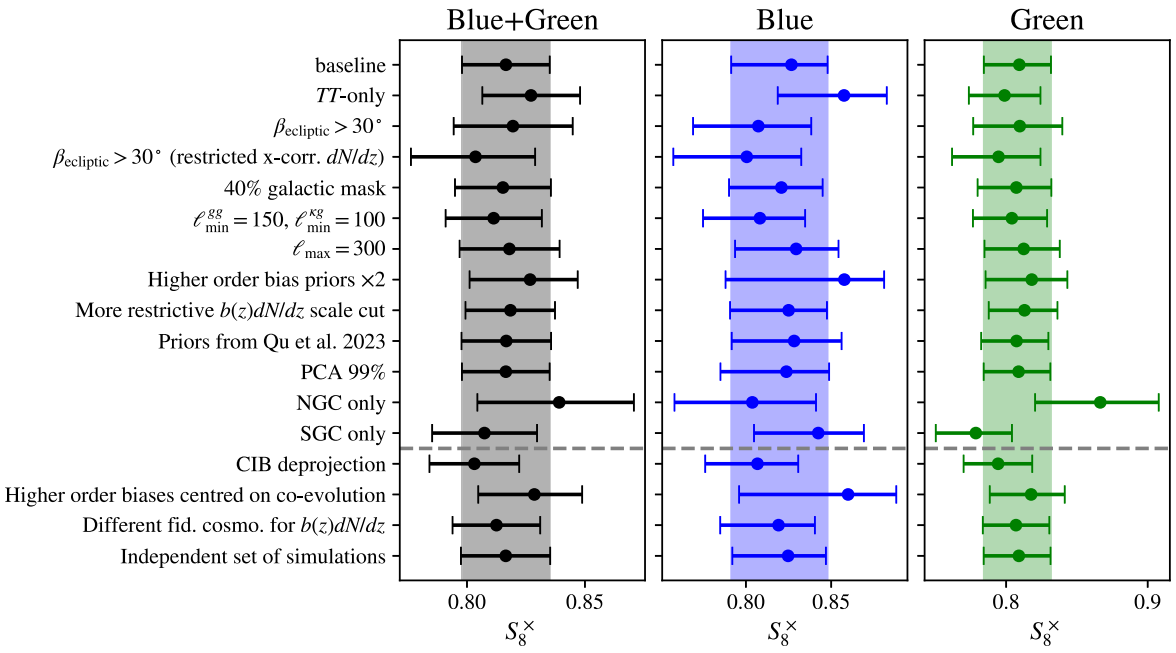

Figure 21. We tested various analyses of data subsets and alternative choices for higher-order bias parameters and hyperparameters relating to the measurement of the cross-correlation redshifts. Here we show the impact on the best-constrained parameter, $S_8^\times$, of these alternative analysis choices. We note that these results are not independent, and where possible, we estimate the likelihood of the shifts observed in Table 6. More consistency tests are also summarized in Table 7. We find consistency across all our tests, indicating that our results are unlikely to be significantly affected by residual systematic contamination.

a single parameter related to the amplitude of the spectrum. For the comparison of nested data sets, i.e., such data sets where one is a proper subset of the other, we estimate the statistical uncertainty on the expected shift in parameters as the difference between the marginalized posterior width of each of the samples approximating them as Gaussian (Gratton & Challinor 2020). In the case where both data sets are independent, we add the variance of both measurements. Detailed results of all consistency tests are provided in Table 6 in Appendix F.

For the other parameters of interest (in particular σ_8 and Ω_m), such comparisons are less straightforward, as these parameters are individually only poorly constrained by the cross-correlations alone, and the posteriors are far from Gaussian. However, we find that the parameter means fall within the 68% confidence region of our baseline analysis in all but three cases for which such shifts are not unexpected, due to a significant reduction in data volume (when restricting the ecliptic latitude to be greater than 30° for the Blue sample and when considering only the NGC for the Blue or Green sample). We show the constraints on σ_8 and Ω_m from the various subset analyses in Figures 37 and 38 in Appendix F.

We also conduct three variations of our baseline analysis that do not simply consider subsets of the full data set (also shown in Figure 21). First, we adopt a lensing reconstruction in which the contamination from CIB has explicitly been deprojected using high-frequency data from Planck. Second, we center the higher-order bias parameters on the fiducial coevolution relations rather than the best fit from simulations. Finally, we use a slightly different fiducial cosmology to measure the cross-correlation redshifts, with $h = 0.702$, $\Omega_m = 0.278$, and $\sigma_8 = 0.805$. For these tests, an estimate of the significance of the shifts observed cannot be obtained easily, due to the nontrivial covariance between these measurements and our baseline analysis. However, the shifts in the parameters S_8 and $S_8^\times$ are small compared to our measurement uncertainties ($<0.35\sigma$; see Table 7 in Appendix F). As discussed in Section 6, we also conduct a stability test using an independent set of simulations to estimate our covariance. This test is also shown in Figure 21. We find that our results are unchanged with this independent covariance estimate.

All consistency tests pass, and the shifts in the parameters of interest are small compared to our uncertainties. This indicates that our baseline cosmology results are unlikely to be significantly affected by remaining systematic contamination.

We note that the null test failures discussed in Section 7.1 indicate a slightly larger lensing amplitude preferred by the temperature-only data. We showed that the difference is consistent with random fluctuations. Nevertheless, we assessed the impact on cosmological parameters. Using the temperature-only lensing reconstruction leads to an increase in the inferred S_8 compared to our baseline analysis of $\Delta S_8 = 0.014$ ($+0.7\sigma$; see Table 6). The shift is consistent within the expected error on the difference between the baseline and temperature-only analysis, and increases the discrepancy with S_8 inferred from galaxy surveys (see comparisons in Section 10.2).

In Figure 22, we also show the impact of neglecting some of the model components in our analysis and find this to have a small impact on the inferred values of $S_8^\times$ ($<1\sigma$ in terms of our statistical uncertainties; these analyses are also summarized in Table 7). While analyses with these models do not appear strongly biased, they also do not dramatically improve our constraining power.

Finally, we compare model predictions for the cross-correlation between the two galaxy samples with the observed $C_\ell^{g_{\rm Blue} g_{\rm Green}}$. We find that the model prediction, fit only to the two galaxy autospectra and the cross-correlations with the ACT DR6 lensing reconstruction, is consistent with the observed cross-spectrum within the expected uncertainty (see Appendix H for details).

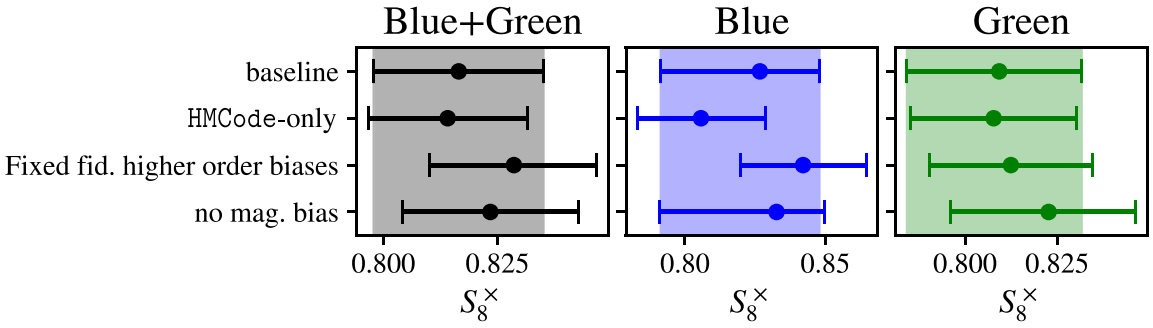

Figure 22. The impact of neglecting various components of our model is very small, with all resulting shifts well below 1σ in terms of our statistical uncertainty. This indicates that our results will only have a small dependence on the detailed modeling choices for those model components.

10. Discussion and Conclusions

Measuring the amplitude of low-redshift fluctuations can reveal the nature of dark matter and dark energy, measure the masses of neutrinos, and provide crucial tests of gravity. The cross-correlation of CMB lensing maps with matter tracers (such as galaxies in this work) with a known redshift distribution—or CMB lensing tomography—can isolate the redshifts of interest, study the time dependence of the signal, break the degeneracy with galaxy bias and reduce the sensitivity to several sources of systematics. In this paper, we leveraged the low shot noise and large redshift lever arm of the unWISE Blue and Green galaxy samples, which fully cover the dark energy-dominated era as well as the transition to matter domination. Our results improve and build upon a previous analysis in Krolewski et al. (2021), and the main differences are highlighted in Appendix I.

10.1. Comparison with Predictions from the Primary CMB

By combining galaxy clustering and cross-correlation measurements, we find $S_8 = 0.813 \pm 0.021$ using ACT lensing, and $S_8 = 0.810 \pm 0.015$ with a combination of Planck and ACT lensing, consistent with the prediction from the primary CMB from Planck at the 0.8σ and 1.1σ level, respectively (Planck obtains $S_8 = 0.834 \pm 0.016$ or $S_8 = 0.832 \pm 0.013$ with CMB lensing; Planck Collaboration et al. 2020a) and with similar statistical uncertainty. BAO data breaks the degeneracy between σ_8 and Ω_m, and we find $\sigma_8 = 0.813 \pm 0.020$ from ACT alone and $\sigma_8 = 0.813 \pm 0.015$ from the combination of Planck and ACT. Again, this is in very good agreement with the Planck primary CMB results of $\sigma_8 = 0.8120 \pm 0.0073$ (0.05σ and 0.07σ, respectively) using primary CMB only (or $\sigma_8 = 0.8111 \pm 0.0060$ when including CMB lensing; Planck Collaboration et al. 2020a). The comparisons with the Planck results are shown in Figure 23, along with other large-scale structure measurements of S_8 and σ_8. Our results are also consistent with predictions from independent primary CMB observations, including from the combination of the Wilkinson Microwave Anisotropy Probe and ACT (Aiola et al. 2020). We show those constraints in Figures 24 and 25 together with a more comprehensive set of other measurements.

10.2. Comparison with Other Measurements of the Large-scale Structure of the Universe

In addition to the comparison to predictions for the amplitude of the structure formation from the primary CMB (using Planck and ACT), we also compare our results to measurements from other large-scale structure observables. We include results from CMB lensing autospectrum analyses (Bianchini et al. 2020; Carron et al. 2022; Madhavacheril et al. 2024; Qu et al. 2024), galaxy weak lensing surveys (DES, KiDS, and HSC; Heymans et al. 2021; Abbott et al. 2022; Miyatake et al. 2023; More et al. 2023; Sugiyama et al. 2023), from other cross-correlations with CMB lensing from ACT, SPT, and Planck (Chen et al. 2022b; White et al. 2022; Abbott et al. 2023b; Chang et al. 2023; Marques et al. 2024), and from the three-dimensional clustering of galaxies (Alam et al. 2021; Ivanov et al. 2023). We subsequently briefly introduce the data sets we employ:

1. *CMBL*: These are constraints from the analysis of the autospectrum of CMB lensing reconstructions. These results are mostly sensitive to linear scales at $z = 1$–2 and primarily constrain the parameter combination $\sigma_8\Omega_m^{0.25}$. We include results from Planck PR4 (Carron et al. 2022), SPTpol (Bianchini et al. 2020), ACT DR6, and a joint analysis of ACT DR6 and Planck PR4 (Madhavacheril et al. 2024). To make fair comparisons, we combine the CMB lensing measurements with BAO information, which breaks the degeneracy between σ_8 and Ω_m.
2. *WL*: From galaxy weak lensing surveys, we include constraints from "3x2pt" analyses, combining measurements of galaxy clustering, galaxy shear, and their cross-correlation. For DES we adopt the results obtained in Abbott et al. (2022) when fixing the neutrino mass. For KiDS, we show results presented in Heymans et al. (2021). We note, that in contrast to the DES analysis, these results are obtained from the combination of projected galaxy shear and galaxy–galaxy lensing measurements with a measurement of the three-dimensional clustering of galaxies in the spectroscopic BOSS and 2dfLenS surveys. Therefore, the KiDS analysis already contains the BAO information. For HSC, we adopt a set of results from a reanalysis of the HSC galaxy shear, galaxy–galaxy lensing, and galaxy clustering measurements (More et al. 2023) using priors on cosmological parameters consistent with those used in this work (see Table 2). We show the results from an analysis using a linear bias model (Sugiyama et al. 2023) and from an analysis using a halo model-based emulator, which includes nonlinear scales (Miyatake et al. 2023).
3. *CMBLX*: We compare our results with other cross-correlations between CMB lensing and galaxy surveys. White et al. (2022) analyzed the cross-correlation between DESI LRG targets and a lensing reconstruction from Planck PR3 (Planck Collaboration et al. 2020b). We also include a series of works cross-correlating DES-Y3

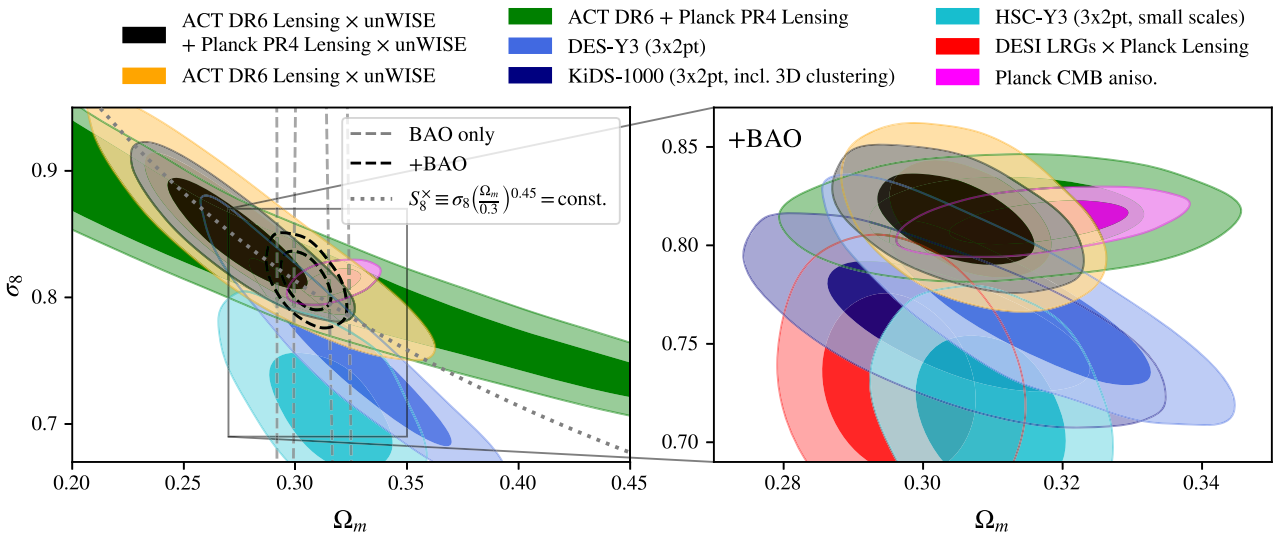

Figure 23. Here we show constraints in the Ω_m–σ_8 plane for our baseline results and selected other data sets. The left panel shows results without external information on Ω_m; all large-scale structure probes show a significant degeneracy between Ω_m and σ_8. For our analysis, the best constraint parameter combination is proportional to $\sigma_8\Omega_m^{0.45}$ shown here as a dotted line. This degeneracy is broken by the addition of BAO information. To illustrate the effect of BAO information, we show the BAO-only constraint as a dashed gray contour and the joint cross-correlation analysis of ACT and Planck with BAO as a dashed black contour (in the left panel). The right panel shows a comparison with other data sets when adding BAO information. We note that given that we do not reanalyze these other data sets, they do not all use the same BAO likelihoods as in this work. We can see that our analysis is in no significant tension with any of the other data sets shown when considering the full Ω_m–σ_8 parameter space despite favoring a larger value of S_8 and σ_8 compared to galaxy weak lensing surveys. Our results are consistent with predictions from the primary CMB and CMB lensing.

galaxy shear and galaxy clustering ($\delta_g + \gamma$) with a joint SPT and Planck lensing reconstruction (Chang et al. 2023). Building on this work, Abbott et al. (2023b) present a "5x2pt" and "6x2pt" analysis, combining all DES-internal cross- and autocorrelations and additionally the lensing autospectrum, respectively. The joint lensing reconstruction from SPT-SZ and Planck is presented in Omori et al. (2023). A recent cross-correlation between DES-Y3 clustering (δ_g) and ACT DR4 lensing (Marques et al. 2024) based on the lensing reconstruction from Darwish et al. (2021) is also included. While all aforementioned analyses use photometric galaxy samples in their cross-correlations, the final cross-correlation study included in our comparisons, Chen et al. (2022b), jointly models the three-dimensional clustering of the spectroscopic BOSS galaxies and their cross-correlation with Planck.

4. *GC*: Finally, we compare our results with constraints from the three-dimensional clustering of galaxies as measured by BOSS and eBOSS. We include the analysis of BAO and RSD from Alam et al. (2021). Furthermore, we include an independent analysis based on the effective theory of large-scale structure (EFTofLSS) that fits the *full shape* of the power spectrum and bispectrum measured in redshift space (Ivanov et al. 2023). Similar, previous analyses found compatible results (see, e.g., D'Amico et al. 2020; Ivanov et al. 2020; Chen et al. 2022a).

In the left panel of Figure 23, we show a comparison of our results with various other probes in the Ω_m–σ_8 parameter space. We can see that the large-scale structure probes shown exhibit a significant degeneracy between σ_8 and Ω_m. That degeneracy is broken when adding BAO information as we show in the right panel of Figure 23. A more extensive set of comparisons for S_8 and σ_8 is shown in Figures 24 and 25, respectively. Generically, we include BAO information in all comparisons of σ_8 to break the Ω_m–σ_8 degeneracy. An exception is those measurements employing three-dimensional galaxy clustering either on its own, as part of a 3x2pt analysis, or in cross-correlation. Those measurements already implicitly contain the BAO information.

We note that we do not reanalyze these data sets with our prior choices. An exception is the results from HSC for which the Markov Chain Monte Carlo runs are not publicly available at the time of writing and which were kindly provided by the HSC team with prior choices that match ours. Madhavacheril et al. (2024) discussed the impact of reanalyzing the galaxy survey data sets with priors matching those in the ACT DR6 lensing autospectrum analysis and found only minor changes (see Appendix C in Madhavacheril et al. 2024). As previously discussed, we also explore an alternative set of priors in Appendix G. We find that while our constraints on S_8 are not very sensitive to the choice of priors, the constraints on σ_8 in combination with BAO are slightly degraded ($\sim$10%) when the Planck prior on $\Omega_m h^3$ is removed. However, we do not observe any significant shifts in the mean σ_8 or S_8, and therefore, we do not expect our conclusions to differ substantially.

Our results are in good agreement with various CMB lensing autospectrum analyses. Given that CMB lensing is primarily sensitive to the parameter combination $\sigma_8\Omega_m^{0.25}$ we combine our measurements as well as the CMB lensing measurements from Planck, SPTpol, and ACT DR6 with BAO to be able to directly compare the resulting σ_8 constraints. The value of σ_8 inferred from the cross-correlation of unWISE with ACT DR6 and Planck together with BAO is consistent within 0.3σ with the constraints from ACT DR6, within 0.04σ with the result from Planck PR4, and within 0.06σ with the results from the joint analysis of ACT DR6 and Planck PR4. In the parameter σ_8, the agreement with SPTpol is less good, though not at any statistical significance (1.2σ).

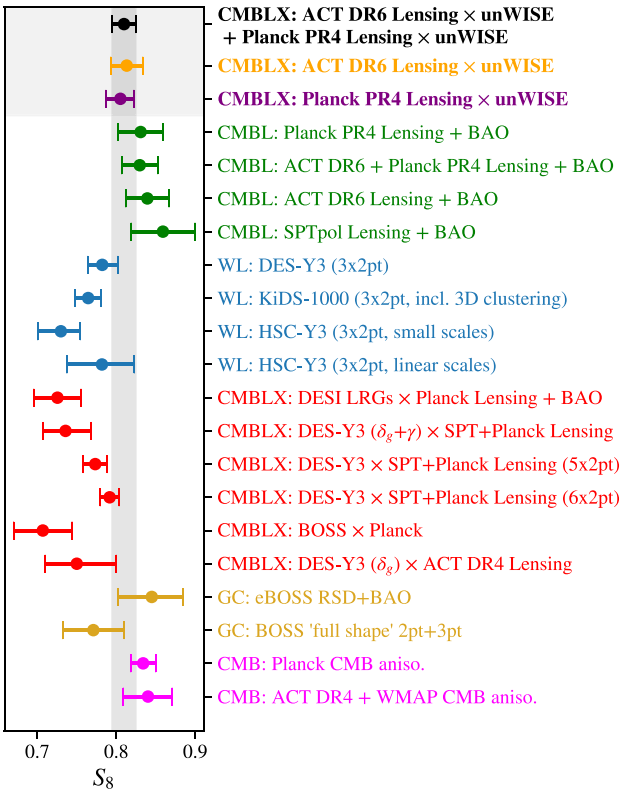

Figure 24. Here we compare with an extensive set of measurements of S_8. We include measurements from CMB lensing analyses in combination with BAO (in green), from galaxy weak lensing surveys (in blue), from cross-correlations with CMB lensing (in red), from the three-dimensional clustering for spectroscopic galaxy surveys (in gold), and predictions from the primary CMB (in magenta). Our results are in good agreement with CMB lensing analyses, as well as with the predictions from the primary CMB. They are also in no significant tension with any galaxy weak lensing survey or the S_8 inferred from the three-dimensional clustering of spectroscopic galaxies. We do, however, find some discrepancies at up to 3σ with previous cross-correlation work.

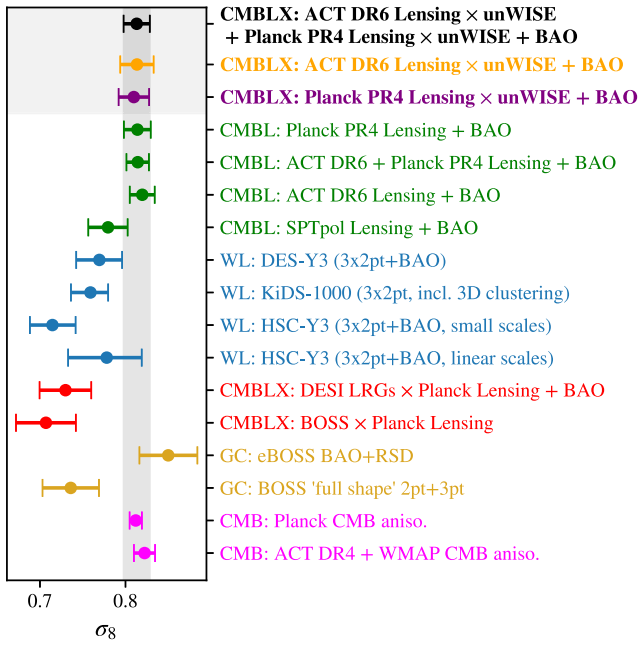

Figure 25. Here we compare with an extensive set of measurements of σ_8. As above, we include measurements from CMB lensing analyses in combination with BAO (in green), from galaxy weak lensing surveys (+BAO; in blue), from cross-correlations with CMB lensing (+BAO; in red), from the three-dimensional clustering for spectroscopic galaxy surveys (in gold), and predictions from the primary CMB (in magenta). As in the case of S_8, our results are in good agreement with most CMB lensing analyses, as well as with the predictions from the primary CMB. Galaxy weak lensing surveys favor smaller σ_8 at varying levels of significance (0.8σ–3.2σ). We also find some discrepancies at up to 3σ with previous cross-correlation work.

These results can also be compared to galaxy weak lensing measurements of S_8. Analyses of DES and KiDS obtain $S_8 = 0.782 \pm 0.019$ and $S_8 = 0.765^{+0.017}_{-0.016}$, respectively, from a combination of cosmic shear and galaxy clustering. The reanalysis of HSC cosmic shear and galaxy clustering with our prior choices yields $S_8 = 0.782 \pm 0.043$ when using only linear scales and $S_8 = 0.730^{+0.025}_{-0.029}$ from an analysis using a halo-model-based emulator.[69] They are all lower than our results, but not in significant statistical tension (approximately 1.1σ, 2.0σ, $0.\sigma$, and 2.5σ for DES, KiDS, and the two results from HSC, respectively). We note that the DES and KiDS 3x2pt analyses draw on cosmic shear measurements for which recent reanalyses have found shifts toward higher S_8. A recent and improved reanalysis of KiDS-1000 cosmic shear data obtains $S_8 = 0.776^{+0.031}_{-0.030}$ (S.-S. Li et al. 2023; increased from the previous $S_8 = 0.759^{+0.024}_{-0.021}$; Asgari et al. 2021), while a recent joint reanalysis of the DES and KiDS cosmic shear data also hints at a higher value of $S_8 = 0.790^{+0.018}_{-0.014}$ (also higher than previous DES results from cosmic shear alone, which yielded $S_8 = 0.759^{+0.025}_{-0.023}$ and the KiDS results above; Amon et al. 2022; Abbott et al. 2023a). For these two renewed cosmic shear analyses, the discrepancy with our results is reduced to $\sim 1.5\sigma$ and $\sim 0.9\sigma$, respectively. It is possible that the shear recalibration from Li et al. (2023) and changes to the pipeline and prior choices in Abbott et al. (2023a) will also increase S_8 inferred from the 3x2pt analyses to which we compare here.

In addition to evaluating the consistency of our cosmological parameters with various weak lensing surveys, we also test the goodness of fit when fixing the cosmology to one similar to the one preferred by DES. This is to test the possibility that our preference for a higher value of S_8 is driven in part by projection effects, which have been seen (albeit in the opposite direction) in some other cross-correlation analyses (Chen et al. 2022b; White et al. 2022). We fixed S_8 to 0.78, close to the mean value obtained by DES (Abbott et al. 2022). We then vary Ω_m and all nuisance parameters in our analysis to obtain the best fit to the autocorrelations of the Blue and Green samples and their cross-correlations with the ACT lensing reconstruction. We find a minimum $\chi^2 = 22.8$. When instead fixing the cosmology to $S_8 = 0.83$, similar to the Planck cosmology, we similarly find $\chi^2 = 23.2$. Our best-fitting baseline model, in which S_8 and Ω_m are free to vary, has a minimum χ^2 of 20.9 but includes one more degree of freedom, suggesting that both the DES and Planck values of S_8 are compatible with our data at $\sim 1\sigma$. However, consistency with the DES cosmology comes at the cost of some tension with the matter density inferred from BAO. When we add BAO

[69] These results differ by approximately 0.2σ and 1.2σ, respectively, from the fiducial results reported by HSC (Miyatake et al. 2023; Sugiyama et al. 2023). The difference is largely driven by the fact that we fix $\Omega_m h^3$ to the mean value for this parameter combination found by Planck. In terms of the expected uncertainty on the difference between the two analyses, the shifts correspond to about 0.3σ–0.6σ and 1.2σ–1.5σ, respectively (assuming that the fiducial analysis constitutes a subset of the analysis with our priors; Gratton & Challinor 2020). These shifts are thus within what is expected, given the difference in prior choices.

information to the minimization at fixed S_8 we find $\Delta\chi^2 = 3.6$ for the DES-like cosmology relative to our baseline fit and $\Delta\chi^2 = 0.3$ for a Planck-like cosmology (including the χ^2 contributions from the BAO likelihoods). This corresponds to a cosmology with the DES-like value of S_8 being slightly disfavored by $\sim 1.6\sigma$.

Our results appear to show a discrepancy with previous CMB lensing cross-correlations. This is true for the previous analysis of the cross-correlation of unWISE and Planck lensing (Krolewski et al. 2021); we discuss this comparison and the origin of the discrepancy in detail in Appendix I. We also find some discrepancies with the results from the cross-correlation of the DESI LRG targets with Planck. White et al. (2022) measured $S_8 = 0.73 \pm 0.03$, corresponding to about a 2.5σ discrepancy with our analysis using both ACT and Planck. A similarly significant difference is also found with the cross-correlation of BOSS and Planck, which yields $S_8 = 0.707 \pm 0.037$ ($\sim 2.6\sigma$), and with the cross-correlation of DES-Y3 with SPT and Planck ($S_8 = 0.736^{+0.032}_{-0.028}$; $\sim 2.2\sigma$). This discrepancy is reduced when adding the DES-internal cross- and autocorrelations. The 5x2pt analysis yields $S_8 = 0.773 \pm 0.016$ ($\sim 1.7\sigma$). Adding the CMB lensing autocorrelation from Planck further increases S_8 to 0.792 ± 0.012 and reduces the discrepancy to $\sim 1.0\sigma$ (6x2pt). Given the consistency of our results with Planck lensing, this is unsurprising. The analysis of DES-Y3 and ACT DR4 lensing also obtains a lower value of S_8, albeit with much larger errors ($S_8 = 0.75^{+0.04}_{-0.05}$; $\sim 1.3\sigma$).

Some of the improvements made here to the previous analysis of the cross-correlation between unWISE and Planck are also relevant for some of the other cross-correlation measurements discussed above. In particular, the inclusion of the Monte Carlo correction to the normalization of the Planck lensing maps (for details, see Appendix I) will also impact the analyses in White et al. (2022), Chen et al. (2022b), Chang et al. (2023), and Abbott et al. (2023b). However, at least in some cases, preliminary results show that they are unlikely to completely alleviate the discrepancy. White et al. (2022) and Chen et al. (2022b) also found indications for significant projection effects in their analyses. We also note the importance of the better redshift calibration of the unWISE samples, which contributed a shift of $\sim 0.8\sigma$ to our reanalysis of the cross-correlation with Planck (see Appendix I), which may also affect other analyses and should be significantly improved in the near future with the availability of spectroscopic redshifts from DESI.

Our results are consistent with the eBOSS analysis of BAO and RSD, which finds $\sigma_8 = 0.850 \pm 0.035$ (consistent with our baseline results within 1.0σ). The full-shape measurements, on the other hand, prefer a lower value of σ_8 by about 2σ.

10.3. Our Results in the Context of the S_8/σ_8 Tension

We briefly discuss the implications of our results for the claimed S_8 tension. It is worth noting that most of the galaxy weak lensing constraints come at least partially from smaller scales, where gravitational nonlinearities, as well as the effects of galaxy formation (assembly bias, baryonic feedback, etc.) are more pronounced. Our cosmological constraints derive almost entirely from perturbative scales at the redshifts of interest ($k \lesssim 0.3\ h\,\mathrm{Mpc}^{-1}$), and therefore, we expect uncertainties, due to galaxy formation to be negligible and fully absorbed in our bias expansion. In Figure 26, we show the scales on which our signal originates. Extensive tests on mocks

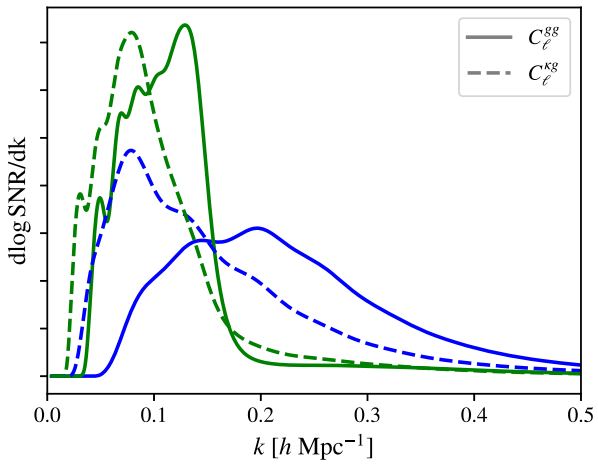

Figure 26. We show the change in the total S/N as a function of the maximum k considered. With our scale cuts ($50 \leqslant \ell \leqslant 400$ for C_ℓ^{kg} and $100 \leqslant \ell \leqslant 400$ for C_ℓ^{gg}), the signal for the galaxy cross- and autocorrelations originates largely on scales of $k \lesssim 0.3\ h\,\mathrm{Mpc}^{-1}$. For the Green sample of galaxies and its cross-correlation with CMB lensing, almost all the signal comes from $k < 0.2\ h\,\mathrm{Mpc}^{-1}$. While the Blue sample has minor contributions from $k \gtrsim 0.3\ h\,\mathrm{Mpc}^{-1}$, almost all the cosmological constraining power comes from larger scales since we marginalize over higher-order contributions to the signal, which become important on smaller scales.

presented in this paper also show no evidence for *projection effects* in the Bayesian parameter estimation. Together with the large number of consistency and null tests, this provides confidence in the results.

The fact that CMB lensing power spectrum measurements (Planck Collaboration et al. 2020b; Carron et al. 2022; Madhavacheril et al. 2024; Qu et al. 2024) are consistent with the CMB power spectrum prediction deriving from high redshifts excludes the possibility of substantial effects of new physics on structure growth at high redshifts and large scales; however, the possibility of new physics at low redshifts ($z \lesssim 1$) or smaller scales remains when considering only CMB lensing power spectrum data. Although the analyses presented in this paper are sensitive to the growth of structure at $z \simeq 0.2$–1.6 (on large scales), our measurements show excellent consistency with CMB power spectrum predictions. In short, using the cross-correlations of CMB lensing and galaxy density, we find no evidence for an S_8 (or σ_8) tension on scales $k \lesssim 0.3\ h\,\mathrm{Mpc}^{-1}$ and for $z \gtrsim 0.2$. Our results, together with CMB lensing autospectrum analyses, imply that if new physics is indeed responsible for the S_8 tension observed in galaxy weak lensing data sets, any effects of new physics must be mostly limited to small scales ($k \gtrsim 0.3\ h\,\mathrm{Mpc}^{-1}$) to which our unWISE measurements are insensitive. This is consistent with resolutions to the S_8 tension based on modifications to the matter power spectrum on nonlinear scales (Amon & Efstathiou 2022; Preston et al. 2023). Our work, therefore, motivates further efforts to test the ΛCDM predictions for structure formation on smaller, nonlinear scales.

10.4. Conclusions

We have presented cosmological results from the cross-correlation of the Blue and Green unWISE galaxy samples and the latest Planck and ACT CMB lensing maps. Thanks to its large footprint on the sky, extended redshift lever arm, and high number density, the unWISE extragalactic samples are ideal for

a number of cross-correlations, including CMB lensing tomographic analyses.

Using conservative choices and a blinded analysis, we were able to obtain a 1.7% and 1.8% measurement of S_8 and σ_8, respectively, when combining the cross-correlations of the Blue and Green unWISE samples with ACT and Planck lensing reconstructions. Both samples and their combination are in full agreement with CMB lensing and the primary CMB results, providing an important test of the standard cosmological model at $z \simeq 0.2$–1.6. Our results imply that if new physics is responsible for the S_8 tension, any effects of new physics must be mostly limited to small scales ($k \gtrsim 0.3\ h\,\mathrm{Mpc}^{-1}$) to which our unWISE measurements are insensitive.

The statistical consistency with CMB lensing autocorrelation results, together with the comprehensive suite of systematic and null tests, motivates deriving joint constraints between the cross-correlation presented here and the CMB lensing autopower spectrum. This analysis will be presented in upcoming work.

Acknowledgments

The authors wish to thank David Alonso, Julien Carron, Benjamin Joachimi, Giulio Fabbian, and Noah Sailer for useful discussions and comments. We are particularly grateful to Hironao Miyatake and the HSC team for making a consistent reanalysis of their Y3 results available to us. We also thank the anonymous reviewer for a very thorough review of this work and the constructive feedback.

Support for ACT was through the U.S. National Science Foundation through awards AST-0408698, AST-0965625, and AST-1440226 for the ACT project, as well as awards PHY-0355328, PHY-0855887, and PHY-1214379. Funding was also provided by Princeton University, the University of Pennsylvania, and a Canada Foundation for Innovation (CFI) award to UBC. The development of multichroic detectors and lenses was supported by NASA grants NNX13AE56G and NNX14AB58G. Detector research at NIST was supported by the NIST Innovations in Measurement Science program. ACT operated in the Parque Astronómico Atacama in northern Chile under the auspices of the Agencia Nacional de Investigación y Desarrollo (ANID). We thank the Republic of Chile for hosting ACT in the northern Atacama, and the local indigenous Licanantay communities whom we follow in observing and learning from the night sky.

Computing was performed using the Princeton Research Computing resources at Princeton University, the Niagara supercomputer at the SciNet HPC Consortium, and the Symmetry cluster at the Perimeter Institute. This research also used resources provided through the STFC DiRAC Cosmos Consortium and hosted at the Cambridge Service for Data Driven Discovery (CSD3). SciNet is funded by the CFI under the auspices of Compute Canada, the Government of Ontario, the Ontario Research Fund-Research Excellence, and the University of Toronto. Research at Perimeter Institute is supported in part by the Government of Canada through the Department of Innovation, Science and Industry Canada and by the Province of Ontario through the Ministry of Colleges and Universities. This research also used resources of the National Energy Research Scientific Computing Center (NERSC), a U.S. Department of Energy Office of Science User Facility located at Lawrence Berkeley National Laboratory, operated under contract No. DE-AC02-05CH11231 using NERSC award HEP-ERCAPmp107.

G.S.F. acknowledges support through the Isaac Newton Studentship and the Helen Stone Scholarship at the University of Cambridge. G.S.F., N.M., I.A.C., F.J.Q., B.D.S. acknowledge support from the European Research Council (ERC) under the European Union's Horizon 2020 research and innovation program (grant agreement No. 851274). B.D.S. further acknowledges support from an STFC Ernest Rutherford Fellowship. I.A.C. also acknowledges support from Fundación Mauricio y Carlota Botton. Z.A. acknowledges support from NSF grant AST-2108126. E.C. acknowledges support from the European Research Council (ERC) under the European Union's Horizon 2020 research and innovation program (grant agreement No. 849169). O.D. acknowledges support from the SNSF Eccellenza Professorial Fellowship (No. 186879). A.J.D. acknowledges support from the Flatiron Institute, which is supported by the Simons Foundation. M.H. acknowledges financial support from the National Research Foundation of South Africa (grant No. 137975). K.M.H. acknowledges support from the NSF under awards 1815887, 2009870, and 2206344, and from NASA under award 80NSSC23K0466. L.P. acknowledges support from the Misrahi and Wilkinson funds. M.M. acknowledges support from NASA grant 21-ATP21-0145. G.A.M. is part of Fermi Research Alliance, LLC under contract No. DE-AC02-07CH11359 with the U.S. Department of Energy, Office of Science, Office of High Energy Physics. M.W. is funded by the U.S. Department of Energy. N.S. acknowledges support from DOE award number DE-SC0020441. C.S. acknowledges support from the Agencia Nacional de Investigación y Desarrollo (ANID) through FONDECYT grant No. 11191125 and BASAL project FB210003.

Software: Some of the results in this paper have been derived using the `healpy` (Zonca et al. 2019) and `HEALPix` (Górski et al. 2005) packages. This research made use of `Astropy`,[70] a community-developed core Python package for Astronomy (Astropy Collaboration et al. 2013, 2018). We also acknowledge the use of the `matplotlib` (Hunter 2007) package and the Python Image Library for producing plots in this paper. Furthermore, we acknowledge the use of the `NumPy` (Harris et al. 2020) and `SciPy` (Virtanen et al. 2020) packages. We use the Boltzmann code `CAMB` (Lewis et al. 1999; Howlett et al. 2012) for calculating theory spectra, and use `GetDist` (Lewis 2019) and `Cobaya` (Torrado & Lewis 2021) for likelihood analysis. We acknowledge the work done by the Simons Observatory Pipeline and Analysis Working Groups in developing the open-source software used in this paper.

Appendix A
Off-diagonal Correlations in the Covariance Matrix

Further to the discussion of the off-diagonal correlations in Section 6, here we show a summary of the level of correlations between different samples and between the cross-correlations using ACT and Planck lensing reconstructions. Figure 27 shows the maximum off-diagonal correlations within our analysis range, which uses band powers in the ranges of $50 \leqslant \ell \leqslant 400$ in $C_\ell^{\kappa g}$ and $100 \leqslant \ell \leqslant 400$ in C_ℓ^{gg}.

[70] https://www.astropy.org/

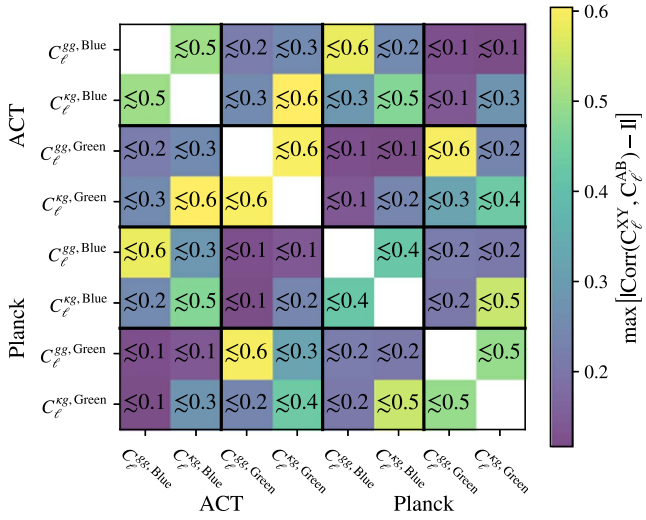

Figure 27. Maximum off-diagonal correlations between different samples and between cross-correlations using the ACT and Planck lensing reconstructions. The most significant off-diagonal correlations are present between the $C_\ell^{\kappa g}$ from different samples, which is due to the use of identical lensing maps and between C_ℓ^{gg} measured on the ACT and Planck footprints, due to the use of identical galaxy samples.

Appendix B
Detailed Summary of Null Tests

A detailed summary of all our lensing reconstruction null test results can be found in Table 4. We also show the corresponding band powers not already shown in the body of this paper in Figures 28, 29, 30 and 31. The tests targeting the spatial homogeneity of the data are summarized in Table 5, with band powers shown in Figure 32 and additionally in Figure 33.

We perform 12 null tests using different lensing reconstructions for each of the two galaxy samples, Blue and Green, and additionally a test on the cross-correlation between our galaxy samples and the curl mode of the baseline lensing reconstruction. The latter is primarily a test of our covariance estimation since we do not expect any signal in the curl mode of the lensing reconstruction at current levels of precision.

In Section 7.1, we discuss the observed failures and summarize our null tests targeting contamination of the lensing reconstruction. The number of observed failures is consistent with what would be expected due to random fluctuations given the correlations between the various tests. We nevertheless investigated whether the observed failures were indicative of contamination, for example, by considering alternative masks to maximize or minimize the contribution from potential contaminants. We performed the comparison of the minimum variance and polarization reconstructions on a more restrictive Galactic mask (see Figure 30); if the failures observed on the full footprint were due to contamination by polarized Galactic dust, we should have seen an improvement further away from the Galactic plane, and we do not. Alternatively, the effect should be more significant near the Galactic plane (i.e., in the region that is included in our baseline mask but not the more restrictive Galactic mask), but this is not the case (see Figure 29 panels (d) and (f)).

Our tests for the homogeneity of the data sets were discussed in Section 7.2. As pointed out there, we do not expect the null tests to pass, due to fluctuations in the selection properties of the galaxy sample on large scales. Those fluctuations affect,

Table 4
Summary of Null Tests for $C_\ell^{\kappa g}$

Null Test	Blue χ^2	Blue PTE	Green χ^2	Green PTE
Curl	11.06	0.136	13.64	0.058
Minimum variance—temperature only—polarization only				
$C_\ell^{\kappa\mathrm{MV}g} - C_\ell^{\kappa\mathrm{TT}g}$	15.20	0.033	8.52	0.289
$C_\ell^{\kappa\mathrm{MV}g} - C_\ell^{\kappa\mathrm{MVPOL}g}$	13.62	0.058	10.44	0.165
$C_\ell^{\kappa\mathrm{TT}g} - C_\ell^{\kappa\mathrm{MVPOL}g}$	14.97	0.036	9.67	0.208
$C_\ell^{\kappa\mathrm{MV}g} - C_\ell^{\kappa\mathrm{MVPOL}g}$ (40% gal. mask)	15.18	0.034	5.63	0.584
Minimum variance—temperature only—polarization only (near Galactic plane)				
$C_\ell^{\kappa\mathrm{MV}g} - C_\ell^{\kappa\mathrm{TT}g}$ (near Galactic plane)	7.40	0.388	6.76	0.454
$C_\ell^{\kappa\mathrm{MV}g} - C_\ell^{\kappa\mathrm{MVPOL}g}$ (near Galactic plane)	4.11	0.767	8.17	0.318
$C_\ell^{\kappa\mathrm{TT}g} - C_\ell^{\kappa\mathrm{MVPOL}g}$ (near Galactic plane)	4.98	0.663	6.37	0.497
Frequency difference tests				
$C_\ell^{\kappa\mathrm{MV,noise\ only}g}$ (150 GHz–90 GHz map level null test, minimum variance)	6.70	0.460	10.89	0.143
$C_\ell^{\kappa\mathrm{TT,noise\ only}g}$ (150 GHz–90 GHz map level null test, temperature only)	9.45	0.222	7.33	0.396
$C_\ell^{\kappa\mathrm{MV,150GHz}g} - C_\ell^{\kappa\mathrm{MV,90GHz}g}$ (150 GHz–90 GHz band power null test, minimum variance)	3.36	0.850	6.78	0.452
$C_\ell^{\kappa\mathrm{TT,150GHz}g} - C_\ell^{\kappa\mathrm{TT,90GHz}g}$ (150 GHz–90 GHz band power null test, temperature only)	2.35	0.938	10.79	0.148
Other				
Baseline versus CIB deprojection	16.09	0.024	10.21	0.177

Note. We compute the χ^2 within our cosmological analysis range of $50 \leqslant \ell \leqslant 400$ and estimate the PTE using a χ^2 distribution with 7 degrees of freedom (given the seven band powers in the analysis range). We find four failures (PTE <0.05), which are highly correlated; all relate to comparing the cross-correlation of the Blue sample of galaxies with different lensing reconstruction options (minimum variance, temperature only, and polarization only). We investigate in Section 7.1 potential systematic contamination, but stress that the number of failures is not inconsistent with random fluctuations, and no further evidence of contamination is found.

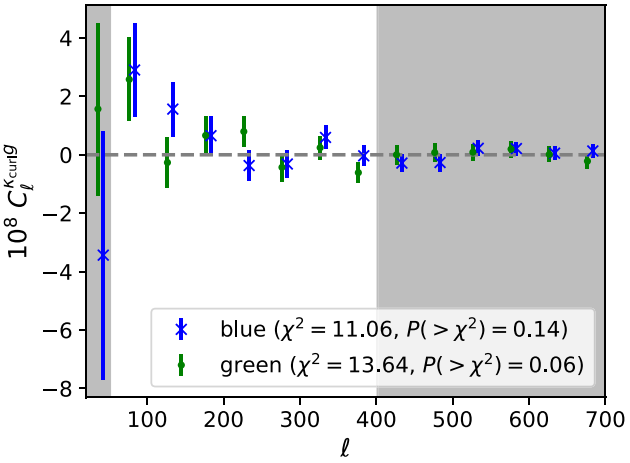

Figure 28. At current levels of precision, we do not expect any signal from the curl mode of the lensing reconstruction. The cross-correlation of the unWISE samples with the curl mode of the lensing reconstruction thus serves as a test of our covariance estimation.

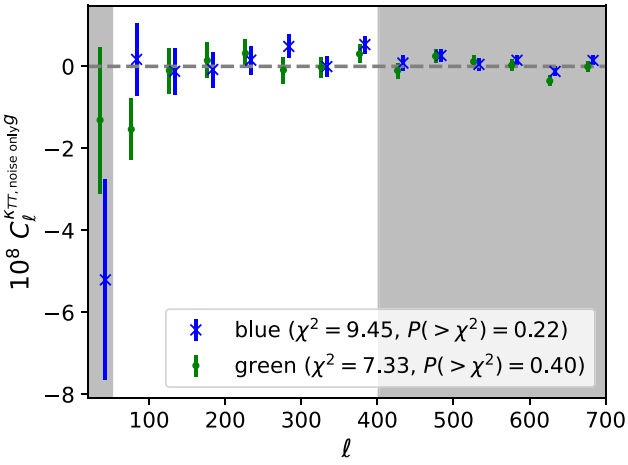

(a) temperature only reconstruction on 150 and 90GHz (noise only) difference maps

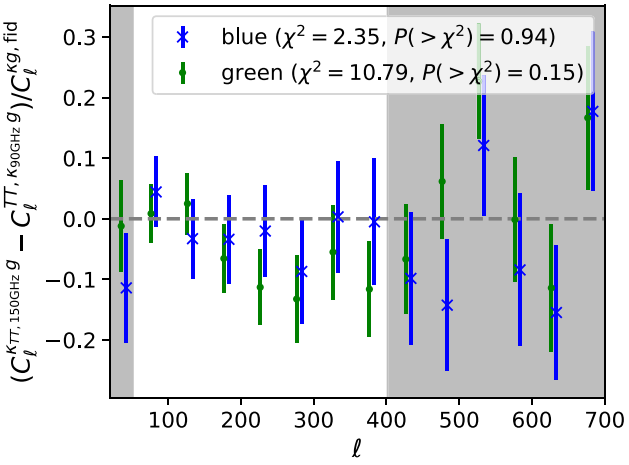

(b) difference of cross-correlation bandpowers using temperature only reconstructions at 150 and 90GHz

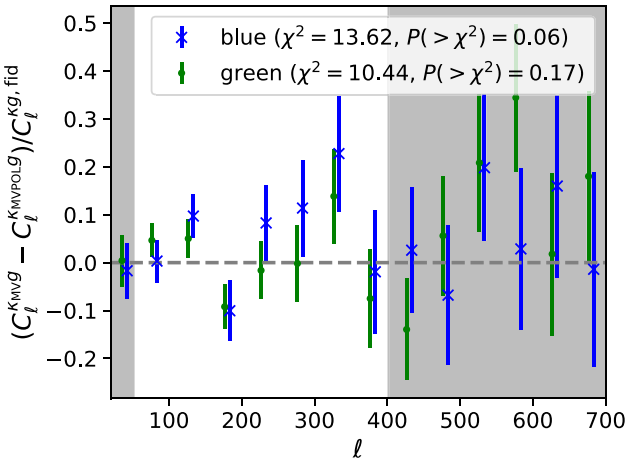

(c) difference of cross-correlation bandpowers using minimum variance and polarisation only reconstructions

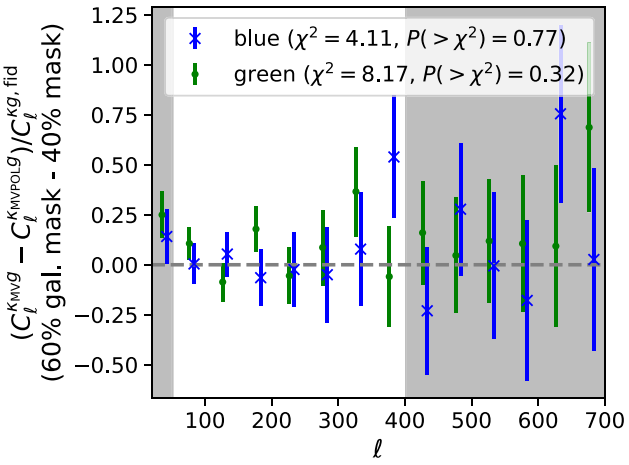

(d) same as (c) but on the difference region of the 60% and 40% masks

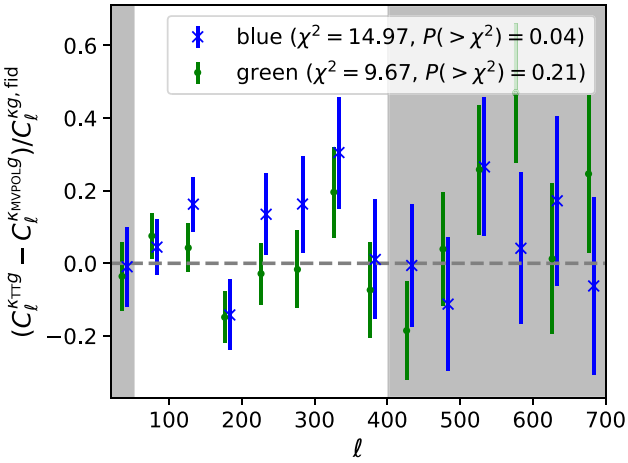

(e) difference of cross-correlation bandpowers using temperature only and polarisation only reconstructions

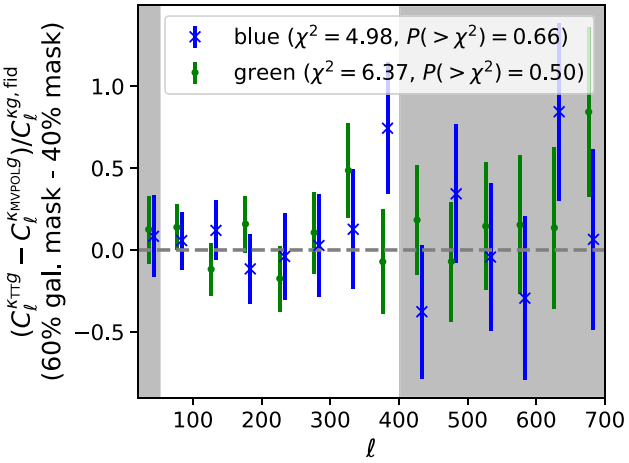

(f) same as (e) but on the difference region of the 60% and 40% masks

Figure 29. Summary of additional null tests related to potential foreground systematics in the lensing reconstruction. We compare cross-correlations with lensing reconstructions using only one of the two ACT frequencies (panels (a) and (b)), cross-correlations using the minimum variance and polarization-only reconstructions (panels (c) and (d)), and cross-correlations using the temperature-only and polarization-only reconstructions (panels (e) and (f)). The number of failures is consistent with expectations when taking into account the correlations between different tests.

Table 5
Summary of Null Tests Targeting the Spatial Homogeneity of the Galaxy Samples

	Blue						Green					
	$C_\ell^{\kappa g}$		C_ℓ^{gg}		$(C_\ell^{\kappa g})^2/C_\ell^{gg}$		$C_\ell^{\kappa g}$		C_ℓ^{gg}		$(C_\ell^{\kappa g})^2/C_\ell^{gg}$	
Null Test	χ^2	PTE	χ^2	PTE	χ^2	PTE	χ^2	PTE	χ^2	PTE	χ^2	PTE
40% Galactic mask	4.99	0.662	6.78	0.341	2.57	0.861	4.65	0.702	16.51	0.011	3.39	0.758
$\beta_{\rm ecliptic} > 30°$	7.43	0.386	30.19	0.000	5.63	0.466	10.39	0.168	45.79	0.000	2.65	0.851
SGC–NGC	1.94	0.963	2.66	0.850	2.18	0.903	2.03	0.958	4.59	0.597	4.04	0.672
Stricter stellar mask	4.83	0.681	7.65	0.265	…	…	4.72	0.694	4.50	0.609	…	…

Note. As expected we find some inhomogeneity in the galaxy sample, in particular with respect to cuts in ecliptic latitude. The χ^2 is computed within our cosmological analysis ranges of $50 \leqslant \ell \leqslant 400$ for $C_\ell^{\kappa g}$ and $100 \leqslant \ell \leqslant 400$ for C_ℓ^{gg}. We estimate the PTE using a χ^2 distribution with 7(6) degrees of freedom (given the 7(6) band powers in the analysis range for $C_\ell^{\kappa g}$ (C_ℓ^{gg})). As argued in Section 7.2, the failures are likely due to large-scale inhomogeneities in the galaxy selection, and thus, varying galaxy bias. The bias-independent combination $(C_\ell^{\kappa g})^2/C_\ell^{gg}$, however, passes our null tests.

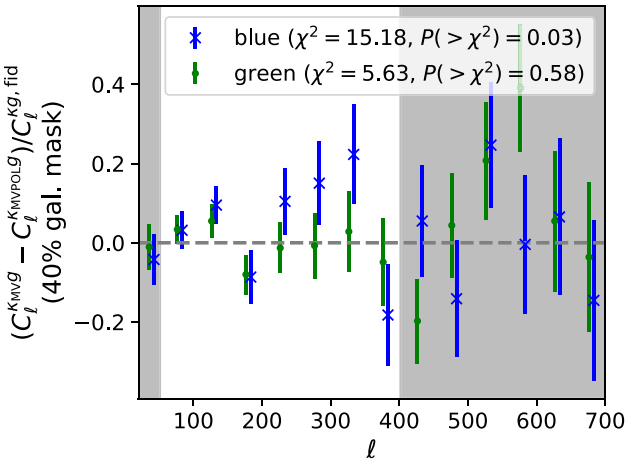

Figure 30. Null test showing the difference in cross-correlation band powers using minimum variance and polarization-only reconstructions on the more restrictive (40%) Galactic mask. We observe a failure for the Blue sample, which is highly correlated with other observed failures shown above. Overall, the number of failures is consistent with expectations, taking into account the correlations between our tests.

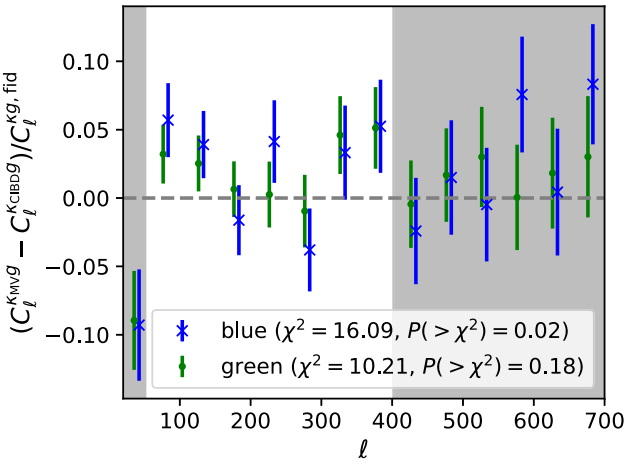

Figure 31. Null test showing the difference between cross-correlation band powers using our baseline reconstruction and one that explicitly deprojects CIB contamination using higher-frequency data from Planck. Again we see a failure for the Blue sample. We note, however, that we cannot rule out the possibility that this is related to a slightly different mask used for the CIB deprojected reconstruction, which removes some additional areas near the Galactic plane. Looking at the null test for the galaxy autocorrelation on the modified masks also yields a borderline PTE of 0.09.

among other things, the galaxy bias. We thus construct an approximately bias-independent quantity, $(C_\ell^{\kappa g})^2/C_\ell^{gg}$, on which we perform null tests to confirm the homogeneity of the data. In Figure 32 (panel (e)), we show this null test for the difference between our baseline analysis and an analysis restricted to an ecliptic latitude larger than 30°. This test primarily targets trends with unWISE depth, which varies with ecliptic latitude, due to the satellites' scan strategy. We also compared the band powers obtained on the SGC and NGC (panel (f)) and found those to be consistent as well. Finally, in Figure 33, we show tests for $C_\ell^{\kappa g}$ and C_ℓ^{gg} comparing different stellar masks. For this test, we mask $0.^\circ1$ around an additional 1.85 million stars with W2, W2, or 2MASS K_m brighter than an 8th magnitude, beyond the 12,890 very bright stars (W2 < 2.5) that we mask by default. This decreases the unmasked sky fraction in the unWISE mask from 0.58 to 0.45. The tests are passing, and because we are changing the mask on small scales rather than selecting a different region, we expect this test to be unaffected by large-scale fluctuations in the galaxy selection.

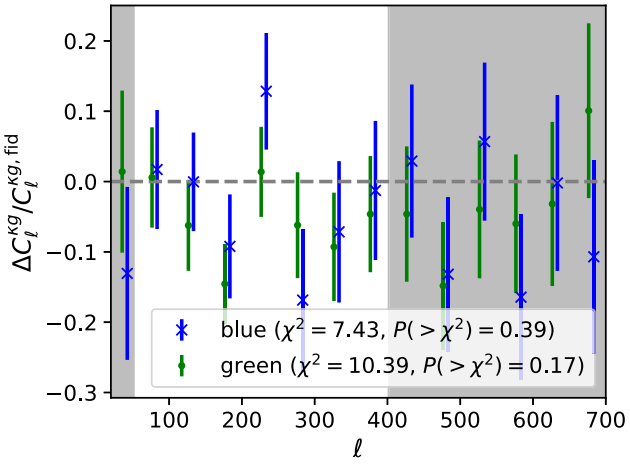

(a) Difference of $C_\ell^{\kappa g}$ measured in the baseline footprint and when restricted to ecliptic latitudes $> 30°$.

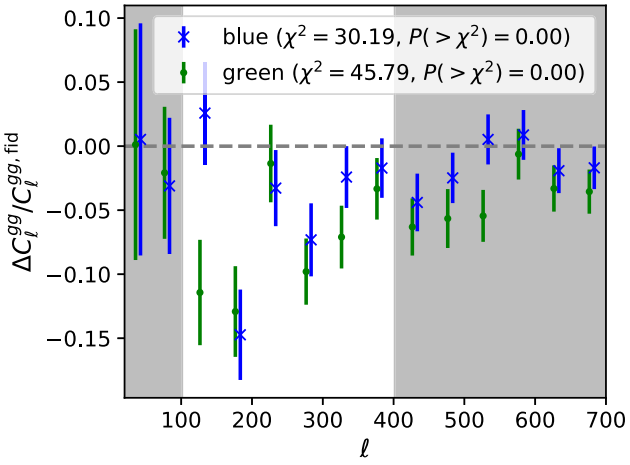

(b) Same as (a) but for C_ℓ^{gg}.

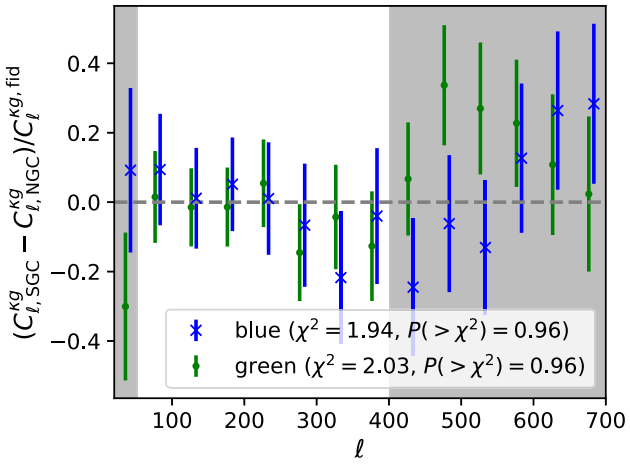

(c) Difference of $C_\ell^{\kappa g}$ measured in the southern and northern galactic cap (SGC and NGC)

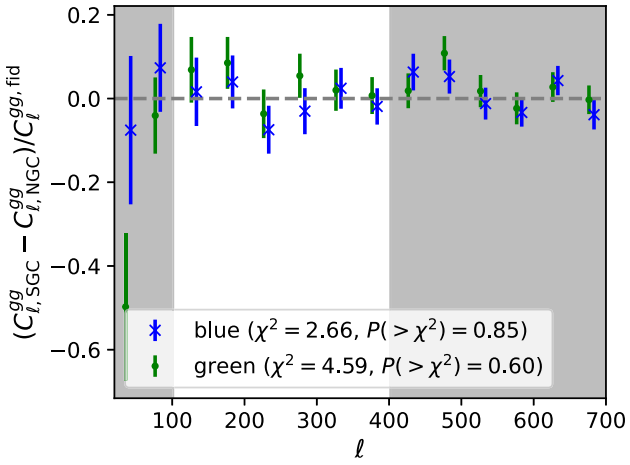

(d) Same as (c) but for C_ℓ^{gg}.

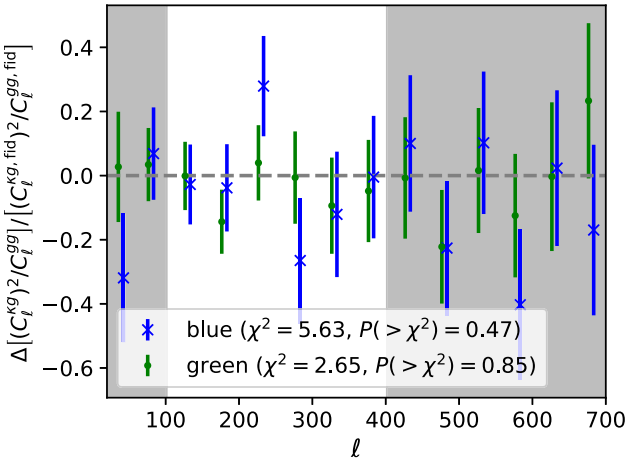

(e) Difference in the bias independent quantity $(C_\ell^{\kappa g})^2 \triangleleft C_\ell^{gg}$ measured in the baseline footprint and when restricted to ecliptic latitudes $> 30°$.

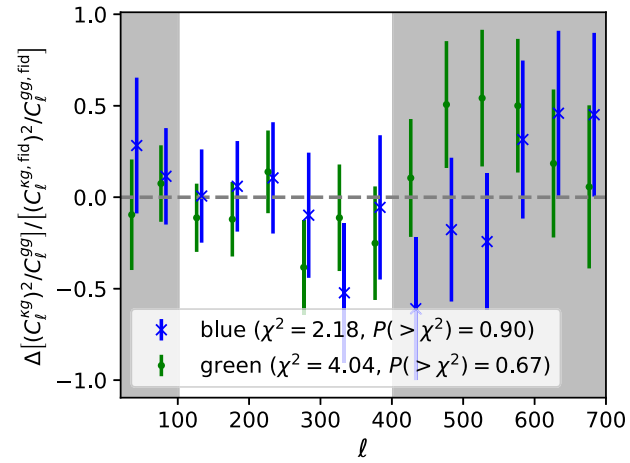

(f) Same as (e) but for the comparison between SGC and NGC.

Figure 32. Summary of additional null tests related to the spatial homogeneity of the observed spectra. We compare cross-correlations and galaxy autocorrelation spectra for different ecliptic latitudes (panels (a) and (b)) and between the SGC and NGC (panels (c) and (d)). In addition, we show the approximately bias-independent quantity $(C_\ell^{\kappa g})^2/C_\ell^{gg}$ for these two comparisons (panels (e) and (f)). While we find several highly significant failures for C_ℓ^{gg} caused by variations in the galaxy bias arising from large-scale fluctuations in the galaxy selection properties, the bias-independent quantity $(C_\ell^{\kappa g})^2/C_\ell^{gg}$ passes our tests.

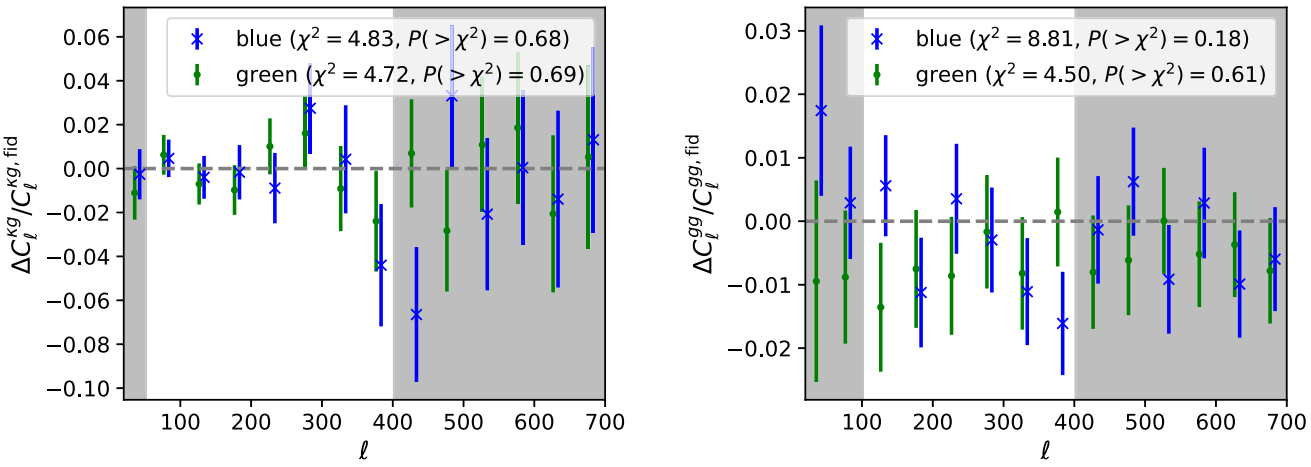

Figure 33. These null tests compare our baseline mask, which removes any source within 2.″75 from a Gaia point source (with W2 < 2.5), with one that additionally masks any source within 0.°1 from a further 1.85 million stars brighter than 8th magnitude. We find no evidence for problems with stellar contamination. This is consistent with results from alternative estimates of the stellar contamination in Krolewski et al. (2020).

Appendix C
Details of the Power Spectrum Model

In this appendix, we discuss the details of our correction for the dependence of the cross-correlation redshifts on the fiducial cosmology, as well as our correction for the noise bias introduced by marginalization over redshift uncertainties.

In Section 8.2, we raised the need to assume a fiducial cosmology to interpret the cross-correlation between the photometric and spectroscopic samples as estimates of $b(z)dN/dz$. In this appendix, we lay out a formalism for correcting for this assumption to avoid biasing our results (Appendix C.1).

In Section 8.2, we discussed the effect of imposing smoothness and positivity on the normalized cross-correlation redshifts, $W^{\mathrm{xc}}(z)$. The result is a noise bias introduced by our marginalization procedure since the final C_ℓ effectively becomes a nonlinear function of a noisy quantity. This bias can be as large as ∼5% for some of the terms contributing to C_ℓ^{gg} in some range of ℓs. The effect is less significant for $C_\ell^{\kappa g}$, but still remains comparable to the data covariance. In Appendix C.2, we detail how we subtract this noise bias.

C.1. Correction for the Fiducial Cosmology Assumed in Determining Cross-correlation Redshifts

As described in Section 3.1.2 (with further details provided in Krolewski et al. 2020 and Appendix K), we measure the redshift distribution of unWISE galaxies using cross-correlations with spectroscopic surveys. This introduces a dependence on the fiducial cosmology assumed in the process of converting from the measured cross-correlation functions to an estimate of $b(z)dN/dz$ (Krolewski et al. 2021). To correct for this dependence we introduce a new method, which is exact in the limit of narrow redshift bins used to measure the cross-correlations between the photometric and spectroscopic samples.

We measure the cross-correlations between the photometric unWISE sample (subsequently indicated by a subscript p) and multiple spectroscopic tracers (subsequently denoted with a subscript s) as well as the spectroscopic sample's autocorrelation in N narrow redshift bins between $z_{\mathrm{min},i}$ and $z_{\mathrm{max},i}$ $(i = 1,\ldots,N)$. Assuming scale-independent bias[71] and linear bias, the relevant correlation functions are given in theory by

$$w_{\mathrm{sp}}(\theta, z_i) = \int \frac{kdk}{2\pi} \int_{z_{\mathrm{min},i}}^{z_{\mathrm{max},i}} dz J_0[k\theta\chi(z)] b_s \times \frac{dN_s}{dz} b_p \frac{dN_p}{dz} H(z) P_{mm}(k, z) \tag{C1}$$

$$w_{\mathrm{ss}}(\theta, z_i) = \int \frac{kdk}{2\pi} \int_{z_{\mathrm{min},i}}^{z_{\mathrm{max},i}} \times dz J_0[k\theta\chi(z)] \left(b_s \frac{dN_s}{dz}\right)^2 H(z) P_{mm}(k, z). \tag{C2}$$

Here b_s and b_p are the bias of the spectroscopic and photometric samples, respectively, and dN_s/dz and dN_p/dz are the corresponding redshift distributions. The comoving radial distance, $\chi(z)$, the Hubble rate $H(z)$, and the matter–matter power spectrum $P_{mm}(k, z)$ depend on the assumed cosmology.

Furthermore, the correlation functions are binned into $n = 3$ log-spaced angular bins between $\theta_{\mathrm{min}} = s_{\mathrm{min}}/\chi_{\mathrm{fid}}(z_{\mathrm{central}})$ and $\theta_{\mathrm{max}} = s_{\mathrm{max}}/\chi_{\mathrm{fid}}(z_{\mathrm{central}})$, where $s_{\mathrm{min}} = 2.5\ h^{-1}$ Mpc and $s_{\mathrm{max}} = 10\ h^{-1}$ Mpc. Here χ_{fid} denotes the comoving radial distance within the chosen fiducial cosmology. Finally, the resulting quantity is integrated over the full range of scales weighting by θ^{-1} to increase the S/N (Ménard et al. 2013), yielding

$$\bar{w}_{XY}(z_i) = \sum_{j=1}^{n} \frac{2\Delta\theta_j}{\theta_j(\theta_{\mathrm{max},j}^2 - \theta_{\mathrm{min},j}^2)} \int_{\theta_{\mathrm{min},j}}^{\theta_{\mathrm{max},j}} \theta d\theta\ w_{XY}(\theta, z_i). \tag{C3}$$

In the limit of narrow redshift bins, we can estimate the spectroscopic bias, b_s, from the measured binned and integrated

[71] This assumption is tested to some extent in our mocks used for model verification, where we have also measured the cross-correlation redshifts on the same scales as in our analysis. The ability to recover an unbiased cosmology discussed in Section 8.3 indicates that this does not bias our constraints. Moreover, we find similar cosmological parameters (shift of -0.1σ in S_8) when increasing the minimum scale used in the cross-correlation redshifts, which decreases the sensitivity to scale-dependent bias.

Table 6
Details of the Series of Parameter-level Consistency Tests Performed

		ΔS_8	$\Delta S_8^\times$	PTE
TT only	Blue	$-0.035(^{+0.027}_{-0.043})$[a]	$-0.031(^{+0.025}_{-0.039})$[a]	⋯
	Green	0.012 ± 0.010	0.010 ± 0.009	0.24
	Blue+Green	-0.014 ± 0.010	-0.011 ± 0.009	0.22
$\beta_{\rm ecliptic} > 30°$	Blue	$0.008(^{+0.033}_{-0.040})$[a]	$0.019(^{+0.031}_{-0.038})$[a]	⋯
	Green	-0.0003 ± 0.025	-0.0004 ± 0.021	0.99
	Blue+Green	-0.005 ± 0.020	-0.003 ± 0.017	0.86
$\beta_{\rm ecliptic} > 30°$ (restricted x-corr. dN/dz)	Blue	$0.016(^{+0.034}_{-0.046})$[a]	$0.026(^{+0.032}_{-0.043})$[a]	⋯
	Green	0.0142 ± 0.025	0.0147 ± 0.021	0.48
	Blue+Green	0.0101 ± 0.022	0.0129 ± 0.019	0.49
40% Galactic mask	Blue	$-0.0001(^{+0.027}_{-0.034})$[a]	$0.006(^{+0.024}_{-0.031})$[a]	⋯
	Green	-0.001 ± 0.012	0.002 ± 0.011	0.85
	Blue+Green	-0.002 ± 0.008	0.001 ± 0.008	0.87
$\ell_{\rm min}^{gg} = 150$, $\ell_{\rm min}^{\kappa g} = 100$	Blue	$0.019(^{+0.027}_{-0.034})$[a]	$0.019(^{+0.027}_{-0.033})$[a]	⋯
	Green	0.006 ± 0.015	0.005 ± 0.011	0.64
	Blue+Green	0.006 ± 0.011	0.005 ± 0.009	0.55
$\ell_{\rm max} = 300$	Blue	$-0.002(^{+0.028}_{-0.041})$[a]	$-0.003(^{+0.025}_{-0.036})$[a]	⋯
	Green	-0.003 ± 0.014	-0.003 ± 0.012	0.80
	Blue+Green	-0.001 ± 0.010	-0.002 ± 0.010	0.88
Higher-order bias priors $\times 2$	Blue	$-0.033(^{+0.027}_{-0.077})$[a]	$-0.031(^{+0.023}_{-0.070})$[a]	⋯
	Green	-0.009 ± 0.020	-0.009 ± 0.019	0.63
	Blue+Green	-0.010 ± 0.016	-0.010 ± 0.015	0.47
More restrictive $b(z)dN/dz$ scale cut	Blue	$0.002(^{+0.025}_{-0.039})$[a]	$0.002(^{+0.022}_{-0.034})$[a]	⋯
	Green	-0.004 ± 0.005	-0.004 ± 0.005	0.46
	Blue+Green	-0.002 ± 0.002	-0.002 ± 0.003	0.52
NGC–SGC	Blue	-0.029 ± 0.063	-0.039 ± 0.059	0.48
	Green	0.101 ± 0.059	0.088 ± 0.052	0.09
	Blue+Green	0.032 ± 0.040	0.032 ± 0.044	0.46

Notes. These tests were originally performed blind using random offsets on the cosmological parameters. We show the difference in the inferred S_8 and $S_8^\times$ for these analyses compared to our baseline analysis (and the difference between analyses using only the NGC and SGC, respectively). Note that the uncertainty quoted is the uncertainty on the difference between the baseline analysis and the subset analysis estimated under the assumption that the posteriors are approximately Gaussian, following the prescription from Gratton & Challinor (2020). In the case of the comparison of analyses performed on the NGC and SGC, the two analyses are fully independent, and we estimate the consistency between the two data sets, taking into account the full non-Gaussian posterior using the tensiometer package. We estimate the statistical likelihood of the shifts obtained, assuming that we are effectively probing a single parameter, $S_8^\times$. We find all consistency tests to yield shifts consistent with expectations based on random fluctuations within $<2\sigma$.

[a] The posteriors on S_8 and $S_8^\times$ for analyses using only the Blue sample are not well approximated by Gaussians. Therefore, we were unable to reliably estimate the significance of the shift for these consistency tests. We nevertheless show here the shift in the parameter mean, which is, in most cases, small compared to the measurement errors shown in parentheses.

autocorrelation function as

$$\hat{b}_s(z_i) = \sqrt{\hat{\tilde{w}}_{\rm ss}(z_i)}\left[\Delta z_i \left(\frac{dN_s}{dz}\right)^2 H(z_i) \int k dk P_{mm}(k, z_i) W(k, z_i)\right]^{-1/2}, \tag{C4}$$

where $W(k, z)$ is a weighting function, which can be computed analytically as

$$W(k, z) = \sum_{j=1}^{n} \frac{\Delta\theta_j [\theta_{{\rm max},j} J_1(k\chi(z)\theta_{{\rm max},j}) - \theta_{{\rm min},j} J_1(k\chi(z)\theta_{{\rm min},j})]}{k\chi(z)\theta_j \pi(\theta_{{\rm max},j}^2 - \theta_{{\rm min},j}^2)}. \tag{C5}$$

Finally, we can obtain an estimate of $b_p dN_p/dz$ as

$$\widehat{b_p \frac{dN_p}{dz}} = \frac{\hat{\tilde{w}}_{\rm sp}(z_i)}{\sqrt{\hat{\tilde{w}}_{\rm ss}(z_i)}}\left[\Delta z_i H(z_i) \int k dk P_{mm}(k, z_i) W(k, z_i)\right]^{-1/2}. \tag{C6}$$

Given $(\widehat{b_p dN_p/dz})_{\rm fid}$ measured in a chosen fiducial cosmology the dependence on the choice of fiducial cosmology can therefore be corrected as

$$\widehat{b_p \frac{dN_p}{dz}} = \left(\widehat{b_p \frac{dN_p}{dz}}\right)_{\rm fid} \frac{\mathcal{C}}{\mathcal{C}_{\rm fid}} \tag{C7}$$

with

$$\mathcal{C} = \left[\Delta z_i H(z_i) \int k dk P_{mm}(k, z_i) W(k, z_i)\right]^{-1/2}. \quad \text{(C8)}$$

In our analysis, we compute $\mathcal{C}$ for every new cosmology to avoid biasing our results through the dependence on the assumed fiducial cosmology. For consistency with the method used to measure the cross-correlation redshifts, we use an `HMCode` model for $P_{gg}(k, z)$. We show in Table 6 that our S_8 constraints are unchanged even when using a different fiducial cosmology, validating the correction of Equation (C8).

C.2. Noise Bias Correction

Similarly to Krolewski et al. (2021), we compute a correction for the noise bias introduced by marginalization over uncertainties in the redshift distributions within a fiducial cosmology (again taken to be the mean cosmology from Planck Collaboration et al. 2020a). First, we draw 9000 sets of PCA coefficients for each of the galaxy samples according to the skew-normal priors obtained as described in Section 8.2 and summarized in Table 2. This number is chosen such that the resulting uncertainty in the correction is highly subdominant compared to the data covariance. We then evaluate the power spectrum model term by term for each set of coefficients and obtain the noise bias as

$$(\Delta C_\ell^{XY})_{\text{noise bias}} = \langle C_\ell^{XY,\text{theory}} \rangle_{c_1,\ldots,c_n} - C_\ell^{XY,\text{theory}}|_{c_1=\ldots=c_n=0}, \quad \text{(C9)}$$

where $C_\ell^{XY,\text{theory}}$ are the various terms contributing to our theory expressions for C_ℓ^{gg} and $C_\ell^{\kappa g}$. During the cosmology analysis, we then correct the theory spectra as

$$(C_\ell^{XY,\text{theory}})_{\text{corrected}} = C_\ell^{XY,\text{theory}} - (\Delta C_\ell^{XY})_{\text{noise bias}}. \quad \text{(C10)}$$

In this process, we scale our noise bias correction appropriately with the value of the nuisance parameters, including galaxy bias parameters and lensing magnification parameters.

Appendix D
Posterior Distributions for the Full Parameter Space

In Figures 34 and 35, we show the posterior distributions for the full parameter space, including the galaxy nuisance parameters for the Blue and Green samples of unWISE galaxies, respectively. The posteriors shown are for our baseline analysis without BAO. Alongside the posterior distributions, we also show the maximum a posterior (MAP) and the priors on all sampled parameters. We observe that the data does not constrain the redshift distribution marginalization parameters beyond the information provided by the priors. These parameters are also only very weakly degenerate with the cosmological parameters of interest. In the case of the free parameters modifying the evolution of the higher-order bias, we see that the only parameter that is constrained by the data is the offset in the second-order Lagrangian bias for the Blue sample. This parameter has some degeneracy with cosmology (see Appendix E for some discussion of this). For the Green sample, higher-order contributions are less significant, and the constraints on the higher-order bias parameters are prior dominated.

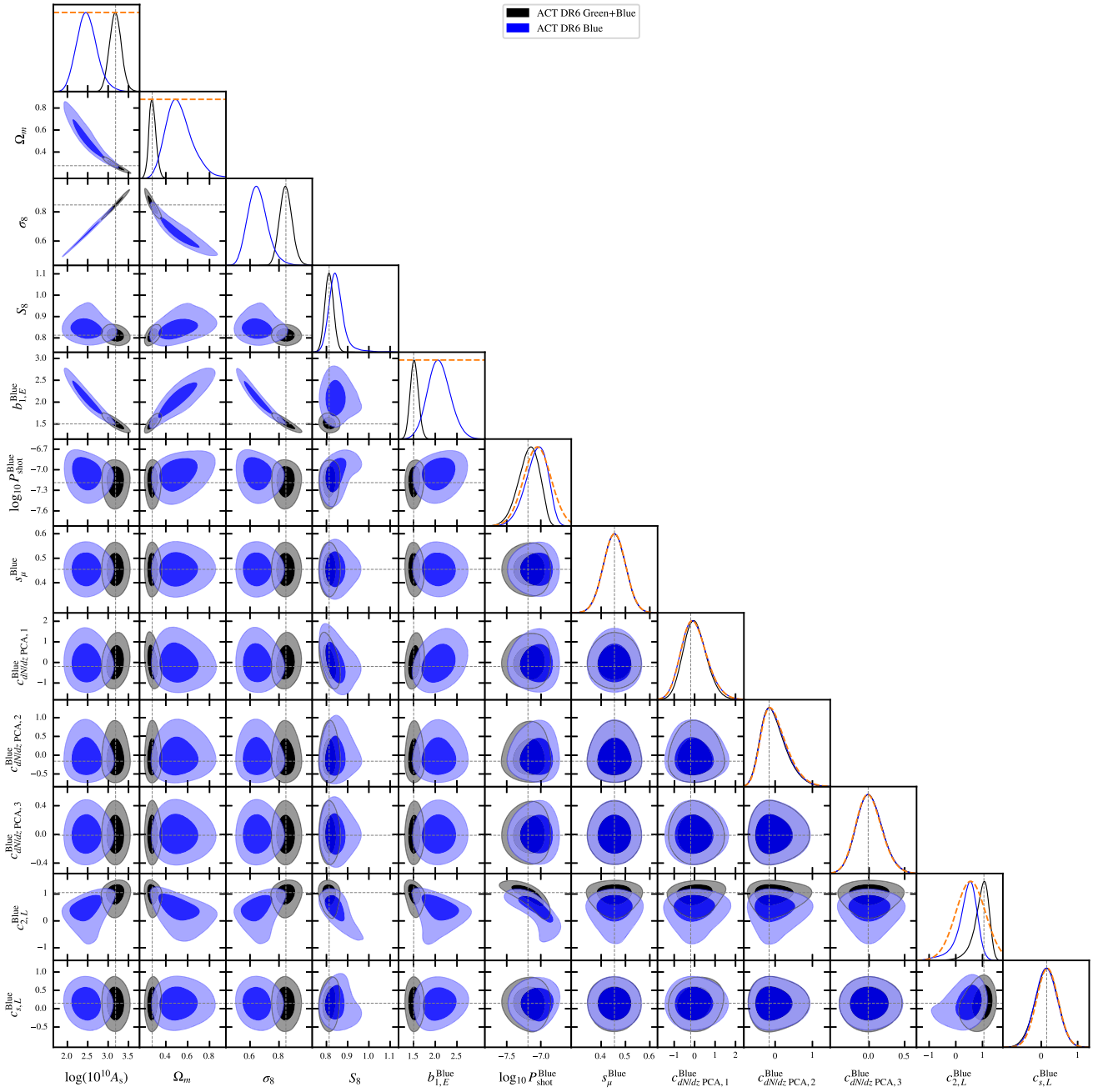

Figure 34. Posterior distributions in the full parameter space including the galaxy nuisance parameters for the Blue sample of unWISE galaxies. The dashed gray lines indicate the MAP and the orange dashed lines show the priors on all sample parameters. We observe that the data does not constrain the redshift distribution beyond the priors provided, which are described in Section 8.2. On the other hand the data is informative for the second-order Lagrangian bias.

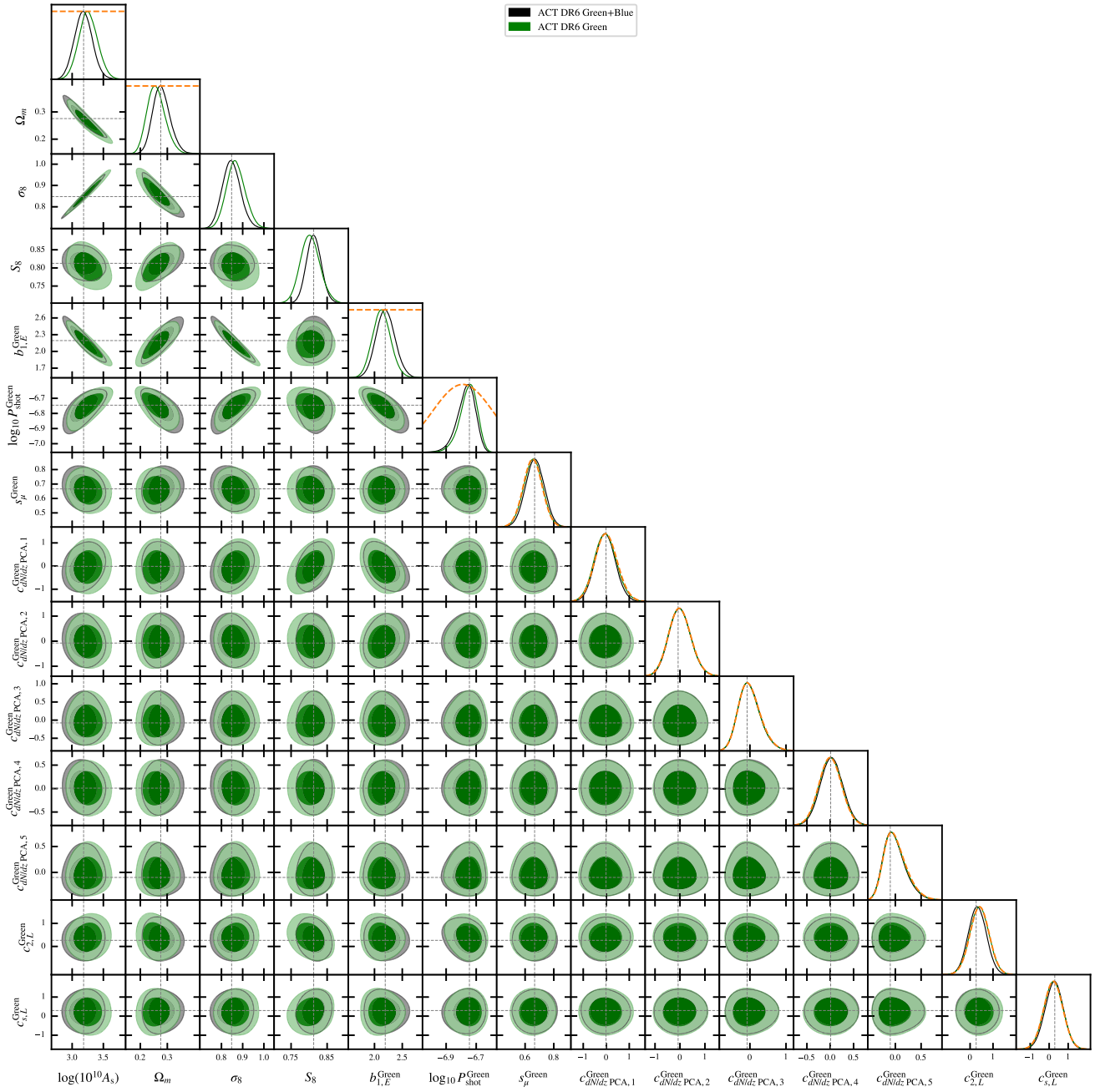

Figure 35. Same as Figure 34 for the Green sample of unWISE galaxies. As with the Blue sample, the redshift distribution parameters are not constrained by the data. In contrast with the Blue sample, the higher-order biases are also prior dominated since these contributions are significantly smaller for the Green sample.

Appendix E
Parameter Consistency from Blue and Green

In Section 9.5, we presented posteriors on cosmological parameters obtained from the analysis of the autocorrelation of the two unWISE redshift samples, Blue and Green, independently, and their cross-correlation with CMB lensing reconstructions from ACT. Our analysis is primarily sensitive to the amplitude of the signal, which depends on the parameter combination $S_8^\times \equiv \sigma_8(\Omega_m/0.3)^{0.45}$. When using only a single tomographic bin (and neglecting structure growth within the bin), σ_8 and Ω_m are exactly degenerate at linear order. Constraints on either parameter individually, therefore, arise only from beyond linear order contributions to the spectrum. Therefore, the inference of σ_8 and Ω_m is very sensitively dependent on the priors on higher-order parameters. In Figure 36, we can see that σ_8 and Ω_m show a strong degeneracy with $c_{2,L}^{\rm Blue}$, the free parameter offsetting the second-order Lagrangian bias for the Blue sample. S_8, on the other hand, shows a much weaker degeneracy with the higher-order bias parameters. The degeneracy is broken when both tomographic samples are included or when we additionally include BAO information.

Given the sensitivity to the higher-order bias priors, we thus do not necessarily expect the two samples to yield the same values for σ_8 or Ω_m, and the fact that they are consistent at 1.7σ suggests that our choice of priors is reasonable.

Furthermore, our tests described in Section 7.2 specifically ensured that the bias-independent amplitude of our spectra remained consistent across different subsets of the data. We

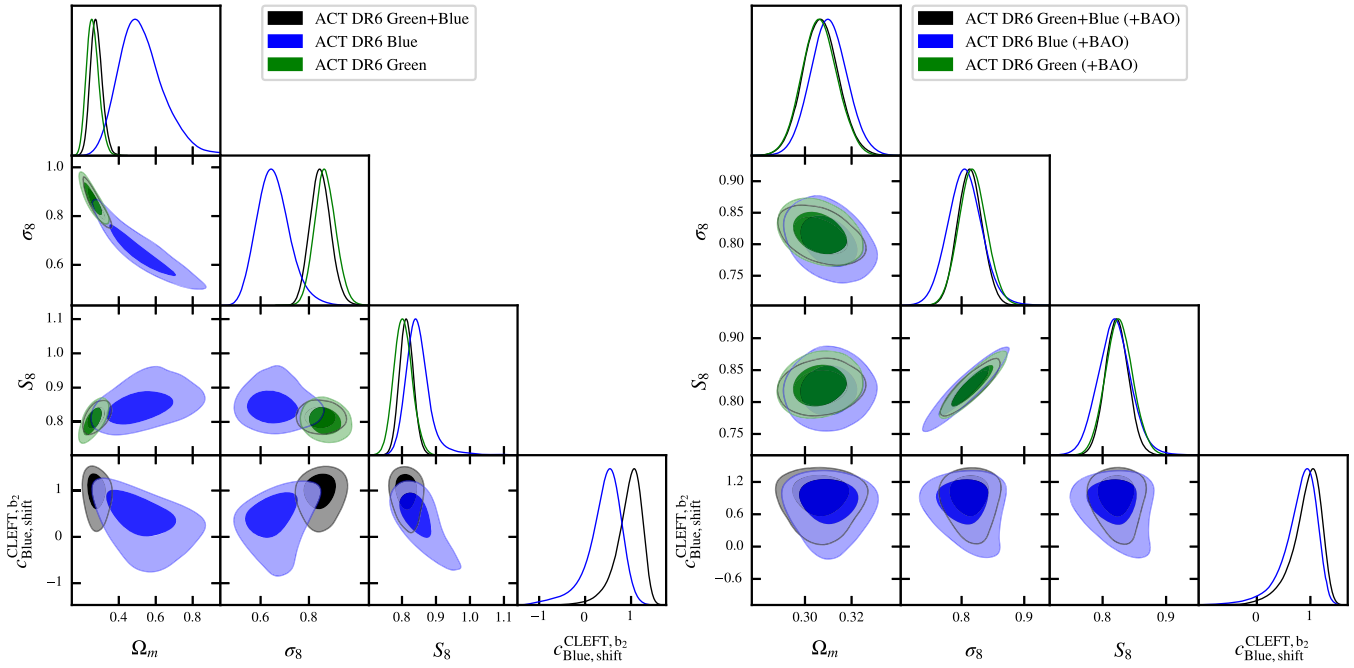

Figure 36. When plotting the posterior for the second-order Lagrangian bias parameter, $c_{2,L}^{\mathrm{Blue}}$, along with the cosmological parameters, we can see that the σ_8 and Ω_m are highly degenerate with this parameter when using only the combination of C_ℓ^{gg} and $C_\ell^{\kappa g}$ (left). This is in contrast to S_8, which is only weakly dependent on the higher-order bias. With BAO data (right), this degeneracy is broken, and the inferred parameters are less sensitive to the higher-order bias priors.

thus cannot rule out that the exact scale dependence of the spectrum, which gives rise to the weak constraints on σ_8 and Ω_m in this type of analysis, is affected to some degree by residual systematic contamination.

In the parameter that is sensitive to the amplitude of the spectrum, S_8 (or $S_8^{\times}$), on the other hand, we find good agreement between the samples and thus consider it justified to combine them.

Appendix F
Summary of all Parameter Consistency Tests

In Table 6, we show a summary of several parameter consistency tests performed in this work; these employ various subsets of our baseline data set and are described in Section 9.7. We also summarize more consistency tests for alternative analysis choices in Table 7. Finally, in Figures 37 and 38, we show the consistency between σ_8 and Ω_m inferred using various subsets of the data and alternative analysis choices. We note that these parameters are individually only poorly constrained, and the posteriors are highly non-Gaussian. Therefore, we are unable to estimate the significance of the observed shifts. We note, however, that in all but three cases, the mean σ_8 and Ω_m fall within the 68% confidence region of our baseline analysis. The only exceptions arise when restricting the analysis to ecliptic latitudes larger than 30° for the Blue sample and considering only the NGC for the Blue or Green sample. In these cases the data volume is significantly reduced so that larger shifts are expected.

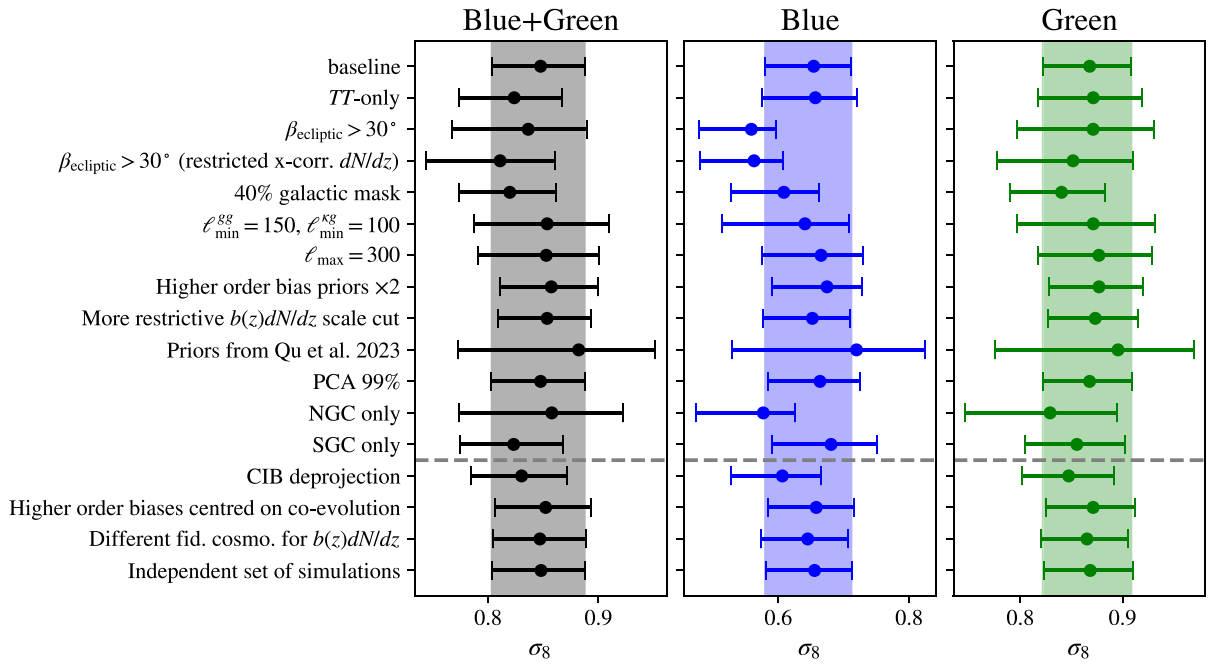

Figure 37. Like Figure 21 but showing the constraints on σ_8 for various subset analyses. The posteriors are highly non-Gaussian, and because the different analyses are not independent, we are unable to reliably estimate the significance of the parameter shifts observed. However, as argued in Section 9.7, comparisons of the best constraint parameter combination $S_8^{\times}$ show no evidence for any significant bias with all shifts consistent with expectations based on reduced data volume.

Table 7
Further Parameter Consistency Tests Not Involving a Subset of Our Baseline Analysis

		S_8	ΔS_8	$S_8^{\times}$	$\Delta S_8^{\times}$
CIB deprojection	Blue	$0.833^{+0.026}_{-0.034}$	0.016	$0.807^{+0.024}_{-0.031}$	0.020
	Green	0.789 ± 0.027	0.014	0.794 ± 0.024	−0.015
	Blue+Green	0.800 ± 0.021	0.013	0.803 ± 0.019	0.013
Higher-order biases centered on coevolution	Blue	$0.886^{+0.030}_{-0.070}$	−0.037	$0.860^{+0.028}_{-0.064}$	−0.033
	Green	$0.812^{+0.026}_{-0.032}$	−0.009	$0.818^{+0.024}_{-0.029}$	−0.008
	Blue+Green	$0.826^{+0.022}_{-0.026}$	−0.013	$0.829^{+0.020}_{-0.024}$	−0.012
Different fid. cosmo. for $b(z)dN/dz$	Blue	$0.842^{+0.024}_{-0.038}$	0.007	$0.819^{+0.021}_{-0.034}$	0.008
	Green	0.801 ± 0.026	0.002	0.807 ± 0.024	0.002
	Blue+Green	0.809 ± 0.020	0.004	0.812 ± 0.019	0.004
Independent set of simulations	Blue	$0.847^{+0.025}_{-0.037}$	0.002	$0.825^{+0.022}_{-0.033}$	0.002
	Green	$0.803^{+0.025}_{-0.028}$	0.0004	$0.809^{+0.022}_{-0.025}$	0.0003
	Blue+Green	0.813 ± 0.021	0.0001	0.816 ± 0.019	0.0001
`HMCode`-only model	Blue	0.821 ± 0.024	0.028	0.806 ± 0.023	0.021
	Green	0.802 ± 0.025	0.001	0.808 ± 0.023	0.002
	Blue+Green	0.812 ± 0.019	0.002	0.814 ± 0.018	0.002
Fixed fid. higher-order biases	Blue	0.869 ± 0.025	−0.02	0.842 ± 0.023	−0.015
	Green	0.807 ± 0.025	−0.004	0.812 ± 0.022	−0.003
	Blue+Green	0.826 ± 0.021	−0.013	0.829 ± 0.018	−0.012
No mag. bias	Blue	$0.856^{+0.019}_{-0.047}$	−0.007	$0.833^{+0.017}_{-0.042}$	−0.006
	Green	$0.815^{+0.026}_{-0.029}$	−0.012	$0.823^{+0.024}_{-0.027}$	−0.013
	Blue+Green	0.817 ± 0.021	−0.004	0.823 ± 0.019	−0.007

Note. For our consistency test using a lensing reconstruction with explicit CIB deprojection, alternative analysis choices in regards to the higher-order bias priors and the fiducial cosmology assumed for the cross-correlation redshifts, it is less straightforward to estimate the statistical significance of the observed parameter shifts. However, as can be seen here, the impact of these alternative analysis choices is small compared to our uncertainties. We also show an analysis run with a covariance obtained from an independent set of 400 simulations. The stability of the results indicates that our covariance is sufficiently converged. Furthermore, we summarized analyses using simplified models, an analysis using only the `HMCode` matter power spectrum, an analysis fixing all higher-order biases to the fiducial coevolution relations, and an analysis neglecting all magnification bias contributions. While these analyses are not necessarily expected to be consistent without baseline results, they provide an indication of the importance of different model components. We find that the shifts induced by these simplified models are small compared to our uncertainties, but they also do not yield dramatic improvements in constraining power.

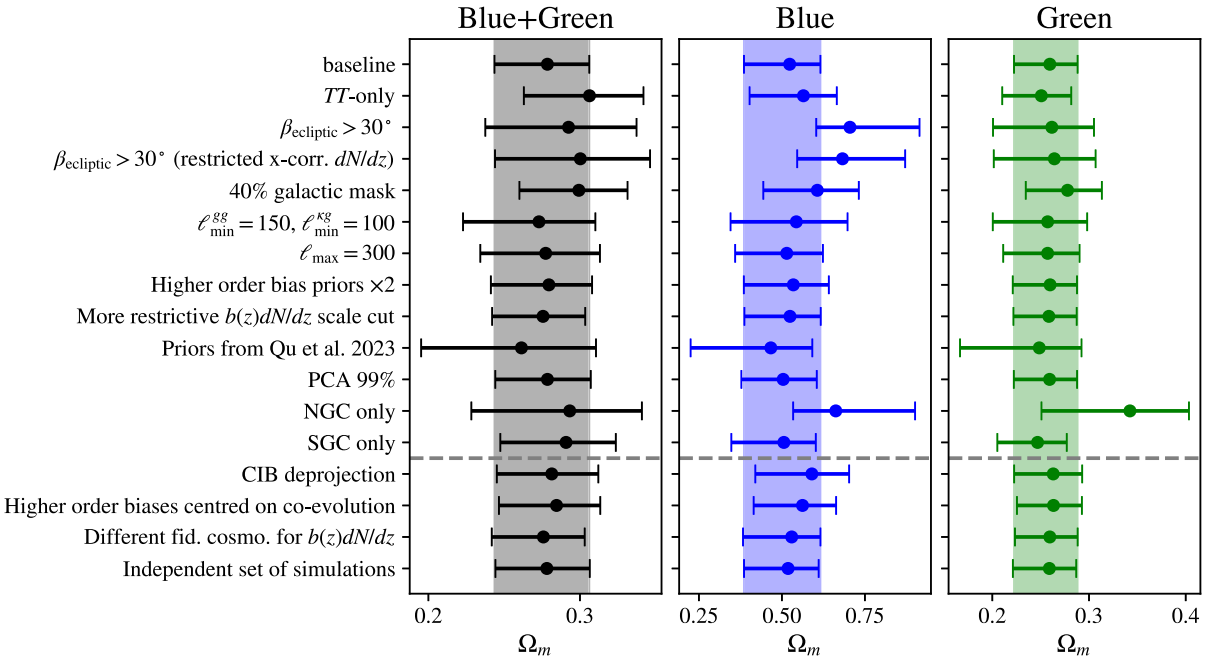

Figure 38. Like Figures 21 and 37 but showing the constraints on Ω_m. As in Figure 37, we are unable to reliably estimate the significance of the shifts given the highly non-Gaussian posteriors and the correlations between different data subsets.

Appendix G
Alternative Priors

In this appendix, we explore the impact of an alternative set of priors on cosmological parameters. In particular, we adopt a set of priors compatible with those from Qu et al. (2024). The main difference between the priors adopted in this work (see Table 2) and those from Qu et al. (2024) is the fact that H_0 is left to vary with a uniform prior between 40 and 100 km s^{-1} Mpc^{-1}. Additionally, Qu et al. (2024) adopt priors on n_s and $\Omega_b h^2$ rather than fixing those parameters to the mean values from Planck (Planck Collaboration et al. 2020a). We summarize this alternative set of priors in Table 8.

We find $S_8 = 0.810 \pm 0.021$ from the combination of the galaxy autocorrelation and the cross-correlation measurements using both samples of unWISE galaxies, only a small degradation of constraining power compared to our baseline analysis (see Section 9.5). Adding BAO information, we obtain $\sigma_8 = 0.812 \pm 0.023$, which is a more significant degradation of constraining power compared to our baseline analysis with BAO. This is explained by the fact that BAO data provide constraints primarily in the Ω_m–H_0 plane. In our baseline analysis, these two parameters do not vary independently, so the addition of BAO information directly represents a constraint on Ω_m, which breaks the degeneracy between σ_8 and Ω_m more effectively than in the case where H_0 is allowed to vary independently. The resulting posteriors from this analysis are shown in Figure 39 and constraints are summarized in Table 9.

Table 8
Priors Adopted from Qu et al. (2024)

Parameter	Prior
$\ln(10^{10}A_s)$	[2,4]
H_0	[40,100]
n_s	$\mathcal{N}(0.96,0.02)$
$\Omega_b h^2$	$\mathcal{N}(0.0223,0.0005)$
$\Omega_c h^2$	[0.005,0.99]

Note. These are identical to those used in the lensing power spectrum analysis performed by the Planck team (Planck Collaboration et al. 2020b). For the galaxy nuisance parameters, we adopt the same priors as in Table 2.

As we argued in Section 9.3, the angular size of the sound horizon, $\theta_{\rm MC}$, which within a ΛCDM cosmology determines the combination $\Omega_m h^3$, is measured with great precision by Planck (Planck Collaboration et al. 2020a). In the context of aiming to compare the amplitude of low-redshift structure to expectations from fits to the primary CMB, it is reasonable to adopt this constraint that helps break the degeneracy between distances and structure growth. Since we are here primarily interested in investigating the claimed S_8 tension, we adopt this approach as our baseline, but will investigate other options that allow one to probe alternative cosmologies in future work. We also note that the comparison with other works that constrain S_8 without the addition of BAO is still meaningful as we showed above that our S_8 constraints are not significantly affected by this choice of priors.

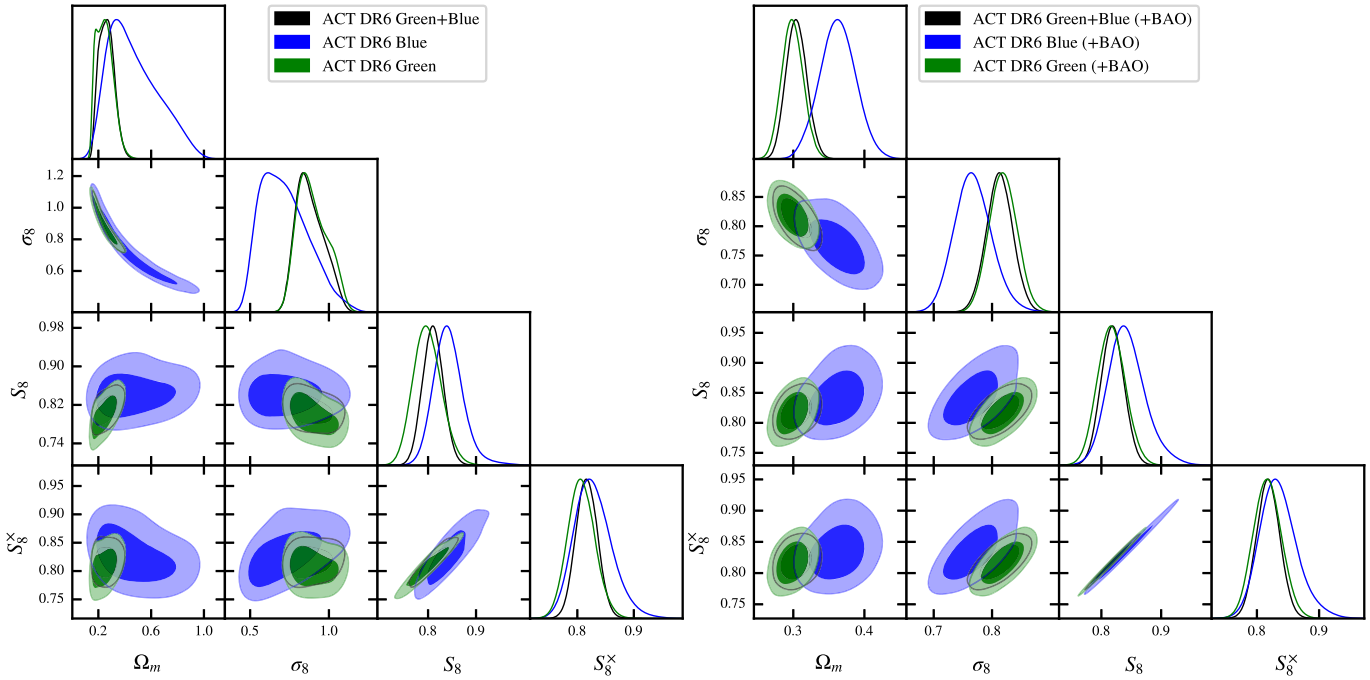

Figure 39. Parameter constraints from the cross-correlation of ACT DR6 lensing and unWISE galaxies using the priors from Qu et al. (2024; see Table 8). The posteriors on Ω_m and σ_8 are significantly more non-Gaussian with this choice of priors compared to our baseline priors (Table 2). The best-constrained parameters S_8 and $S_8^\times$ are not strongly affected by this choice of priors, however. We find $S_8 = 0.810 \pm 0.021$ from the combination of C_ℓ^{gg} and $C_\ell^{\kappa g}$ for both samples of unWISE galaxies (left). Adding BAO data (right) yields $\sigma_8 = 0.812 \pm 0.023$, a slightly more significant degradation of constraining power compared to our baseline.

Table 9
Summary of the Constraints on Cosmological Parameters Obtained from the Cross-correlation of unWISE Galaxies with ACT DR6 Lensing Reconstruction Using the Priors from Qu et al. (2024; see Table 2)

	Ω_m	σ_8	S_8	$S_8^\times$
		ACT DR6 × unWISE only		
Blue	$0.47^{+0.12}_{-0.24}$	$0.72^{+0.10}_{-0.19}$	$0.843^{+0.026}_{-0.033}$	$0.828^{+0.028}_{-0.037}$
Green	$0.249^{+0.044}_{-0.082}$	$0.896^{+0.074}_{-0.12}$	$0.799^{+0.027}_{-0.031}$	0.807 ± 0.024
Joint	$0.261^{+0.049}_{-0.066}$	$0.882^{+0.069}_{-0.11}$	0.810 ± 0.021	0.817 ± 0.019
		ACT DR6 × unWISE + BAO		
Blue	0.363 ± 0.025	$0.768^{+0.029}_{-0.034}$	$0.843^{+0.026}_{-0.034}$	$0.835^{+0.025}_{-0.033}$
Green	0.299 ± 0.015	0.819 ± 0.024	0.817 ± 0.023	0.817 ± 0.023
Joint	0.305 ± 0.014	0.813 ± 0.022	0.819 ± 0.019	0.818 ± 0.019

Note. It should be compared to Table 3. The constraining power on the best-constrained parameters S_8 and $S_8^\times$ is similar to our baseline analysis, but the addition of BAO proves less powerful in constraining σ_8 with these alternative priors.

Appendix H
Consistency Test of Galaxy–Galaxy Cross-spectrum

As a further consistency test, we compare the prediction for the cross-correlation between the Blue and Green samples of unWISE galaxies obtained from the model inference we presented in Section 9.5 with the observed cross-spectrum. This cross-spectrum contains potentially valuable information to constrain the magnification bias (particularly for the Green sample, where the magnification kernel entirely overlaps with the Blue sample) and the high-redshift tail of the Blue sample. Nevertheless, we chose to neglect this information in the model fit since the ratio of potential systematic contamination to signal is less favorable as compared to the autospectrum. While the signal is approximately a factor of 1.5–2.5 smaller than the autocorrelation of the galaxy samples, observational systematics are expected to be of the same order as in the autocorrelation since they are likely common between both samples. We never performed any null or consistency test on the cross-spectrum and hence do not use it for cosmology analysis.

Here we present a comparison of the model we constrain in Section 9.5 to the observed cross-spectrum as a consistency test (see Figure 40). We find that the observed cross-spectrum is consistent with the posterior predictive distribution of the galaxy–galaxy cross-spectrum conditioned on the autospectra of both galaxy samples and their cross-spectra with the ACT DR6 lensing reconstruction. This test that accounts for the data and model uncertainties yields a PTE of 0.18. To compute the posterior predictive distribution, we sample 500 random points from the posterior of the joint fit to the Green and Blue auto- and cross-correlations (including BAO information; shown as gray lines in Figure 40). To compute the χ^2, we add the covariance of these 500 model predictions (which has significant off-diagonal

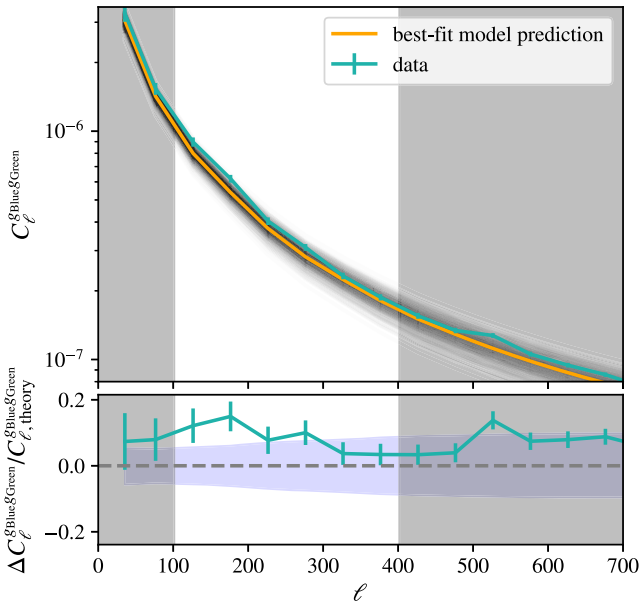

Figure 40. The cross-correlation between the Blue and Green samples of galaxies is consistent with the posterior predictive distribution of our model prediction from a joint fit to the Blue and Green samples from Section 9.5. The gray lines show the spread in model predictions consistent with the posterior of the model fit. The best-fit prediction is shown in orange, with the measured cross-spectrum shown in Blue. The gray bands indicate the range of scales not used for cosmological analysis. In the lower panel, we show the fractional residuals between the best-fit model prediction and the measured cross-spectrum. The blue band shows the 1σ posterior on the model prediction. Note, that the amplitudes of different scales within the model posterior are significantly correlated.

components) to an analytical approximation of the data covariance and compute the residual as the difference between the observed cross-spectrum and the best-fit model prediction.

Appendix I
Reanalysis of the Cross-correlation of Planck Lensing and unWISE

In this paper, we present an analysis pipeline for the cross-correlation between CMB lensing reconstruction from ACT and unWISE galaxies. In the subsequent sections, we discuss

Table 10
Various Improvements to the Previous Analysis of the Cross-correlation between Planck Lensing and unWISE Galaxies

	Impact on S_8
Monte Carlo lensing norm correction	$+0.6\sigma$
Modeling improvements	-0.5σ
Systematics weighting	$+0.4\sigma$
Additional spectroscopic data	$+0.8\sigma$
Use of Planck PR4 lensing reconstruction	$+0.2\sigma$
PCA-based dN/dz marginalization	$-0.2\sigma + \sim$15% wider posteriors
fid. cosmo. correction	Change in degeneracy directions
Total	$+1.3\sigma + \sim$15% wider posteriors

Note. This includes the exploitation of updated and additional data such as the PR4 lensing reconstruction from Planck and additional spectroscopic data from eBOSS to constrain the sample redshifts. Additionally, we include systematics weighting for the unWISE galaxies, improvements to the modeling, and the Monte Carlo lensing norm correction for the Planck lensing map. Here we summarize the impact of these improvements.

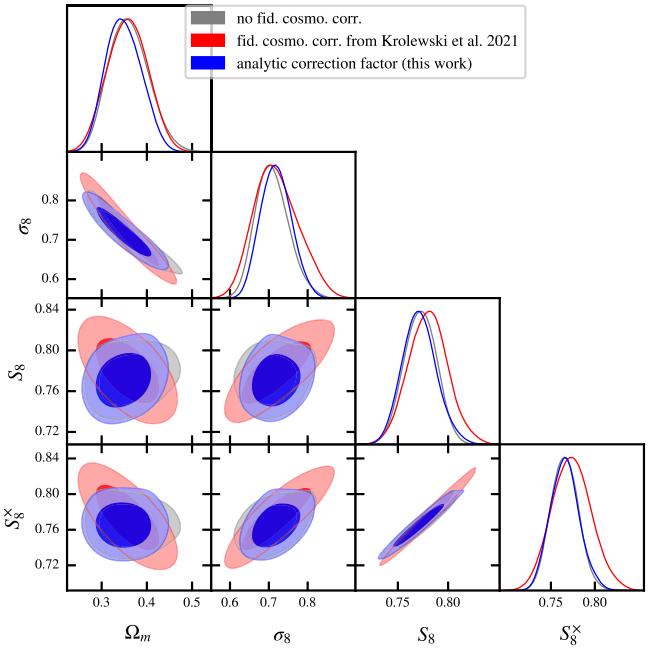

Figure 41. Comparison of three methods for the fiducial cosmology correction on the Blue sample in Planck × unWISE. Replacing the approximate fiducial cosmology correction in Krolewski et al. (2021) with the expressions in Appendix C.1, rotates the S_8–Ω_m contours.

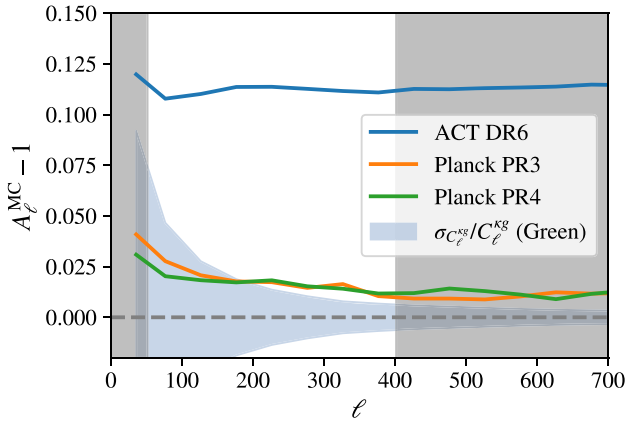

Figure 42. Shown here are the Monte Carlo norm corrections for the cross-correlation of the unWISE galaxies with the Planck PR4 (Carron et al. 2022) and PR3 (Planck Collaboration et al. 2020b) lensing reconstructions. We also show the equivalent norm correction for the ACT DR6 lensing reconstruction used in this work. That correction is much larger, due to the application of Fourier space masking prior to lensing reconstruction that aims to reduce contamination from instrumental effects such as ground pickup and features in the scan strategy. Moreover, we show the fractional 1σ errors on our $C_\ell^{\kappa g}$ (here shown for the Green galaxy sample) for comparison.

the differences in the previous analysis of the cross-correlation between Planck lensing and unWISE presented by Krolewski et al. (2021; with spectra and redshift distributions measured in Krolewski et al. 2020). In Appendix I.3, we also show a reanalysis of the cross-correlation with Planck based on the newest available lensing reconstruction (Carron et al. 2022).

I.1. Summary of the Changes to the Analysis

In Section 8.1, we outlined the improvements we made to the model that was used for the analysis of the cross-correlation of Planck PR3 lensing (Planck Collaboration et al. 2020b) with the unWISE galaxies presented in Krolewski et al. (2020). This

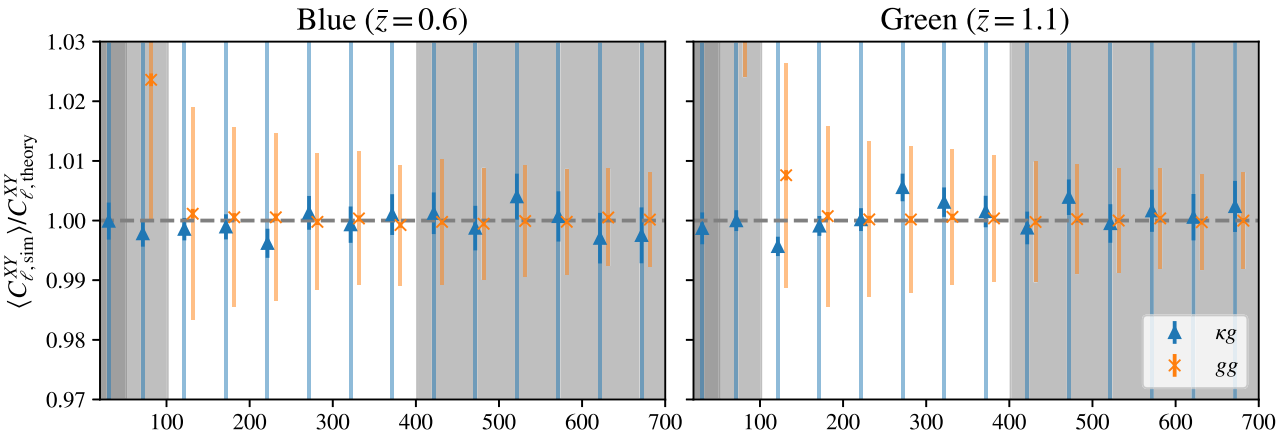

Figure 43. As with ACT, we recover the input C_ℓ^{gg} and $C_\ell^{\kappa g}$ on Planck simulations to better than 1% on all scales. The lightly colored error bars indicate our measurement errors, while the dark error bars show the error on the mean of 480 Gaussian simulations.

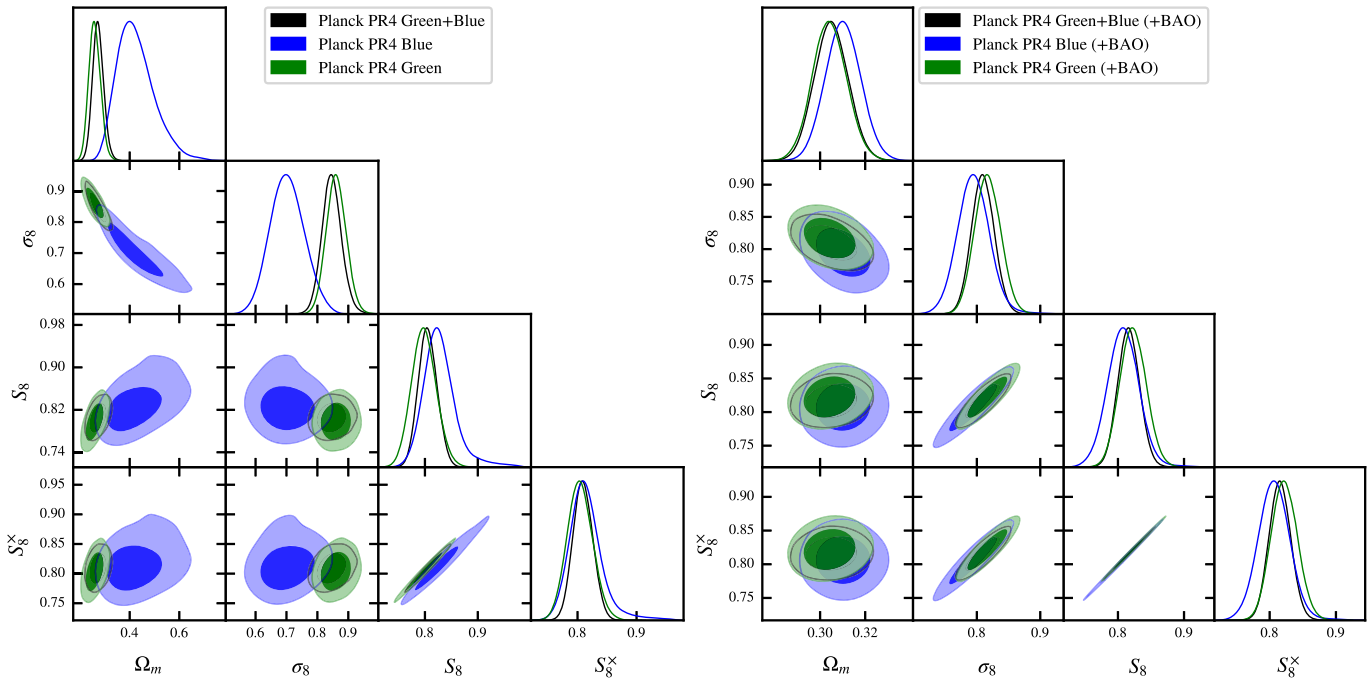

Figure 44. Updated parameter constraints from the cross-correlation of Planck lensing and unWISE galaxies. From the combination of C_ℓ^{gg} and $C_\ell^{\kappa g}$ only for both samples of unWISE galaxies (left), we find $S_8 = 0.805 \pm 0.018$. With additional information from BAO (right), we obtain $\sigma_8 = 0.810 \pm 0.018$.

Table 11
Summary of the One-dimensional Marginalized Posteriors on the Key Cosmological Parameters from Our Reanalysis of the Cross-correlation between unWISE Galaxies and the Planck Lensing Reconstructions

	Ω_m		σ_8		S_8		$S_8^\times$	
				Planck PR4 × unWISE only				
Blue	$0.425^{+0.054}_{-0.088}$	(0.390)	$0.703^{+0.052}_{-0.059}$	(0.714)	$0.828^{+0.022}_{-0.033}$	(0.814)	$0.815^{+0.021}_{-0.030}$	(0.804)
Green	$0.259^{+0.022}_{-0.025}$	(0.250)	0.861 ± 0.032	(0.865)	0.798 ± 0.023	(0.790)	0.804 ± 0.022	(0.797)
Joint	$0.273^{+0.020}_{-0.024}$	(0.279)	0.846 ± 0.032	(0.836)	0.805 ± 0.018	(0.807)	0.809 ± 0.017	(0.810)
				Planck PR4 × unWISE + BAO				
Blue	0.3102 ± 0.0078	(0.311)	0.795 ± 0.026	(0.793)	0.808 ± 0.025	(0.808)	0.807 ± 0.025	(0.806)
Green	0.3042 ± 0.0077	(0.304)	0.817 ± 0.021	(0.814)	0.823 ± 0.020	(0.820)	0.822 ± 0.020	(0.820)
Joint	0.3050 ± 0.0075	(0.305)	0.810 ± 0.018	(0.808)	0.816 ± 0.017	(0.816)	0.816 ± 0.016	(0.815)

Note. We use the newest Planck PR4 lensing maps (Carron et al. 2022) and our improved model detailed in this paper. We provide best-fit values in parentheses following the marginalized constraints.

includes marginalization over higher-order biases, improved marginalization over redshift uncertainties, and a different treatment of the fiducial cosmology dependence of the cross-correlation redshift estimates. Additionally, we have also introduced systematics weighting for the unWISE samples (see Section 3.1.3), and we outline in Section 3.1.2 (with details provided in Appendix K) the additional data that are available to improve the cross-correlation redshift estimates for the unWISE samples. New and improved data are also available on the Planck lensing side with the improved PR4 release (Carron et al. 2022), briefly described in Section 3.3. Finally, it was noticed that previous cross-correlation work had neglected to include a Monte Carlo correction that is required to achieve the correct normalization of the lensing reconstruction; we briefly discuss this aspect in more detail in the subsequent section.

The impact of the various changes and improvements is summarized in Table 10. The Monte Carlo lensing norm correction is described in Appendix I.2 below, and the modeling improvements are described in Section 8. The change in spectra from applying systematics weighting is shown in Figure 47. The most significant driver of the change in S_8 is the shift toward higher $C_\ell^{\kappa g}$ for the Blue sample when applying the weights, while C_ℓ^{gg} is largely unchanged. In contrast, for the Green sample, both $C_\ell^{\kappa g}$ and C_ℓ^{gg} increase, leading to a smaller change in S_8. The change in redshift distribution is shown in Figure 52; the impact on parameters is dominated by the Blue sample, where the redshift distribution changes much more (0.74σ) than for the Green sample (0.14σ). When adding the new data to the cross-correlation redshifts, the Blue sample shifts to a lower redshift. At fixed parameters, this increases C_ℓ^{gg} (due to the larger amplitude of structure at low redshift), while decreasing $C_\ell^{\kappa g}$ (due to the smaller overlap with the lensing kernel). To fit to the fixed data vector, the parameters must change in the opposite direction, leading to a higher S_8. The Green sample shifts to slightly higher redshift, although the dominant change is likely from the narrower width of the new dN/dz, which increases C_ℓ^{gg} more than $C_\ell^{\kappa g}$ at fixed parameters, which likewise leads to a smaller upward shift in S_8. The new redshift marginalization is described in Section 8.2. Finally, in Figure 41, we show the impact of switching the approximate fiducial cosmology correction from Krolewski et al. (2021) to the formalism described in Appendix C.1. The impact is mostly a change in the direction of the S_8–Ω_m degeneracy.

I.2. Lensing Monte Carlo Norm Correction

A well-known effect in CMB lensing reconstruction is a misnormalization of the lensing reconstruction resulting from performing lensing reconstruction in the presence of a mask (see N. Sailer et al. 2023, in preparation, for a pedagogical discussion of this effect and Benoit-Levy et al. 2013 or Carron 2023 for a more technical discussion). Typically CMB lensing autospectrum analyses have computed Monte Carlo corrections for this effect using Gaussian simulations (Planck Collaboration et al. 2020b; Carron et al. 2022; Qu et al. 2024). The normalization correction is obtained as the ratio of the cross-correlation between appropriately masked input lensing convergence with the lensing reconstruction to the autocorrelation of the known input convergence. For the case of the cross-correlation, this implies

$$A_\ell^{\rm MC} = \frac{C_\ell^{\kappa_{{\rm in},\kappa-{\rm mask}}\kappa_{{\rm in,g-mask}}}}{C_\ell^{\hat{\kappa}\kappa_{{\rm in,g-mask}}}}. \tag{I1}$$

Here $\hat{\kappa}$ is the masked CMB lensing reconstruction, $\kappa_{{\rm in},\kappa-{\rm mask}}$ is the input lensing convergence masked with the lensing mask, and $\kappa_{{\rm in},g-{\rm mask}}$ is the input lensing convergence masked using the galaxy mask. As one can see here, the correction in principle depends on the region of overlap and thus cannot be universally computed, though we find in practice that the footprint dependence is small (<1%). An unbiased estimate of the CMB lensing cross-correlation can then be obtained as

$$C_\ell^{\hat{\kappa}_{\rm MC}g} = C_\ell^{\hat{\kappa}g} A_\ell^{\rm MC}. \tag{I2}$$

We compute $A_\ell^{\rm MC}$ using 480 Gaussian simulations and corresponding lensing reconstructions provided by Carron et al. (2022). We find that on the scales of interest for our analysis, the norm correction results in a nearly scale-invariant increase in the amplitude of $C_\ell^{\kappa g}$ by around 2% (see Figure 42). We note that Krolewski et al. (2021) used the Planck PR3 lensing reconstruction (Planck Collaboration et al. 2020b), which also exhibits very similar behavior (see Figure 42). Given the error bars on our cross-correlation measurement, accounting for this effect is unavoidable and leads to a $\sim 0.6\sigma$ increase in the inferred value of S_8 (see Table 10).

We perform the same test of unbiased power spectrum recovery shown for ACT in Section 5 for Planck and find recovery to within 1% after application of the norm correction (see Figure 43).

I.3. Updated Cosmological Constraints from the Cross-correlation of Planck Lensing and unWISE

With the improvements laid out above, we perform a reanalysis of the cross-correlation of Planck lensing and unWISE galaxies. We adopt the priors and scale cuts consistent with our ACT analysis and estimate the covariance as described in Section 6. We find $S_8 = 0.805 \pm 0.018$ from the combination of $C_\ell^{\kappa g}$ and C_ℓ^{gg} alone and $\sigma_8 = 0.810 \pm 0.018$ when adding BAO information. The parameter constraints from the reanalysis of the cross-correlation between Planck lensing and unWISE are summarized in Table 11, with posterior distributions shown in Figure 44.

Appendix J
Impact of Galaxy Systematics Weighting

Figures 45 and 46 show the correlation of the unWISE number counts with various systematic tracers discussed in Section 3.1.3 before and after correction for the trends with stellar density and W2 limiting magnitude (corrected correlations are shown as red lines in the relevant panels).

In this work, we include systematics weights, which had not been applied previously, but we also no longer filter out the low-ℓ ($\ell < 20$) modes in the unWISE map (in contrast to what was done in Krolewski et al. 2020, 2021). The large-scale filtering has a similar effect to systematics weighting, also reducing large-scale power by removing correlations between systematics and the true galaxy density. However, removing large scales in harmonic space complicates the use of the MASTER algorithm Hivon et al. (2002) to obtain unbiased band powers through mode decoupling. Hence, we no longer adopt this method. Nevertheless, the net effect of replacing the low-ℓ filtering with the angular systematics weights is at most 0.5% (Figure 47).

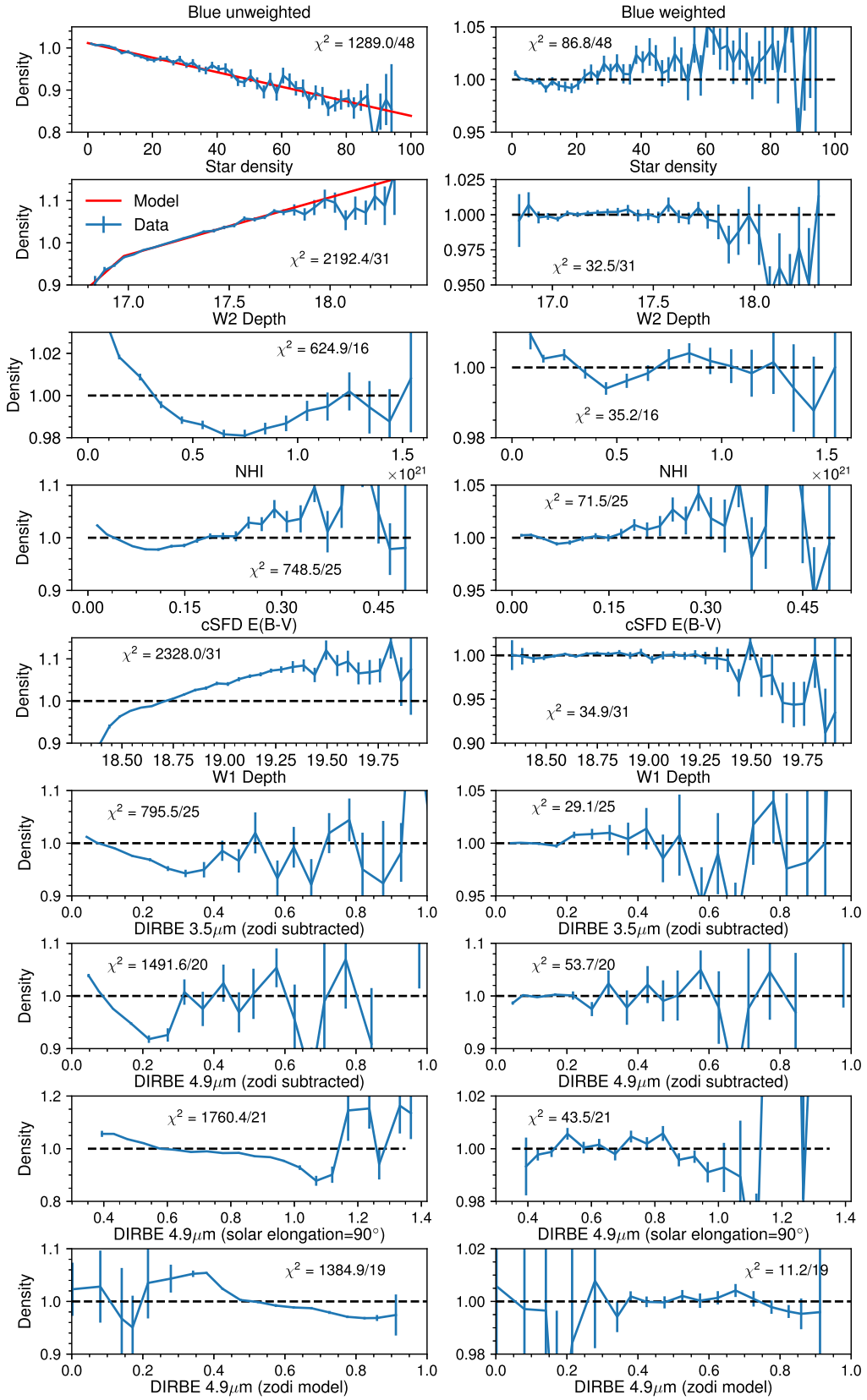

Figure 45. We show here the correlations of the unWISE number density from the Blue sample with the imaging systematics templates discussed in Section 3.1.3. Prior to applying any corrections, the number density is significantly correlated with all templates. All correlations are reduced dramatically after applying corrections for the correlation with W2 depth and stellar density. Because many of the templates are correlated the improvement also extends to those templates for which we did not explicitly correct. To guard against overfitting and because the residual impact on the scales of interest is small we do not correct for further contamination even though some of the correlations are still significant even after the correction.

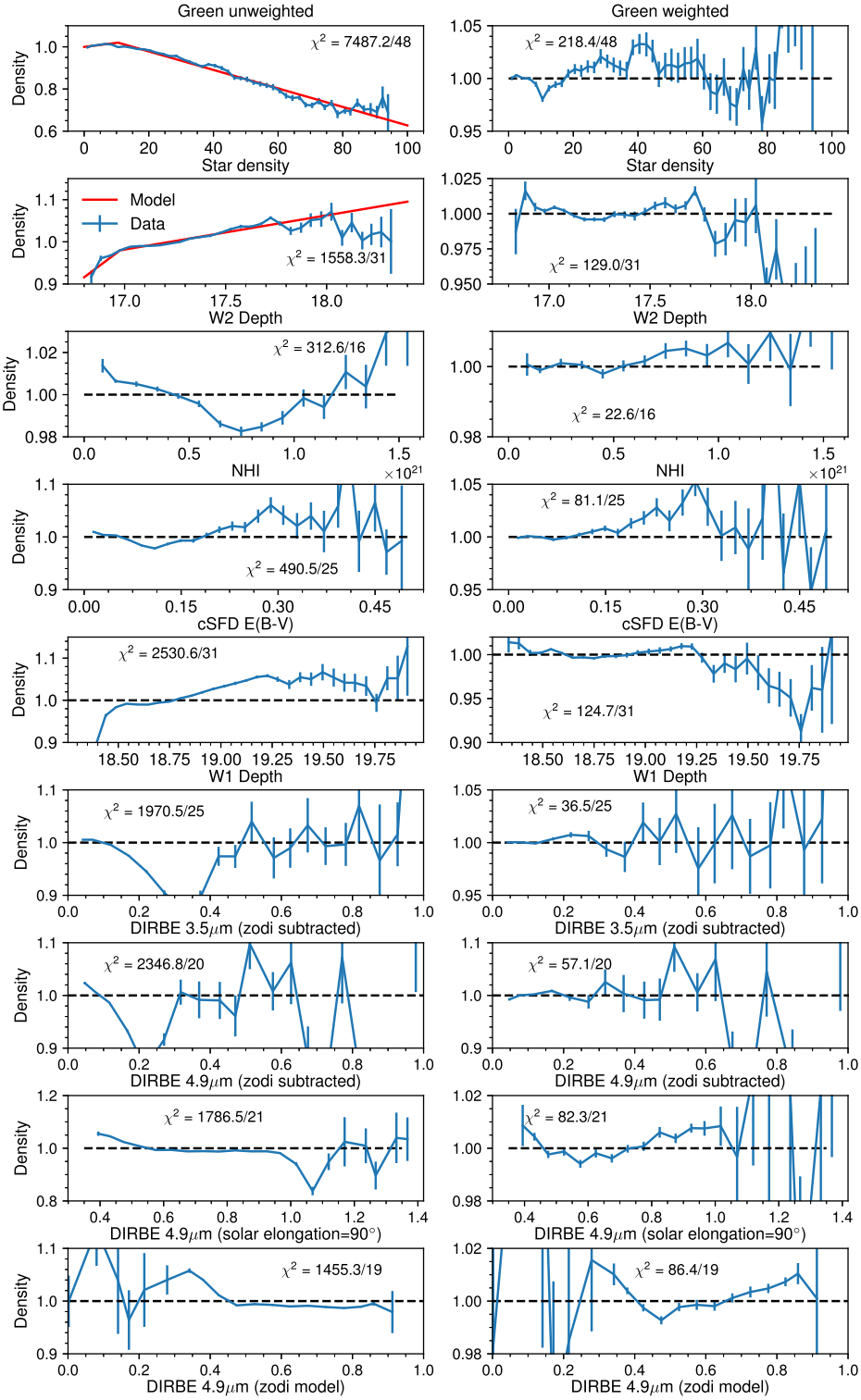

Figure 46. Similar to Figure 45 but shown here for the Green sample of unWISE galaxies. As with the Blue sample, we correct the data for correlations with W2 depth and stellar density, improving the correlations with all of the imaging templates used.

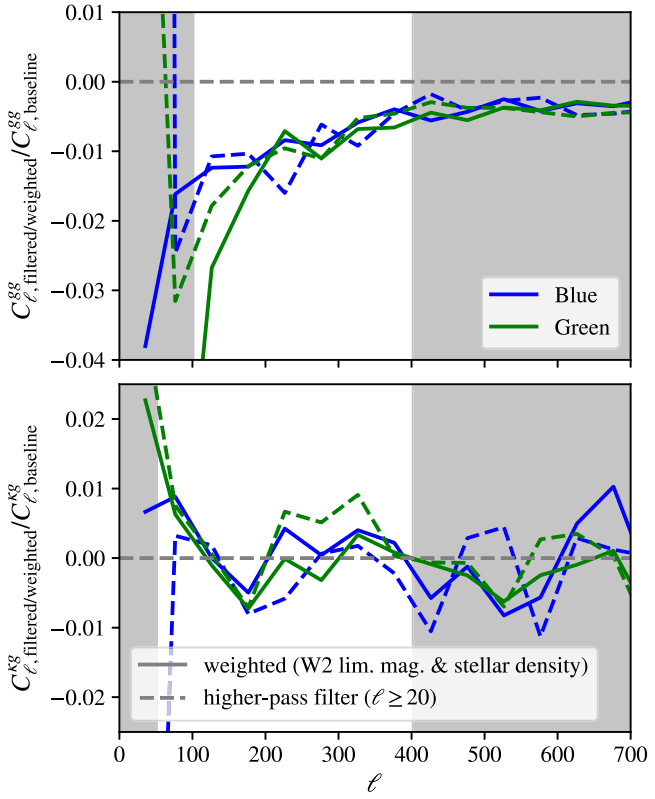

Figure 47. Ratio of galaxy–galaxy and galaxy-CMB lensing spectra after weighting against W2 5σ limiting magnitude and Gaia stellar density (as described in Section 3.1.3) to the same spectra without such weighting. The correction for these observational effects reduces the power in the autocorrelation by up to 3% on large scales, while it does not significantly impact the measured cross-correlation spectra. We also show for comparison the spectra used in Krolewski et al. (2020, 2021); these filtered our large scales ($\ell < 20$) in harmonic space as an alternative method for mitigating such observational effects. The difference between the spectra using the two methods is about 0.5%. In this comparison, we have corrected for the simulation-derived transfer function described in Section 5.

Appendix K
Spectroscopic Samples Used in Cross-correlation Redshifts

We follow the methodology described in Section 5.4 of Krolewski et al. (2020) with updated spectroscopic galaxy samples and revised magnification bias measurements for the spectroscopic samples. We split the spectroscopic samples into the NGC and SGC regions, allowing for different spectroscopic biases between the hemispheres (Alam et al. 2017; Ross et al. 2017) and to test their consistency. We summarize the spectroscopic samples used in Table 12 and Figures 48 and 49.

We use both unWISE and spectroscopic sample sytematics weights in computing the Davis–Peebles (Davis & Peebles 1983) estimator for $\bar{w}_{\mathrm{sp}}(\theta)$. The unWISE weights are described in Section 3.1.3 above, and the spectroscopic sample weights are the standard systematic weights for BOSS and eBOSS (Eftekharzadeh et al. 2015; Reid et al. 2016).

The eBOSS LRGs are targeted at a lower priority than eBOSS quasars. Unlike BOSS, which used multiple passes to eventually reach lower-priority objects, eBOSS did not have enough passes to reach lower-priority objects within the fiber radius of higher-priority objects. Therefore, no LRGs were observed within the fiber scale (62″) of any quasar target. This poses a problem for comparing LRG-unWISE and quasar-unWISE cross-correlations in the region where both spectroscopic tracers overlap ($0.8 < z < 1.0$) since the LRGs and quasars will be anticorrelated on small scales due to fiber collisions. We, therefore, remove any unWISE galaxies and randoms within 62″ of an eBOSS quasar target, as these unWISE galaxies will also be anticorrelated with the eBOSS LRGs due to their positions near the quasars.

Table 12
Properties of the Spectroscopic Samples Used for Cross-correlation Redshifts

Sample	z_{min}	z_{max}	N	Jackknife Regions	Area (deg^2)
LOWZ NGC	0.0	0.5	273547	34	5661
LOWZ SGC	0.0	0.5	120585	13	2393
CMASS NGC	0.1	0.8	544308	37	6676
CMASS SGC	0.1	0.8	193899	13	2427
eBOSS DR16 LRG NGC	0.6	1.0	107500	63	2898
eBOSS DR16 LRG SGC	0.6	1.0	67316	38	1812
eBOSS DR16 QSO NGC	0.8	2.2	218209	61	2927
eBOSS DR16 QSO SGC	0.8	2.2	125499	38	1825
BOSS DR12 QSO NGC	2.0	4.0	69204	36	6569
BOSS DR12 QSO SGC	2.0	4.0	16590	12	2176

Note. Areas are defined using the overlap of the spectroscopic survey mask and the unWISE mask.

We revise the magnification bias measurements presented in Appendix C of Krolewski et al. (2020) and update them for the eBOSS LRGs. Magnification bias of the spectroscopic samples can create spurious correlations between widely separately photometric and spectroscopic redshift bins, thus biasing the clustering dN/dz in the tails; the spectroscopic magnification bias is relevant when the spectroscopic sample lies at a higher redshift than the photometric sample.

First, Krolewski et al. (2020) did not correctly consider the impact of magnification bias on fixed-aperture flux measurements. Lensing magnification preserves surface brightness, brightening galaxies by making them larger on the sky. The impact of magnification on a fixed-aperture flux measurement therefore depends on the light profile: if it is spatially constant, then magnification has no effect, but in the more realistic case where it rises toward the galaxy's center, lensing magnification will brighten the galaxy, but not by as much as if the aperture contained all of the galaxy's light. CMASS and LOWZ use four different measurements of magnitude: model magnitudes, consisting of the best-fit exponential or de Vaucoleurs profile; cmodel magnitudes, a linear combination of the exponential and de Vaucoleurs profiles; point-spread function (PSF) magnitudes, which fit a PSF model to the source and therefore only consider flux within the PSF solid angle; and fib2 magnitudes, which only count flux within the 2″ fibers. We approximate the model and cmodel magnitudes as measuring the full galaxy flux (therefore being maximally affected by lensing magnification). For PSF magnitudes and fib2 magnitudes, we magnify the galaxy profile (assuming an isotropic linear combination of de Vaucoleurs and exponential profiles with effective radius given in the catalog) and truncate the fluxes at either 2″ or the mean PSF size in a given band (1.″32 in r, 1.″26 in i, 1.″29 in z).

Second, in a spectroscopic survey, lensing magnification affects the redshift success rate, the probability with which a redshift can be estimated from an observed spectrum, which is lower for fainter galaxies. LOWZ galaxies are sufficiently bright that redshift failures and successes have very similar

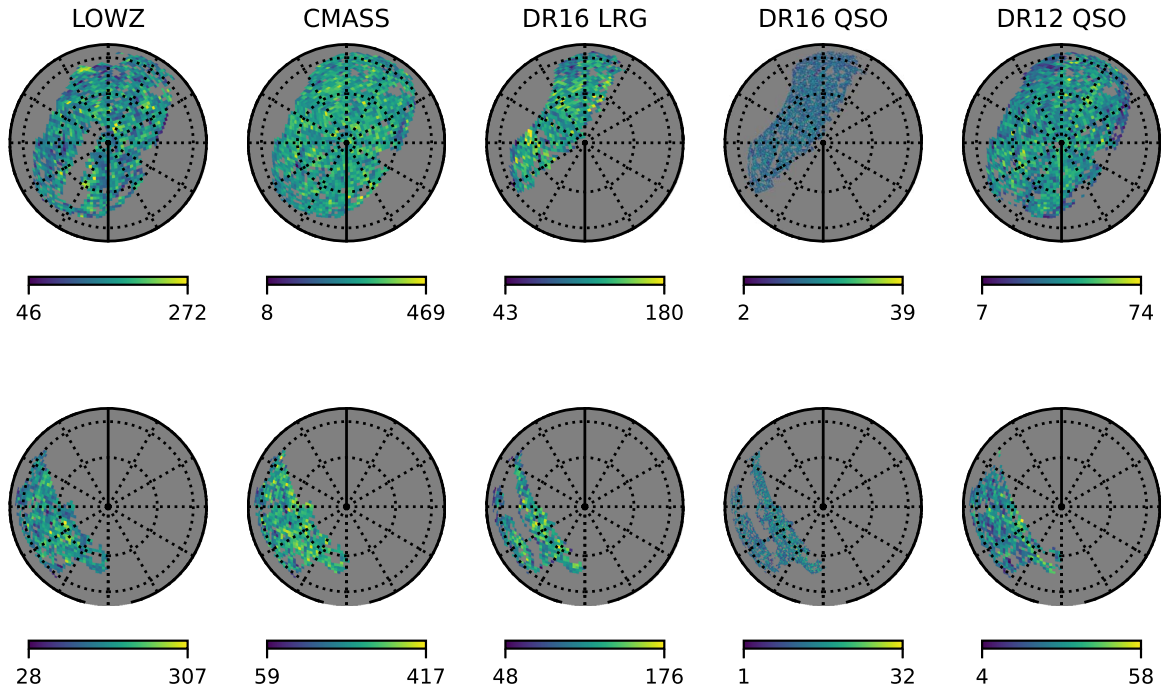

Figure 48. Maps of the spectroscopic samples used to determine $b(z)dN/dz$ of the unWISE galaxies. The top row shows NGC and the bottom row SGC. Together the spectroscopic samples cover a representative subset of the unWISE footprint (as can also be seen in Figure 50).

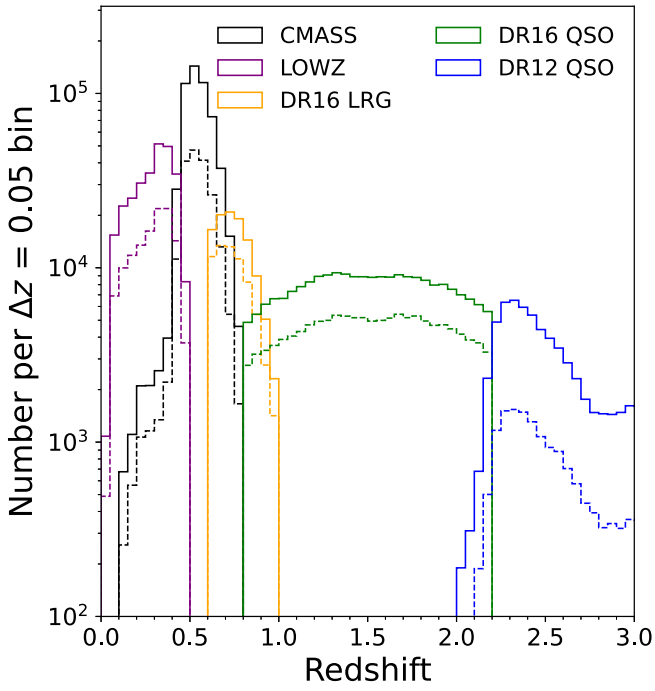

Figure 49. Here we show the redshift distribution of spectroscopic samples used to measure the cross-correlation redshifts for the unWISE samples (NGC and SGC are shown as solid and dashed lines, respectively). The spectroscopic tracers used in this work span the full redshift range of the unWISE samples up to $z \sim 3$.

magnitude distributions (Figure 7 in Reid et al. 2016), i.e., the faintest LOWZ galaxies are considerably brighter than the *limiting magnitude* of the spectrograph and therefore increasing or decreasing their flux by a small amount will not change the success rate. CMASS galaxies are fainter, and we estimate from Figure 7 in Reid et al. (2016) that $\frac{d\ln N}{di_{\rm fib2}} = 0.32$, due to the change in the redshift success rate (by differencing the $i_{\rm fib2}$ distribution at the faint end of CMASS galaxies, comparing $i_{\rm fib2} = 21.3$ and 21.4). Since $i_{\rm fib2}$ has a fixed aperture, we further correct for its reduced sensitivity to lensing magnification compared to total magnitudes. For eBOSS LRGs, we also correct for changes in redshift success rate using the measurement of redshift success against the spectral S/N in Figure 5 of Ross et al. (2020). We translate the S/N to magnitudes assuming background-limited sources and account for the finite aperture (fiber size) in which the spectral S/N is measured. For eBOSS quasars, we rerun the XDQSO quasar probability code to measure the response of the quasar selection to small magnifications (the change in the redshift success rate with magnitude is negligible; see Figure 4 of Ross et al. 2020). We also account for the reduced efficiency of star/galaxy separation at fainter magnitudes due to magnification (where a point source can be demagnified and then spuriously considered an extended source; Strauss et al. 2002).[72]

Third, we correctly account for the impact of lensing magnification at both the bright and faint ends of the sample (i.e., if the sample has a bright cut, demagnified objects near the threshold are more likely to constitute the sample). This particularly matters for the eBOSS LRGs, which have a bright cut to prevent overlap with BOSS CMASS. We follow the method of Elvin-Poole et al. (2023) and Samuroff et al. (2023), in which the change in number counts is computed both when magnifying and demagnifying the galaxies, and the total change is the difference between the two: $\delta N = \delta N_+ - \delta N_-$. We use a small finite step size of $\delta m = 0.02$ to compute magnification biases.

Magnification bias measurements are shown in Tables 13 and 14. These results are reasonably consistent with external estimates: von Wietersheim-Kramsta et al. (2021) find $s = 0.77$ for LOWZ at $z = 0.35$ and $s = 1.05$ for CMASS at

[72] https://classic.sdss.org/dr7/products/general/stargalsep.html

Table 13
Summary of the Effective Redshifts for the Spectroscopic Autocorrelation, $z_{\rm eff,ss}$, and the Cross-correlation with the Green unWISE Sample $z_{\rm eff,sp}$

		LOWZ					CMASS					eBOSS DR16 LRG				
$z_{\rm min}$	$z_{\rm max}$	$z_{\rm eff,ss}$	$z_{\rm eff,sp}$	s	$b_{\rm NGC}$	$b_{\rm SGC}$	$z_{\rm eff,ss}$	$z_{\rm eff,sp}$	s	$b_{\rm NGC}$	$b_{\rm SGC}$	$z_{\rm eff,ss}$	$z_{\rm eff,sp}$	s	$b_{\rm NGC}$	$b_{\rm SGC}$
0.00	0.05	0.042	⋯	1.975	1.326	1.244	⋯	⋯	⋯	⋯	⋯	⋯	⋯	⋯	⋯	⋯
0.05	0.10	0.079	0.070	1.069	1.368	1.305	⋯	⋯	⋯	⋯	⋯	⋯	⋯	⋯	⋯	⋯
0.10	0.15	0.124	0.123	0.912	1.518	1.491	⋯	⋯	⋯	⋯	⋯	⋯	⋯	⋯	⋯	⋯
0.15	0.20	0.175	0.175	1.049	1.683	1.682	0.179	0.177	0.756	3.078	1.735	⋯	⋯	⋯	⋯	⋯
0.20	0.25	0.225	0.223	1.015	1.892	1.755	0.226	0.223	0.663	1.204	1.448	⋯	⋯	⋯	⋯	⋯
0.25	0.30	0.276	0.273	0.972	1.978	2.051	0.276	0.273	0.982	1.775	1.650	⋯	⋯	⋯	⋯	⋯
0.30	0.35	0.327	0.325	0.923	1.984	2.062	0.324	0.323	1.121	1.765	1.798	⋯	⋯	⋯	⋯	⋯
0.35	0.40	0.372	0.369	1.014	2.051	2.077	0.382	0.371	1.161	2.273	2.078	⋯	⋯	⋯	⋯	⋯
0.40	0.45	0.420	0.419	1.179	2.211	2.109	0.439	0.429	0.972	2.055	2.048	⋯	⋯	⋯	⋯	⋯
0.45	0.50	0.460	0.463	1.511	2.541	2.187	0.479	0.475	0.937	2.065	2.000	⋯	⋯	⋯	⋯	⋯
0.50	0.55	⋯	⋯	⋯	⋯	⋯	0.524	0.524	1.040	2.034	2.101	⋯	⋯	⋯	⋯	⋯
0.55	0.60	⋯	⋯	⋯	⋯	⋯	0.572	0.573	1.148	2.136	2.073	⋯	⋯	⋯	⋯	⋯
0.60	0.65	⋯	⋯	⋯	⋯	⋯	0.620	0.617	1.352	2.233	2.147	0.627	0.620	0.539	2.137	2.114
0.65	0.70	⋯	⋯	⋯	⋯	⋯	0.669	0.672	1.553	2.400	2.236	0.675	0.675	0.595	2.094	2.107
0.70	0.75	⋯	⋯	⋯	⋯	⋯	0.717	0.715	1.957	2.509	2.434	0.725	0.718	0.721	2.202	2.066
0.75	0.80	⋯	⋯	⋯	⋯	⋯	0.765	0.772	2.239	2.666	2.918	0.773	0.777	0.798	2.363	2.333
0.80	0.85	⋯	⋯	⋯	⋯	⋯	⋯	⋯	⋯	⋯	⋯	0.821	0.825	0.884	2.458	2.514
0.85	0.90	⋯	⋯	⋯	⋯	⋯	⋯	⋯	⋯	⋯	⋯	0.871	0.868	0.890	2.572	2.400
0.90	0.95	⋯	⋯	⋯	⋯	⋯	⋯	⋯	⋯	⋯	⋯	0.919	0.922	0.949	2.517	2.405
0.95	1.00	⋯	⋯	⋯	⋯	⋯	⋯	⋯	⋯	⋯	⋯	0.969	0.971	0.947	2.211	2.382

Note. We also summarize the measured magnification (s) and clustering biases ($b_{\rm NGC}$ and $b_{\rm SGC}$ for the NGC and SGC regions, respectively) for the spectroscopic samples. The effective redshifts and magnification bias are determined from the NGC only, whereas the clustering bias is measured separately for NGC and SGC. Estimates of the magnification biases on the SGC are consistent with the NGC but with increased uncertainties. Therefore, we use the magnification biases measured on the NGC throughout. We allow for a different clustering bias between the hemispheres. We do not report a value for $z_{\rm sp}$ at $z < 0.05$ because there are zero unWISE-Green galaxies matched to COSMOS photometric redshifts in this redshift range.

Table 14
Same as Table 13, but for the Quasar Samples

		eBOSS DR16 QSO					BOSS DR12 QSO		
$z_{\rm min}$	$z_{\rm max}$	$z_{\rm eff,ss}$	$z_{\rm eff,sp}$	s	$b_{\rm NGC}$	$b_{\rm SGC}$	$z_{\rm eff,ss}$	$z_{\rm eff,sp}$	s
0.00	0.20	⋯	⋯	⋯	⋯	⋯	⋯	⋯	⋯
0.20	0.40	⋯	⋯	⋯	⋯	⋯	⋯	⋯	⋯
0.40	0.60	⋯	⋯	⋯	⋯	⋯	⋯	⋯	⋯
0.60	0.80	⋯	⋯	⋯	⋯	⋯	⋯	⋯	⋯
0.80	1.00	0.910	0.910	0.126	1.563	1.840	⋯	⋯	⋯
1.00	1.20	1.107	1.115	0.153	2.062	2.088	⋯	⋯	⋯
1.20	1.40	1.300	1.279	0.151	2.055	2.095	⋯	⋯	⋯
1.40	1.60	1.499	1.482	0.171	2.406	2.398	⋯	⋯	⋯
1.60	1.80	1.699	1.674	0.163	2.315	2.520	⋯	⋯	⋯
1.80	2.00	1.895	1.894	0.180	2.789	3.019	⋯	⋯	⋯
2.00	2.20	2.090	2.059	0.163	3.269	2.928	2.176	2.112	0.494
2.20	2.40	⋯	⋯	⋯	⋯	⋯	2.307	2.302	0.213
2.40	2.60	⋯	⋯	⋯	⋯	⋯	2.481	2.461	0.234
2.60	2.80	⋯	⋯	⋯	⋯	⋯	2.671	2.616	0.387
2.80	3.00	⋯	⋯	⋯	⋯	⋯	2.904	2.820	0.793
3.00	3.20	⋯	⋯	⋯	⋯	⋯	3.095	3.150	0.821
3.20	3.40	⋯	⋯	⋯	⋯	⋯	3.270	⋯	1.047

Note. For the BOSS DR12 QSOs, we do not measure the spectroscopic bias, but rather use the fit from Laurent et al. (2017). We do not report a value for $z_{\rm sp}$ at $3.2 < z < 3.4$ because there are zero unWISE-Green galaxies matched to COSMOS photometric redshifts in this redshift range.

$z = 0.65$; Samuroff et al. (2023) find $s = 0.21$ for CMASS at $z = 0.5$ and $s = 0.81$ for eBOSS LRG at $z = 0.8$, and Leauthaud et al. (2022) find $s \sim 1.2$ at $z = 0.65$. The agreement between these measurements is hindered by differences in the exact samples used (i.e., redshift binning) and methodology adopted (measuring the slope of the luminosity function in a single band, or properly taking into account the complex selection function). During the preparation of this paper, we compared results to those in Wenzl et al. (2024), who also account for the full complexities of the selection function (with some methodological improvements over our results). We find very similar results for the magnification bias of CMASS and LOWZ in redshift bins, agreeing to $\Delta s \sim 0.05$, well within our assumed systematic error of $\Delta s = 0.2$.

For quasars, Wang et al. (2020) find $s \sim 0.1$–0.2 for quasars following the eBOSS quasar luminosity function with an

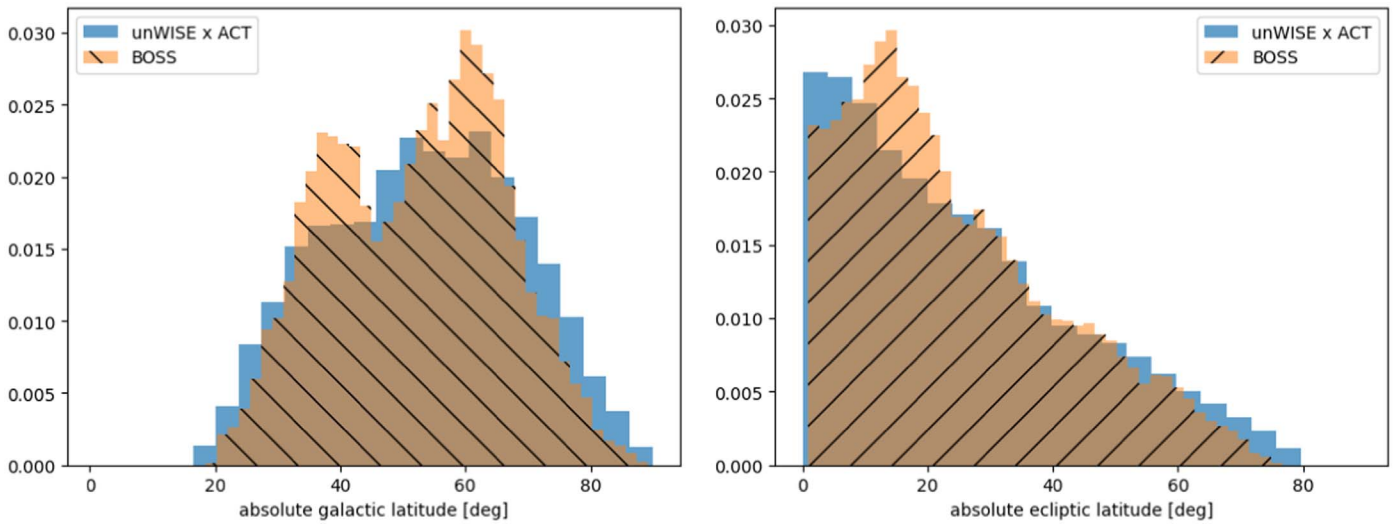

Figure 50. Distribution of the absolute value of ecliptic and Galactic latitude for the ACT-unWISE footprint that we measure C_ℓ^{gg} and $C_\ell^{\kappa g}$ on; and unWISE-BOSS footprint that we use for cross-correlation redshifts. The fact that the unWISE-BOSS footprint is a good match to the ACT-unWISE footprint means that our estimate of $b(z)dN/dz$ from the cross-correlation of unWISE with BOSS is likely to be representative of the bias-weighted redshift distribution on the ACT-unWISE footprint.

absolute magnitude cutoff; Lepori et al. (2020) and Iršič et al. (2016) find $s = 0.295$ for BOSS quasars; Myers et al. (2003, 2005) find $s = 0.29$ for 2dF quasars.

We propagate errors on the magnification bias estimates into our uncertainty on the clustering redshift by assuming that magnification bias errors are dominated by a systematic error of $\Delta s = 0.2$. This is motivated by the level of agreement between our results and past results, and by Elvin-Poole et al. (2023), who find agreement to $\Delta s \sim 0.2$ between the approximate method that we use and more sophisticated methods based on image simulations. We find the magnification bias measurements are consistent between NGC and SGC, so we use NGC measurements, due to their higher density and smaller uncertainties. We assume the magnification bias error is entirely correlated between NGC and SGC for each tracer.

We place the measurement in each bin at its effective redshift rather than the mean redshift of the bin. This is a very minor effect except for the $\Delta z = 0.2$ quasar bins in the tail of the unWISE redshift distribution. We compute the effective redshift for the unWISE cross-correlations as

$$z_{\mathrm{eff,\,sp}} = \frac{\sum_p z_{p,i}\ 1/\chi^2_{p,i}\ dN_s/dz}{\sum_p 1/\chi^2_{p,i}\ dN_s/dz} \tag{K1}$$

and for the spectroscopic autocorrelations as

$$z_{\mathrm{eff,ss}} = \frac{\int dz\ z\ 1/\chi^2 dN_s/dz}{\int dz\ 1/\chi^2 dN_s/dz}. \tag{K2}$$

We can only obtain estimates of the redshifts of individual photometric galaxies, $z_{p,i}$, in the unWISE sample for the small number of objects that have counterparts in the $2\,\mathrm{deg}^2$ COSMOS field. Because the number of objects is small, we cannot reliably estimate a smooth dN_p/dz, and therefore, explicitly write the integral as a sum over the photometric sample in Equation (K1).

With an improved measurement of eBOSS quasar clustering, we switch from using the parameterized form of the quasar bias from Laurent et al. (2017) to our own measurements of the quasar bias from its autocorrelation, similar to the method adopted for CMASS and LOWZ (Figure 6 in Krolewski et al. 2020). We continue to use the Laurent et al. (2017) bias function for the DR12 QSOs, which have a noisier autocorrelation measurement. Our quasar bias measurements are consistent with Laurent et al. (2017) within the error bars, but they allow for deviations from a smooth trend and take advantage of the larger sample size, especially compared to the measurement of Laurent et al. (2017), which uses a preliminary release of eBOSS quasars (DR14). Spectroscopic biases are given in Tables 13 and 14.

Table 15
Consistency of Cross-correlation Estimates of $b(z)dN/dz$ for Different Spectroscopic Tracers

Spec. Sample 1	Spec. Sample 2	Blue χ^2/dof	Green χ^2/dof
DR12 CMASS N	DR12 CMASS S	7.4/14	17.7/14
DR12 CMASS N	DR12 LOWZ N	5.6/7	6.6/7
DR12 CMASS N	DR12 LOWZ S	6.2/7	5.1/7
DR12 CMASS N	DR16 LRG N	3.6/4	2.5/4
DR12 CMASS N	DR16 LRG S	1.4/4	1.2/4
DR12 CMASS S	DR12 LOWZ N	4.9/7	10.3/7
DR12 CMASS S	DR12 LOWZ S	3.7/7	10.7/7
DR12 CMASS S	DR16 LRG N	5.1/4	3.3/4
DR12 CMASS S	DR16 LRG S	3.6/4	1.4/4
DR12 LOWZ N	DR12 LOWZ S	5.7/9	1.7/9
DR16 LRG N	DR16 LRG S	2.9/8	8.5/8
DR16 QSO N	DR16 QSO S	10.2/7	7.4/7
DR16 QSO N	DR12 QSO N	⋯	3.0/1
DR16 QSO N	DR12 QSO S	⋯	1.5/1
DR16 QSO S	DR12 QSO N	⋯	0.0/1
DR16 QSO S	DR12 QSO S	⋯	2.7/1
DR12 QSO N	DR12 QSO S	⋯	11.3/8

Note. We show the χ^2 between the clustering redshift estimates obtained using different spectroscopic subsamples and the number of degrees of freedom, i.e., the number of overlapping redshift bins between the samples. The Blue sample of unWISE galaxies has no significant overlap with the high-redshift BOSS DR12 quasars (compare Figure 49).

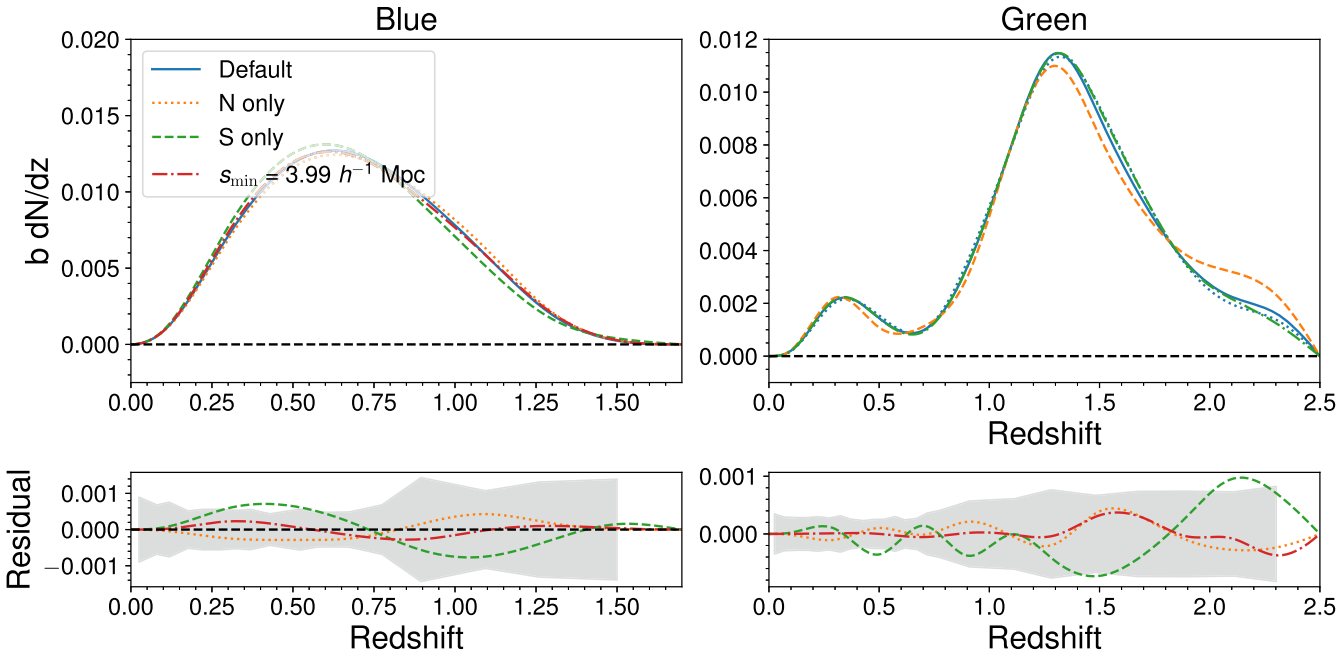

Figure 51. Comparison of $b(z)dN/dz$ used for different null tests: NGC only, SGC only, and increasing the minimum scale used in the clustering redshifts, with the residual (changed $b(z)dN/dz$ minus default) shown in bottom panels. The gray error band shows the uncertainties on the data points used to fit the default $b(z)dN/dz$. The estimates are consistent within the uncertainties, and we show in Section 9.7 that our cosmological inference is stable with respect to these choices.

As in Krolewski et al. (2020), we verify that our cross-correlation redshifts are consistent between different spectroscopic tracers and between hemispheres. We find good agreement ($p > 0.05$) for all overlapping tracers with the same redshift binning ($\Delta z = 0.05$ for galaxies and $\Delta z = 0.20$ for quasars; see Table 15). Furthermore, since the eBOSS LRGs overlap with the eBOSS quasars in the redshift range of $0.8 < z < 1.0$, we have an additional consistency check. We find that for both the Blue and Green unWISE samples, the quasar cross-correlation is slightly higher than the LRG cross-correlation (see Figure 52). To quantitatively compare the two, we create both a $\Delta z = 0.2$ bin for the LRGs and a $\Delta z = 0.05$ bin for the quasars. For Blue, in the single $\Delta z = 0.2$ bin, the quasars are higher by 1.77σ. In the four $\Delta z = 0.05$ bins, the quasars are higher by 1.25σ, 0.77σ, 2.35σ, and 1.65σ. For Green, in a single $\Delta z = 0.2$ bin, the quasars are higher by 1.06σ. Therefore, while a discrepancy certainly exists (especially for Blue), it is not large enough to be particularly concerning, especially given the large number of comparisons in Table 15. Future spectroscopic surveys such as DESI will significantly help the situation—both by improving the statistics and by offering multiple tracers for improved systematics testing.

The unWISE sample exhibits some inhomogeneity, particularly in ecliptic latitude (see Section 7.2), likely due to the variable unWISE coverage depth. This inhomogeneity may also result in spatially varying dN/dz. Given that the dN/dz is based on cross-correlations measured over only a fraction of the unWISE-ACT footprint (see Figure 48), we desire that this area be representative of the full footprint. In Figure 50, we show that the unWISE-ACT and unWISE-BOSS footprints match very well in (absolute value) ecliptic and Galactic latitude. The absolute value is most relevant here because the WISE depth is greatest at the poles and shallowest at the equator; likewise, Galactic contamination is small at both poles. Therefore, the sign of the latitude (hemisphere) matters much less than the distance from the equator. In Table 16, we summarize the mean absolute ecliptic and Galactic latitude of the BOSS and eBOSS surveys. The combined spectroscopic regions are similar in mean absolute ecliptic and Galactic latitude to the unWISE-ACT footprint. Therefore, we expect our cross-correlation estimate of $b(z)dN/dz$ to be representative of the $b(z)dN/dz$ on the unWISE-ACT footprint. Lizancos & White (2023) showed that as long as the redshift distribution assumed in the model matches the mean redshift distribution of the sample used, anisotropies in the dN/dz across the survey footprint do not bias the inferred cosmology.

Table 16
Mean Absolute Value of Ecliptic and Galactic Latitude for Various Footprints

Region	Galactic $\langle\lvert b\rvert\rangle$ (°)	Ecliptic $\langle\lvert\beta\rvert\rangle$ (°)
ACT-unWISE	53.8	25.3
eBOSS N	55.4	39.2
eBOSS S	47.0	15.1
eBOSS N+S	52.1	29.5
BOSS N	55.2	29.5
BOSS S	45.7	14.3
BOSS N+S	52.9	25.8

Note. The combined spectroscopic regions are similar in mean absolute ecliptic and Galactic latitude to the unWISE-ACT footprint.

In Figure 51, we show the variations in dN/dz considered as part of our null tests: restricting to the NGC; restricting to the SGC; and using a larger minimum scale cut in the clustering redshift measurement ($s_{\rm min} = 3.99\ h^{-1}$ Mpc rather than the default $s_{\rm min} = 2.52\ h^{-1}$ Mpc). We show in Figure 21 the impact of these changes on $S_8^\times$; note that the NGC and SGC $S_8^\times$

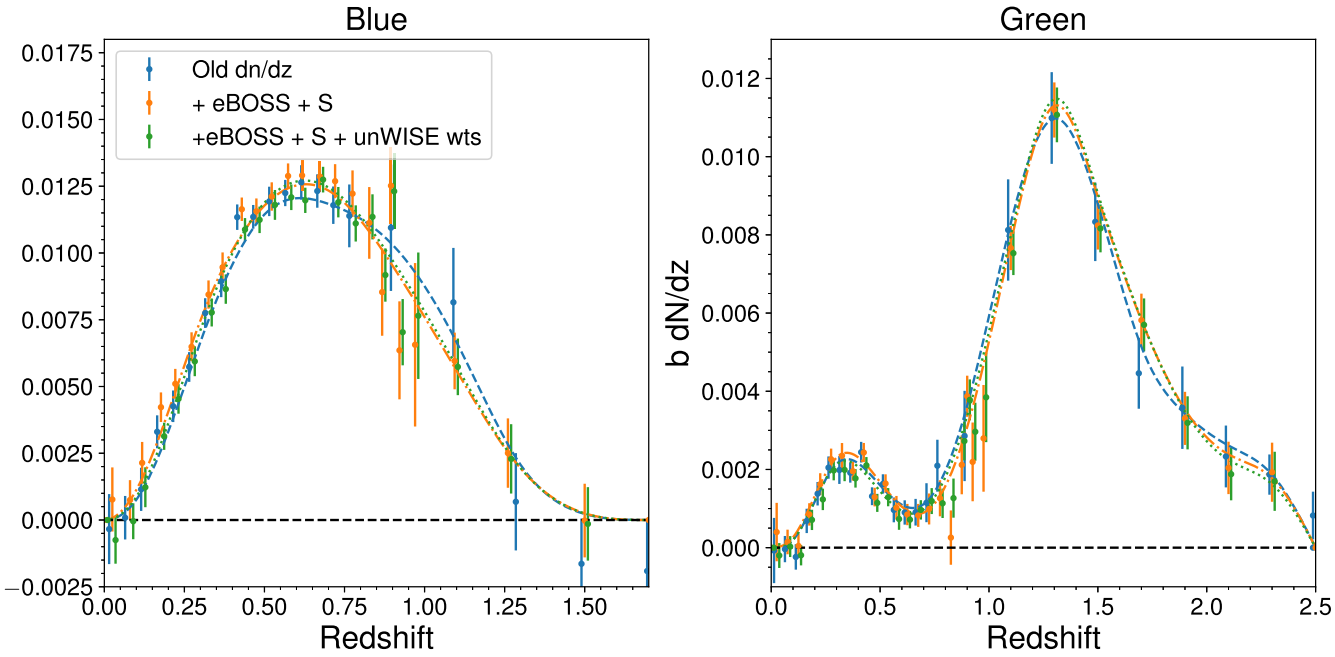

Figure 52. Comparison between the old cross-correlation $b(z)dN/dz$ (from Krolewski et al. 2020, 2021) and the updated $b(z)dN/dz$ used in this work. We show both the data points (i.e., cross-correlation measurement, averaged over scale, divided by spectroscopic sample bias) and the smooth best fits. The $b(z)dN/dz$ used in Krolewski et al. (2021) are shown in blue (with the smoothed best fit shown as a dashed line). The orange data points and dashed line show the estimated bdN/dz after adding the southern spectroscopic samples, the eBOSS LRGs, and replacing the eBOSS DR14 quasars with the DR16 quasars (this also includes the correction to the treatment of the spectroscopic magnification bias). Finally, the green data points and dotted line show estimates that additionally include unWISE weights in the cross-correlation (final version used in this paper). Points are offset in redshift for clarity.

measurements also use the appropriate $C_\ell^{\kappa g}$ and C_ℓ^{gg} measured only on the NGC or SGC, respectively, so the observed $\sim 1\sigma$ shift is expected just due to the different sky areas.

In Figure 52, we compare the new cross-correlation $b(z)dN/dz$ to the old ones, breaking the changes into two parts: the changes or additions to the data set (adding SGC tracers, eBOSS LRGs, and exchanging the eBOSS DR14 quasars for the final eBOSS DR16 quasars), and a change in method (using unWISE weights in the cross-correlation as well as the spectroscopic weights). For Blue, the mean redshift changes from 0.714 to 0.690 when adding more data, and finally to 0.697 when adding the unWISE weights. This is a shift of 0.74σ compared to the standard deviation of 0.023 as measured from 1000 samples of dN/dz, and this large shift is the dominant source for the upward shift in S_8 in the Planck reanalysis. For Green, the mean redshift changes from 1.352 to 1.357 when adding new data, and to 1.355 when adding the unWISE weights (compared to an uncertainty of 0.022: a shift of 0.14σ). The new dN/dz show clearly reduced uncertainty, especially in the eBOSS quasar redshift range of $0.8 < z < 2.0$, where we have used almost four times as much area. Moreover, the new dN/dz have improved redshift resolution at $0.8 < z < 1.0$ from the eBOSS LRG, which reduces the uncertainty on dN/dz in this range, although it is not apparent from the plot. It is also clear that most of the change in dN/dz comes from the addition of the southern footprints of the spectroscopic tracers and the additional eBOSS data; adding unWISE weights makes little difference. Interestingly, the weights seem to make the largest difference at low redshift, where they suppress dN/dz, but make little difference at $z > 0.7$. This suggests that there may have been some small residual systematic power in the cross-correlation redshifts with BOSS CMASS and LOWZ. The changes between the old and new dN/dz are consistent with statistical fluctuations related to adding more data. The changes in dN/dz are largest at $z > 0.8$, where the statistical error is the biggest.

Appendix L
Detailed Discussion of Post-unblinding Changes

As discussed in Section 9.2, we made four minor corrections to the analysis after unblinding. This includes a modification to the treatment of the mask-induced mode coupling of the shot noise, a small correction to the transfer function obtained from simulations, the inclusion of the cross-covariance between the two unWISE samples, and a bug fix affecting the implementation of the higher-order biases. The impact of these corrections partially offsets, and they result in a net shift of -0.1σ in S_8 compared to our initially unblinded results. Here we provide some more detail on these corrections.

In order to compare our theory predictions of C_ℓ^{gg} and $C_\ell^{\kappa g}$ with the observed spectra, we convolve them with a band power window, which captures the effect of the approximate mode decoupling performed on the data. As discussed in Section 4, the expectation value of the observed pseudo-C_ℓ is related to the true underlying C_ℓ through a mode-coupling matrix $M_{\ell\ell'}$,

$$\langle \tilde{C}_\ell \rangle = \sum_{\ell'} C_{\ell'} M_{\ell\ell'}. \tag{L1}$$

For the binned power spectra $\hat{C}_b$, this relation can only approximately be inverted. The decoupled observed power spectrum is then

$$\hat{C}_b^{\text{decoupled}} = \sum_{b'} \widehat{M^{-1}}_{bb'} \hat{C}_{b'} \tag{L2}$$

where $\widehat{M^{-1}}_{bb'}$ is the inverse of the binned mode-coupling matrix obtained under the assumption that the power spectrum is piecewise constant across each bin.[73] The expectation value of the decoupled power spectrum is therefore given in terms of the true underlying C_ℓ by

$$\langle \hat{C}_b^{\rm decoupled} \rangle = \sum_{b'} \widehat{M^{-1}}_{bb'} \sum_{\ell} w_\ell^{b'} \sum_{\ell'} M_{\ell\ell'} C_{\ell'} \tag{L3}$$

where w_ℓ^b are the weights associated with each multipole in bin b. In order to compare a given theory prediction with the observed and decoupled band powers, one thus needs to convolve it with a band power window,

$$F_{b,\ell'} = \sum_{b'} \widehat{M^{-1}}_{bb'} \sum_{\ell} w_\ell^{b'} M_{\ell\ell'}. \tag{L4}$$

For a purely white power spectrum, no mode coupling is induced. This is because, as was pointed out in Hivon et al. (2002), $\sum_{\ell'} M_{\ell\ell'} = w_2$. So no mode decoupling is required on any white noise component of the signal. However, since the mode-coupling matrix is computed in practice only to finite ℓ, the operation of masking the noise and convolving the noise power spectrum with the finite mode-coupling matrix are not equivalent ($\sum_{\ell'=0}^{\ell_{\rm max}} M_{\ell\ell'} \neq w_2$). Consequently, while the white noise present in the map is in fact scaled simply by w_2, the operation applied to the white noise component of the theory spectrum does not reflect this. In principle, the mode-coupling matrix is also inaccurate for the signal component of the spectrum for the same reason; however, because the signal falls off quickly with ℓ, the effect is strongly suppressed. On our simulations we find that power spectrum is most accurately recovered if we instead adopt the following approach:

$$C_b^{\rm th,bpw\ conv.} = \sum_{b'} \widehat{M^{-1}}_{bb'} \sum_{\ell} w_\ell^{b'} \times \left[\sum_{\ell'} (M_{\ell\ell'} (C_{\ell'}^{\rm th} - N_{\rm shot}) + M_{0,\ell'} N_{\rm shot}) \right]. \tag{L5}$$

The inaccuracy in our previous treatment, which did convolve the shot noise with the mode-coupling matrix, due to this effect being very small (<0.1%). In the process of correcting this effect, however, we noticed that because our Gaussian realizations of the lensing field are band limited to $\ell_{\rm max}^{\rm Gaussian\ \kappa} = 5100 < 3{*}{\rm NSIDE}$, our correlated realizations of the galaxy field were not generated with the correct power at $\ell > \ell_{\rm max}^{\rm Gaussian\ \kappa}$. This was originally not taken into account when testing the power spectrum recovery and computing the transfer function (see Section 5). Since the mode-coupling matrix mixes even widely separated scales, the incorrect power at small scales also affects some scales within our analysis range at the ∼0.5% level. Given that the fractional error on C_ℓ^{gg} is of the order of 2%, this explains the $\sim 0.2\sigma$ shift in our results.

Additionally, it was noticed that the cross-covariance between the two redshift samples was erroneously omitted from the analysis. When corrected, this results in the shift of $\sim -0.3\sigma$ in the value inferred for S_8 from the joint analysis of the Blue and Green samples ($\sim -0.17\sigma$ for $S_8^{\times}$) and a slight degradation of constraining power by about 5%.

[73] This is the default approximation implemented in `NaMaster` (Alonso et al. 2019). An alternative approach suggested in Hivon et al. (2002) is to assume the $\ell(\ell+1)C_\ell$ is constant instead.

Finally, we noticed a small bug in the implementation of the bias evolution of the higher-order biases. The fiducial bias evolution for $b_{2,L}$ was erroneously adopted for $b_{s,L}$ as well. Correcting this mistake required newly determining the priors on the higher-order bias offsets from our N-body simulations. The prior mean on the offset for the second-order Lagrangian bias for the Blue sample, $c_{2,L}^{\rm Blue}$, increased from 0.39 to 0.55 (approximately 0.3σ), and since we set the width of the prior to be consistent with $c_{2,L}^{\rm Blue} = 0$, this also required an increase of the width of the prior by ∼30%. The prior mean for the shear bias parameter decreased from $c_{2,s}^{\rm Blue} = 0.30$ to $c_{2,s}^{\rm Blue} = 0.17$, with the width of the prior remaining basically unchanged. For the Green sample, the mean of the prior on $c_{2,L}^{\rm Green}$ also increased by about 30% to 0.42 with the corresponding increase in width. The prior on $c_{2,s}^{\rm Green}$ increased in width by about 15%, while the mean increased by about 30%. We reran the model verification on our N-body sims and recovered the input cosmology well within the requisite 1σ in terms of the covariance appropriate for the simulation volume. This indicates that the error introduced by this bug was at least partially absorbed by our higher-order bias marginalization.

Since the higher-order terms are much more significant for the Blue sample, the impact on the value of S_8 inferred from the Blue sample alone lies at about 0.3σ. On the other hand, our joint inference is unchanged apart from a small, ∼5%, increase in the posterior width. This suggests that in the joint inference, the combined data provide sufficient constraining power to probe the higher-order biases beyond the information given by the prior.

ORCID iDs

Gerrit S. Farren https://orcid.org/0000-0001-5704-1127
Alex Krolewski https://orcid.org/0000-0003-2183-7021
Niall MacCrann https://orcid.org/0000-0002-8998-3909
Simone Ferraro https://orcid.org/0000-0003-4992-7854
Irene Abril-Cabezas https://orcid.org/0000-0003-3230-4589
Zachary Atkins https://orcid.org/0000-0002-2287-1603
Nicholas Battaglia https://orcid.org/0000-0001-5846-0411
J. Richard Bond https://orcid.org/0000-0003-2358-9949
Erminia Calabrese https://orcid.org/0000-0003-0837-0068
Steve K. Choi https://orcid.org/0000-0002-9113-7058
Omar Darwish https://orcid.org/0000-0003-2946-1866
Mark J. Devlin https://orcid.org/0000-0002-3169-9761
Adriaan J. Duivenvoorden https://orcid.org/0000-0003-2856-2382
Jo Dunkley https://orcid.org/0000-0002-7450-2586
J. Colin Hill https://orcid.org/0000-0002-9539-0835
Matt Hilton https://orcid.org/0000-0002-8490-8117
Kevin M. Huffenberger https://orcid.org/0000-0001-7109-0099
Joshua Kim https://orcid.org/0000-0002-0935-3270
Thibaut Louis https://orcid.org/0000-0002-6849-4217
Mathew S. Madhavacheril https://orcid.org/0000-0001-6740-5350
Gabriela A. Marques https://orcid.org/0000-0002-8571-8876
Jeff McMahon https://orcid.org/0000-0002-7245-4541
Kavilan Moodley https://orcid.org/0000-0001-6606-7142
Lyman A. Page https://orcid.org/0000-0002-9828-3525
Bruce Partridge https://orcid.org/0000-0001-6541-9265
Frank J. Qu https://orcid.org/0000-0001-7805-1068

Emmanuel Schaan https://orcid.org/0000-0002-4619-8927
Neelima Sehgal https://orcid.org/0000-0002-9674-4527
Blake D. Sherwin https://orcid.org/0000-0002-4495-1356
Cristóbal Sifón https://orcid.org/0000-0002-8149-1352
Suzanne T. Staggs https://orcid.org/0000-0002-7020-7301
Alexander Van Engelen https://orcid.org/0000-0002-3495-158X
Cristian Vargas https://orcid.org/0000-0001-5327-1400
Lukas Wenzl https://orcid.org/0000-0001-5245-2058
Martin White https://orcid.org/0000-0001-9912-5070
Edward J. Wollack https://orcid.org/0000-0002-7567-4451

References

Abbott, T. M. C., Aguena, M., Alarcon, A., et al. 2022, PhRvD, 105, 023520
Abbott, T. M. C., Aguena, M., Alarcon, A., et al. 2023a, OJAp, 6, 36
Abbott, T. M. C., Aguena, M., Alarcon, A., et al. 2023b, PhRvD, 107, 023531
Abidi, M. M., & Baldauf, T. 2018, JCAP, 2018, 029
Aihara, H., Arimoto, N., Armstrong, R., et al. 2017, PASJ, 70, S4
Aihara, H., Armstrong, R., Bickerton, S., et al. 2018, PASJ, 70, S8
Aiola, S., Calabrese, E., Maurin, L., et al. 2020, JCAP, 2020, 047
Alam, S., Ata, M., Bailey, S., et al. 2017, MNRAS, 470, 2617
Alam, S., Aubert, M., Avila, S., et al. 2021, PhRvD, 103, 083533
Alonso, D., Sanchez, J., & Slosar, A. 2019, MNRAS, 484, 4127
Amon, A., & Efstathiou, G. 2022, MNRAS, 516, 5355
Amon, A., Gruen, D., Troxel, M. A., et al. 2022, PhRvD, 105, 023514
Asgari, M., Lin, C.-A., Joachimi, B., et al. 2021, A&A, 645, A104
Astropy Collaboration, Price-Whelan, A. M., Sipőcz, B. M., et al. 2018, AJ, 156, 123
Astropy Collaboration, Robitaille, T. P., Tollerud, E. J., et al. 2013, A&A, 558, A33
Ata, M., Baumgarten, F., Bautista, J., et al. 2018, MNRAS, 473, 4773
Atkins, Z., Duivenvoorden, A. J., Coulton, W. R., et al. 2023, JCAP, 2023, 073
Bartelmann, M., & Schneider, P. 1999, PhR, 340, 291
Bautista, J. E., Vargas-Magaña, M., Dawson, K. S., et al. 2018, ApJ, 863, 110
Benoit-Levy, A., Dechelette, T., Benabed, K., et al. 2013, A&A, 555, A37
Beutler, F., Blake, C., Colless, M., et al. 2011, MNRAS, 416, 3017
Bianchini, F., Wu, W. L. K., Ade, P. A. R., et al. 2020, ApJ, 888, 119
Brooks, S. P., & Gelman, A. 1998, J. Comput. Graph. Stat., 7, 434
Calabrese, E., Hložek, R. A., Bond, J. R., et al. 2017, PhRvD, 95, 063525
Carron, J. 2023, JCAP, 02, 057
Carron, J., Mirmelstein, M., & Lewis, A. 2022, JCAP, 09, 039
Chang, C., Omori, Y., Baxter, E. J., et al. 2023, PhRvD, 107, 023530
Chen, S.-F., Vlah, Z., Castorina, E., & White, M. 2020a, JCAP, 2021, 100
Chen, S.-F., Vlah, Z., & White, M. 2020b, JCAP, 2020, 062
Chen, S.-F., Vlah, Z., & White, M. 2022a, JCAP, 02, 008
Chen, S.-F., White, M., DeRose, J., & Kokron, N. 2022b, JCAP, 2022, 041
Chiang, Y.-K. 2023, ApJ, 958, 24
Chiang, Y.-K., & Ménard, B. 2019, ApJ, 870, 120
Chisari, N. E., Alonso, D., Krause, E., et al. 2019, ApJS, 242, 2
Comparat, J., Delubac, T., Jouvel, S., et al. 2016, A&A, 592, A121
Dalal, R., Li, X., Nicola, A., et al. 2023, PhRvD, 108, 123519
D'Amico, G., Gleyzes, J., Kokron, N., et al. 2020, JCAP, 05, 005
Darwish, O., Madhavacheril, M. S., Sherwin, B. D., et al. 2021, MNRAS, 500, 2250
Davis, M., & Peebles, P. J. E. 1983, ApJ, 267, 465
du Mas des Bourboux, H., Rich, J., Font-Ribera, A., et al. 2020, ApJ, 901, 153
Eftekharzadeh, S., Myers, A. D., White, M., et al. 2015, MNRAS, 453, 2779
Elvin-Poole, J., Crocce, M., Ross, A. J., et al. 2018, PhRvD, 98, 042006
Elvin-Poole, J., MacCrann, N., Everett, S., et al. 2023, MNRAS, 523, 3649
Feng, Y., Chu, M.-Y., Seljak, U., & McDonald, P. 2016, MNRAS, 463, 2273
Flaugher, B., Diehl, H. T., Honscheid, K., et al. 2015, AJ, 150, 150
Gaia Collaboration, Brown, A. G. A., Vallenari, A., et al. 2018, A&A, 616, A1
García-García, C., Alonso, D., & Bellini, E. 2019, JCAP, 2019, 043
Gelman, A., & Rubin, D. B. 1992, StaSc, 7, 457
Górski, K. M., Hivon, E., Banday, A. J., et al. 2005, ApJ, 622, 759
Gratton, S., & Challinor, A. 2020, MNRAS, 499, 3410
Hang, Q., Alam, S., Peacock, J. A., & Cai, Y.-C. 2021, MNRAS, 501, 1481
Harris, C. R., Millman, K. J., van der Walt, S. J., et al. 2020, Natur, 585, 357
Hartlap, J., Simon, P., & Schneider, P. 2007, A&A, 464, 399
Heymans, C., Tröster, T., Asgari, M., et al. 2021, A&A, 646, A140
HI4PI Collaboration, Ben Bekhti, N., Flöer, L., et al. 2016, A&A, 594, A116
Hivon, E., Gorski, K. M., Netterfield, C. B., et al. 2002, ApJ, 567, 2
Howlett, C., Lewis, A., Hall, A., & Challinor, A. 2012, JCAP, 2012, 027
Hunter, J. D. 2007, CSE, 9, 90
Iršič, V., Di Dio, E., & Viel, M. 2016, JCAP, 2016, 051
Ivanov, M. M., Philcox, O. H. E., Cabass, G., et al. 2023, PhRvD, 107, 083515
Ivanov, M. M., Simonović, M., & Zaldarriaga, M. 2020, JCAP, 05, 042
Kelsall, T., Weiland, J. L., Franz, B. A., et al. 1998, ApJ, 508, 44
Kitanidis, E., & White, M. 2020, MNRAS, 501, 6181
Krolewski, A., & Ferraro, S. 2022, JCAP, 2022, 033
Krolewski, A., Ferraro, S., Schlafly, E. F., & White, M. 2020, JCAP, 2020, 047
Krolewski, A., Ferraro, S., & White, M. 2021, JCAP, 2021, 028
Kuijken, K., Heymans, C., Hildebrandt, H., et al. 2015, MNRAS, 454, 3500
Laigle, C., McCracken, H. J., Ilbert, O., et al. 2016, ApJS, 224, 24
Lang, D. 2014, AJ, 147, 108
Laurent, P., Eftekharzadeh, S., Le Goff, J.-M., et al. 2017, JCAP, 7, 017
Leauthaud, A., Amon, A., Singh, S., et al. 2022, MNRAS, 510, 6150
Lepori, F., Iršič, V., Di Dio, E., & Viel, M. 2020, JCAP, 2020, 006
Lewis, A. 2019, arXiv:1910.13970
Lewis, A., Challinor, A., & Lasenby, A. 1999, ApJ, 538, 473
Li, S.-S., Hoekstra, H., Kuijken, K., et al. 2023, A&A, 679, A133
Li, X., Zhang, T., Sugiyama, S., et al. 2023, PhRvD, 108, 123518
Limber, D. N. 1953, ApJ, 117, 134
Lizancos, A. B., & White, M. 2023, JCAP, 2023, 044
LoVerde, M., & Afshordi, N. 2008, PhRvD, 78, 123506
MacCrann, N., Sherwin, B. D., Qu, F. J., et al. 2023, arXiv:2304.05196
Madhavacheril, M. S., Qu, F. J., Sherwin, B. D., et al. 2024, ApJ, 962, 22
Madhavacheril, M. S., Smith, K. M., Sherwin, B. D., & Naess, S. 2021, JCAP, 2021, 028
Mainzer, A., Bauer, J., Cutri, R. M., et al. 2014, ApJ, 792, 30
Mainzer, A., Bauer, J., Grav, T., et al. 2011, ApJ, 731, 53
Marques, G. A., Madhavacheril, M. S., Darwish, O., et al. 2024, JCAP, 2024, 033
McQuinn, M., & White, M. 2013, MNRAS, 433, 2857
Mead, A. J., Heymans, C., Lombriser, L., et al. 2016, MNRAS, 459, 1468
Meisner, A. M., Lang, D., & Schlegel, D. J. 2017, AJ, 153, 38
Ménard, B., Scranton, R., Schmidt, S., et al. 2013, arXiv:1303.4722
Miyatake, H., Sugiyama, S., Takada, M., et al. 2023, PhRvD, 108, 123517
Modi, C., White, M., & Vlah, Z. 2017, JCAP, 2017, 009
Moessner, R., Jain, B., & Villumsen, J. V. 1997, MNRAS, 294, 291
More, S., Sugiyama, S., Miyatake, H., et al. 2023, PhRvD, 108, 123520
Myers, A. D., Outram, P. J., Shanks, T., et al. 2003, MNRAS, 342, 467
Myers, A. D., Outram, P. J., Shanks, T., et al. 2005, MNRAS, 359, 741
Newman, J. A. 2008, ApJ, 684, 88
Omori, Y., Baxter, E. J., Chang, C., et al. 2023, PhRvD, 107, 023529
Pandey, S., Krause, E., Jain, B., et al. 2020, PhRvD, 102, 28
Percival, W. J., Sutherland, W., Peacock, J. A., et al. 2002, MNRAS, 337, 1068
Planck Collaboration, Aghanim, N., Akrami, Y., et al. 2020a, A&A, 641, A6
Planck Collaboration, Aghanim, N., Akrami, Y., et al. 2020b, A&A, 641, A8
Preston, C., Amon, A., & Efstathiou, G. 2023, MNRAS, 525, 5554
Qu, F. J., Sherwin, B. D., Madhavacheril, M. S., et al. 2024, ApJ, 962, 51
Reid, B., Ho, S., Padmanabhan, N., et al. 2016, MNRAS, 455, 1553
Robertson, N. C., Alonso, D., Harnois-Déraps, J., et al. 2021, A&A, 649, A146
Rodríguez-Monroy, M., Weaverdyck, N., Elvin-Poole, J., et al. 2022, MNRAS, 511, 5665
Ross, A. J., Bautista, J., Tojeiro, R., et al. 2020, MNRAS, 498, 2354
Ross, A. J., Beutler, F., Chuang, C.-H., et al. 2017, MNRAS, 464, 1168
Ross, A. J., Percival, W. J., Sánchez, A. G., et al. 2012, MNRAS, 424, 564
Ross, A. J., Samushia, L., Howlett, C., et al. 2015, MNRAS, 449, 835
Sailer, N., Ferraro, S., & Schaan, E. 2023, PhRvD, 107, 023504
Sailer, N., Schaan, E., & Ferraro, S. 2020, PhRvD, 102, 063517
Samuroff, S., Mandelbaum, R., Blazek, J., et al. 2023, MNRAS, 524, 2195
Schlafly, E. F., Meisner, A. M., & Green, G. M. 2019, ApJS, 240, 30
Schlegel, D. J., Finkbeiner, D. P., & Davis, M. 1998, ApJ, 500, 525
Singh, S., Mandelbaum, R., Seljak, U., Rodríguez-Torres, S., & Slosar, A. 2020, MNRAS, 491, 51
Stein, G., Alvarez, M. A., & Bond, J. R. 2019, MNRAS, 483, 2236
Stein, G., Alvarez, M. A., Bond, J. R., van Engelen, A., & Battaglia, N. 2020, JCAP, 2020, 012
Strauss, M. A., Weinberg, D. H., Lupton, R. H., et al. 2002, AJ, 124, 1810
Sugiyama, S., Miyatake, H., More, S., et al. 2023, PhRvD, 108, 123521
Tanaka, M., Coupon, J., Hsieh, B.-C., et al. 2018, PASJ, 70, S9
Torrado, J., & Lewis, A. 2021, JCAP, 2021, 057
Villumsen, J. V. 1995, arXiv:astro-ph/9512001
Virtanen, P., Gommers, R., Oliphant, T. E., et al. 2020, NatMe, 17, 261

Vlah, Z., Castorina, E., & White, M. 2016, JCAP, 2016, 007
Vlah, Z., White, M., & Aviles, A. 2015, JCAP, 2015, 014
von Wietersheim-Kramsta, M., Joachimi, B., van den Busch, J. L., et al. 2021, MNRAS, 504, 1452
Wang, M. S., Beutler, F., & Bacon, D. 2020, MNRAS, 499, 2598
Weaverdyck, N., & Huterer, D. 2021, MNRAS, 503, 5061
Wenzl, L., Chen, S.-F., & Bean, R. 2024, MNRAS, 527, 1760
White, M., Zhou, R., DeRose, J., et al. 2022, JCAP, 2022, 007
Wright, E. L., Eisenhardt, P. R. M., Mainzer, A. K., et al. 2010, AJ, 140, 1868
Zonca, A., Singer, L., Lenz, D., et al. 2019, JOSS, 4, 1298